

Master of Science Thesis

Efficacy of Linearized Aerodynamic CFD Modeling for Flutter Computation

Niko Tatomir

March 13, 2019

Efficacy of Linearized Aerodynamic CFD Modeling for Flutter Computation

Master of Science Thesis

For obtaining the degree of Master of Science in Aerospace Engineering
at Delft University of Technology

Niko Tatomir

March 13, 2019



Delft University of Technology

Copyright © Aerospace Engineering, Delft University of Technology
All rights reserved.

DELFT UNIVERSITY OF TECHNOLOGY
DEPARTMENT OF AERODYNAMICS

The undersigned hereby certify that they have read and recommend to the Faculty of Aerospace Engineering for acceptance the thesis entitled “**Efficacy of Linearized Aerodynamic CFD Modeling for Flutter Computation**” by **Niko Tatomir** in fulfillment of the requirements for the degree of **Master of Science**.

Dated: March 13, 2019

Supervisors:

Dr.ir. A.H. (Alexander) van Zuijlen

Dr.ir. B.W. (Bas) van Oudheusden

Dr.ir. A.C. (Axelle) Viré

ir. C.F. (Carlos) Baptista

Preface

This Master Thesis project marks the end of my studies at TU Delft. I would like to take the opportunity to thank my supervisor, Dr. ir. Alexander van Zuijlen, for his guidance and particularly for being readily available to discuss my doubts with me. Thank you to my friends for their support and fun times. Finally, I want to thank my family for giving me the opportunity to study abroad and for their encouraging words during the course of my Masters Program.

*Niko Tatomir
Delft, March 2019*

Abstract

Aeroelastic stability must be maintained for the entire flight duration. Of the vast phenomena that fall under the field of aeroelasticity, flutter is the most studied and influential in terms of driving aircraft design. As such, it is the main topic of analysis of this Masters Thesis. For flutter analysis, it is of critical importance to accurately model the system unsteady aerodynamics, particularly for harmonic oscillatory motion. Therefore, the aim of this Master's Thesis is to study the aerodynamic accuracy of a method that uses high fidelity unsteady CFD simulations to build a linearized aerodynamic model, applicable to flows of linear nature. The unsteady aerodynamic loads obtained with the linearized aerodynamic CFD model are validated by comparing them to that of Theodorsen and unsteady OpenFOAM simulations of a harmonically oscillating 2D airfoil.

The results obtained by the linearized aerodynamic CFD model are unable to predict the unsteady air loads for oscillatory harmonic airfoil motion and therefore cannot be used to accurately predict the flutter boundary. The underlying reason for this is the fact that the current formulation of the model does not take into account the wake effects on the unsteady air loads.

Table of Contents

Preface	v
Abstract	vii
List of Figures	xiii
List of Tables	xvii
1 Introduction	1
1.1 Motivation	1
1.2 Literature Review	4
1.3 Research Objective/Question and Plan	6
1.4 Thesis Outline	6
2 Dynamic Aeroelasticity	7
2.1 Introduction	7
2.2 Aeroelastic Systems	7
2.2.1 Structural Dynamics	8
2.2.2 Unsteady Aerodynamics	9
2.3 Flutter Computation Methods: k Method	11
2.4 Modal Analysis	14

2.4.1	Coefficient Extraction Method: Theory	18
2.4.2	Flutter Prediction	19
2.4.3	Gust Response Analysis	21
2.5	Concluding Remarks	22
3	Computational Fluid Dynamics (CFD)	23
3.1	Introduction	23
3.2	Governing Equations	24
3.3	Turbulence Modeling	24
3.3.1	Reynolds Averaged Navier-Stokes (RANS)	25
3.3.2	Turbulence Models: k - ω SST	26
3.4	Mesh Deformation Methods	27
3.4.1	Radial Basis Function (RBF) Interpolation as a Mesh Deformation Method	28
3.5	Concluding Remarks	30
4	Computational Setup	31
4.1	Introduction	31
4.2	NACA 0009 Airfoil	31
4.3	Flow Parameters: The Reynolds Number	32
4.4	Meshing Strategy	34
4.4.1	Mesh Convergence Tests	38
4.5	Boundary Conditions	39
4.5.1	Pressure & Velocity Boundary Conditions	39
4.5.2	Turbulent Boundary Conditions	40
4.6	Finite Volume Schemes & Solution Algorithm	41
4.7	Concluding Remarks	42
5	Validation of OpenFOAM Unsteady Aerodynamic Modeling	43

5.1	Introduction	43
5.2	Comparison of Unsteady Lift for Different Reduced Frequencies with Theodorsen Theory	43
5.2.1	Theodorsen Lift for a Harmonically Pitching Airfoil	44
5.2.2	Convergence Criterion for Unsteady OpenFOAM Simulations	46
5.2.3	Unsteady Lift Results	47
5.3	Comparison of Unsteady Moment for Different Reduced Frequencies with Theodorsen Theory	48
5.3.1	Theodorsen Moment for a Harmonically Pitching Airfoil	48
5.3.2	Unsteady Moment Results	51
5.4	Concluding Remarks	52
6	Validation of Linearized Aerodynamic CFD Modeling	55
6.1	Introduction	55
6.2	The Linearization Technique	55
6.2.1	Coefficient Extraction Method	56
6.3	Results	58
6.3.1	Case 1	61
6.3.2	Case 2	67
6.3.3	Evaluation of the Linearized Aerodynamic CFD Model	71
6.4	Concluding Remarks and Discussion	75
7	Conclusion	79
	Bibliography	81
	A Derivation of Modal Aerodynamic Matrices	87
	B Unsteady Lift for $k = 0.1, 0.3, 0.4$ & 0.8	91
	C Unsteady Moment for $k = 0.1, 0.3, 0.4$ & 0.8	93

D A Comment on the A Matrix	95
E Remaining Results of Case 1 & 2	99

List of Figures

2.1	2DOF Aeroelastic System	8
2.2	Theodorsen Model	9
3.1	Ensemble Averaging of Velocity at a Point in Turbulent Flow	25
4.1	NACA 0009 Airfoil	32
4.2	$\partial c_l / \partial \alpha$ for Different NACA Airfoil Thickness/Type	32
4.3	XFOIL Lift Polars, Natural Transition	33
4.4	XFOIL Lift Polars, Forced Transition	33
4.5	Farfield	35
4.6	Structured C - Grid Around NACA 0009 Airfoil + Unstructured Farfield	36
4.7	Structured O - Grid Around NACA 0009 Airfoil + Structured C - Grid Region	37
4.8	Lift Polars, $Re = 1,000,000$	38
4.9	Drag Polars, $Re = 1,000,000$	38
5.1	c_l vs. <i>time</i> , $k = 0.8$	46
5.2	c_l vs. θ , $k = 0.8$	46
5.3	c_l vs. <i>time</i> , $k = 0.2$	47
5.4	c_l vs. θ , $k = 0.2$	47
5.5	c_l vs. <i>time</i> , $k = 0.6$	47
5.6	c_l vs. θ , $k = 0.6$	47

5.7	c_l vs. <i>time</i> , $k = 1$	47
5.8	c_l vs. θ , $k = 1$	47
5.9	σ_{c_l} vs. k (for unsteady lift)	48
5.10	ϕ_{c_l} vs. k (for unsteady lift)	48
5.11	c_m vs. <i>time</i> , $k = 0.2$	51
5.12	c_m vs. θ , $k = 0.2$	51
5.13	c_m vs. <i>time</i> , $k = 0.6$	51
5.14	c_m vs. θ , $k = 0.6$	51
5.15	c_m vs. <i>time</i> , $k = 1$	51
5.16	c_m vs. θ , $k = 1$	51
5.17	σ_{c_m} vs. k (for unsteady moment)	52
5.18	ϕ_{c_m} vs. k (for unsteady moment)	52
6.1	Case 1.6: c_l vs. <i>time</i>	57
6.2	Case 1.6: c_m vs. <i>time</i>	57
6.3	Case 1: θ' vs. <i>time</i>	62
6.4	Case 1: $\dot{\theta}'$ vs. <i>time</i>	62
6.5	Case 1: Δc_l vs. <i>time</i>	62
6.6	Case 1: Δc_m vs. <i>time</i>	62
6.7	Case 1: σ_{c_l} vs. k (for linearized lift)	64
6.8	Case 1: ϕ_{c_l} vs. k (for linearized lift)	64
6.9	Case 1: σ_{c_m} vs. k (for linearized moment)	65
6.10	Case 1: ϕ_{c_m} vs. k (for linearized moment)	65
6.11	Case 1.7: Δc_l vs. <i>time</i>	65
6.12	Case 1.7: Δc_m vs. <i>time</i>	65
6.13	Case 2: θ' vs. <i>time</i>	67
6.14	Case 2: $\dot{\theta}'$ vs. <i>time</i>	67

6.15	Case 2: Δc_l vs. <i>time</i>	68
6.16	Case 2: Δc_m vs. <i>time</i>	68
6.17	Case 2: σ_{c_l} vs. k (for linearized lift)	69
6.18	Case 2: ϕ_{c_l} vs. k (for linearized lift)	69
6.19	Case 2: σ_{c_m} vs. k (for linearized moment)	70
6.20	Case 2: ϕ_{c_m} vs. k (for linearized moment)	70
6.21	$\partial c_l / \partial \theta$ vs. k	74
6.22	$\partial c_m / \partial \theta$ vs. k	74
6.23	$\partial c_l / \partial \dot{\theta}$ vs. k	74
6.24	$\partial c_m / \partial \dot{\theta}$ vs. k	74
6.25	$\partial c_l / \partial \ddot{\theta}$ vs. k	74
6.26	$\partial c_l / \partial \ddot{\theta}$ vs. k	74
B.1	c_l vs. <i>time</i> , $k = 0.1$	91
B.2	c_l vs. θ , $k = 0.1$	91
B.3	c_l vs. <i>time</i> , $k = 0.3$	91
B.4	c_l vs. θ , $k = 0.3$	91
B.5	c_l vs. <i>time</i> , $k = 0.4$	92
B.6	c_l vs. θ , $k = 0.4$	92
B.7	c_l vs. <i>time</i> , $k = 0.8$	92
B.8	c_l vs. θ , $k = 0.8$	92
C.1	c_m vs. <i>time</i> , $k = 0.1$	93
C.2	c_m vs. θ , $k = 0.1$	93
C.3	c_m vs. <i>time</i> , $k = 0.3$	93
C.4	c_m vs. θ , $k = 0.3$	93
C.5	c_m vs. <i>time</i> , $k = 0.4$	94

C.6	c_m vs. θ , $k = 0.4$	94
C.7	c_m vs. <i>time</i> , $k = 0.8$	94
C.8	c_m vs. θ , $k = 0.8$	94
D.1	$\dot{\theta}'_{ana}/\dot{\theta}'_{num}$ vs. <i>time step</i>	97
D.2	$\ddot{\theta}'_{ana}/\ddot{\theta}'_{num}$ vs. <i>time step</i>	97
E.1	Remaining Results of Case 1: θ' vs. <i>time</i>	99
E.2	Remaining Results of Case 1: $\dot{\theta}'$ vs. <i>time</i>	99
E.3	Remaining Results of Case 1: Δc_l vs. <i>time</i>	99
E.4	Remaining Results of Case 1: Δc_m vs. <i>time</i>	99
E.5	Remaining Results of Case 1: σ_{c_l} vs. k (for linearized lift)	100
E.6	Remaining Results of Case 1: ϕ_{c_l} vs. k (for linearized lift)	100
E.7	Remaining Results of Case 1: σ_{c_m} vs. k (for linearized moment)	100
E.8	Remaining Results of Case 1: ϕ_{c_m} vs. k (for linearized moment)	100
E.9	Remaining Results of Case 2: ϕ_{c_m} vs. k (for linearized moment)	100

List of Tables

4.1	Mesh Topology Parameters	35
4.2	Mesh Topology Parameters for Different Meshes	38
4.3	Finite Volume Schemes for Steady State Cases	41
4.4	Finite Volume Schemes for Unsteady State Cases	42
6.1	Case 1: Linearization Parameters, $\theta'_{final} = 0.005^\circ$	61
6.2	Case 1: Linearized Lift Coefficients, $\theta'_{final} = 0.005^\circ$	63
6.3	Case 1: Linearized Moment Coefficients, $\theta'_{final} = 0.005^\circ$	63
6.4	Case 2: Linearization Parameters, $\theta'_{final} = 0.05^\circ$	67
6.5	Case 2: Linearized Lift Coefficients, $\theta'_{final} = 0.05^\circ$	68
6.6	Case 2: Linearized Moment Coefficients, $\theta'_{final} = 0.05^\circ$	69

Chapter 1

Introduction

1.1 Motivation

It is of critical importance for any aircraft to maintain its stability for the entire flight duration. The class of problems that effectively deal with aircraft stability and flight performance fall under the subject of aeroelasticity. Specifically, aeroelasticity deals with the mutual interaction of aerodynamic loads and elastic structures. The term was first introduced by Alfred Pugsley and Harold Roxbee Cox in the early 1930s (Weisshaar, 2017). The importance of this engineering discipline arose in the early 20th century, when the first airplanes were starting to be developed. Many of the catastrophic events that occurred are a result of various, today known as, aeroelastic phenomena (Garrick and Reed III, 1981). In the most general sense, aeroelasticity can be divided into two parts: *static* aeroelasticity and *dynamic* aeroelasticity. The former deals with aerodynamic and elastic forces while the latter incorporates aerodynamic, inertial and elastic forces. A more detailed breakdown of how various aeroelastic phenomena relate to the aerodynamic, inertial and elastic forces is given by Collar's Triangle (Collar, 1946). The most studied and influential aeroelastic phenomena in terms of driving aircraft design is *flutter* (Garrick and Reed III, 1981; Bisplinghoff et al., 2013; Schuster et al., 2003). As such it is the main focus of this author's Master Thesis. However, gust response analysis is also included in the discussion.

Flutter is a neutrally stable point. At the flutter speed, an aeroelastic system, subject to an initial perturbation, will oscillate harmonically. Hence, energy would neither be added or extracted from the system causing the system to be conservative (Weisshaar, 2017). Above the flutter speed any perturbation of the aeroelastic system will result in increasing oscillations and eventual wing failure. In this case, the system extracts energy from the airflow. Below the flutter point, the wing dissipates energy to the airflow and all oscillations damp out. The classical type of flutter is associated with potential flow where usually, but not necessarily, two or more degrees of freedom are coupled (Bisplinghoff et al., 2013). The non-classical type of flutter is a dynamic instability that could involve separated regions, periodic separation

and reattachment, stalling conditions or moving shock waves. The former can be adequately modeled linearly while the latter requires a nonlinear analysis. In this Master's Thesis, the classical type of flutter problem is considered.

Initially, aeroelastic problems were unanticipated (Weisshaar, 2017). Early flight speeds were low enough such that structural stiffness was not of issue (Bisplinghoff et al., 2013; Weisshaar, 2017). The first powered flight took place on December 17, 1903 by the Wright Brothers. Their biplane made use of a wing warping concept (Garrick and Reed III, 1981), tested by Edson Gallaudet as early as 1898 (Weisshaar, 2017), that uses the wings structural twisting displacement to create aerodynamic rolling moments. This implies the wing must be torsionally flexible. The wing warping concept was also applied successfully to monoplanes; however, as aircraft engines became more powerful and flight speeds increased, the wing torsional stiffness was not sufficient to carry the loads produced, resulting in failure. An example of this is the Bleriot XI monoplane that suffered from wing divergence. Also, the British Bristol Pier aircraft suffered from structural failures in 1912 which resulted in England's ban of all monoplanes (Baker, 1994) and production and development turned to biplanes exclusively, only to have monoplanes resurface towards the end of World War I (WWI). Unfortunately, biplanes were not immune to failure. The twin-engined Handley Page 0/400 bomber suffered from horizontal tail flutter at the beginning of WWI (Bisplinghoff et al., 2013; Weisshaar, 2017). When monoplanes resurfaced and the wing warping concept was abandoned, new aeroelastic instabilities occurred, such as wing aileron flutter. Experimental and theoretical investigations of Von Baumhauer and Koning in 1922 resulted in mass balancing as a solution to the problem and is still used today (Von Baumhauer and Koning, 1923). Wing aileron flutter was also present in biplanes. However, by the 1930s, the use of biplanes was abandoned in favour of monoplanes due to their superior performance. In general, little unsteady aerodynamic theory, mathematical analysis and wind tunnel testing was used when tackling aeroelastic problems in the first two decades of the 20th century. Solutions were mostly found through trial and error and hence there were quite a few fatal accidents. However, due to research conducted by scientists such as Prandtl, Birnbaum, Küssner, Wagner and Perring, to name a few, fundamentals of flutter were understood by the end of the 1920s (Frazer, 1929).

During and after World War II (WWII), USA's efforts shifted to studying transonic and supersonic flight. With the invention of the jet engine, aircrafts approached transonic speeds, introducing new and challenging aeroelastic problems. To this day, transonic flutter is difficult to analyse due to it being characterized by strong nonlinearities (Schuster et al., 2003). In 1944, the P-80 airplane suffered from "aileron buzz", a single degree of freedom flutter caused by the coupling of the aileron rotation and the movement of shock waves along the wing in the chordwise direction (Garrick and Reed III, 1981). This type of flutter involved nonlinearities such as periodical separation and reattachment of the flow behind the moving shock waves (Garrick and Reed III, 1981). The first supersonic flight happened in 1947, when Charles Yeager broke the sound barrier by flying the rocket powered X-1 research airplane. Supersonic flight suffered from a new type of flutter called panel flutter (Weisshaar, 2017). More than 70 failures of Wernher von Braun's V-2 rocket occurred during WWII, many of which were due to panel flutter near the nose of the rocket (Garrick and Reed III, 1981). Panel flutter was also a problem for the Saturn V Apollo launch vehicle rocket in the 1960s.

From historical examples it is clear that the importance of adequately analyzing aeroelastic phenomena increased, primarily due to inadequate structural stiffness that became critical as aircraft speed increased. If airplane structures were perfectly rigid, aeroelasticity as a discipline would not exist (Bisplinghoff et al., 2013). Aeroelastic design remains an integral part of aircraft design not only due to the fact that these vehicles operate at subsonic, transonic, supersonic and even hypersonic conditions but also because there is a need to manufacture lighter aircraft in order to decrease fuel consumption, which leads to a more flexible structure (Prananta, 1999). Even though the field of aeroelasticity was driven by human flight, it is relevant in other fields as well such as turbomachinery and wind turbines. In the ever growing need for renewable energy sources, wind energy plays a major role. In order to increase efficiency and energy extraction the overall size and rotor diameter are continuously growing resulting in an increasing amount of research in the field of extreme scale wind turbines (Stuurman, 2016). These wind turbines are more likely to be stability driven than loads-driven, as is currently the case (Bir and Jonkman, 2007), and their main aeroelastic issues are edgewise blade vibrations and classical blade flutter (Hansen et al., 2006).

To accurately analyze any aeroelastic phenomena, it is of major importance to adequately model the systems inertial, structural and aerodynamic features. However, none is more important than the theoretical aerodynamics model (Weisshaar, 2017). Much of today's research is aimed at modeling transonic flows due to the nonlinearities of the system while subsonic/supersonic aeroelastic analysis is considered a mature science due to its linear nature (Schuster et al., 2003). This should, by no means, serve as discouragement when attempting to develop higher fidelity aerodynamic models that could describe linear aeroelastic phenomena with an increased accuracy while not significantly increasing the computational cost. Stuurman (2016) built a linearized aerodynamic CFD model that was used to analyze classical flutter of a wind turbine blade in incompressible flow via a modal analysis. The linearized model has potential to be used in preliminary design phases of aircraft due to it being computationally inexpensive. This author's Master Thesis serves as a continuation of Mark Stuurman's Master Thesis. As such, the main objective is as follows

Validate the efficacy of a linearized aerodynamic CFD model in accurately predicting incompressible unsteady aerodynamic loads and hence aeroelastic instabilities such as classical flutter.

1.2 Literature Review

The character of aerodynamic flows treated in this Master's Thesis is subsonic and incompressible. Hence, this brief literature review is restricted to state of the art methods used for modeling these types of flows. The problem formulation that forms the basis for aeroelastic analysis is given in the form of generalized aeroelastic equation of motion (EOM) (Schuster et al., 2003) as follows

$$[M_s]\{\ddot{q}(t)\} + [D_s]\{\dot{q}(t)\} + [K_s]\{q(t)\} = \{F(t)\}, \quad (1.1)$$

$$\{w(x, y, z, t)\} = \sum_{i=1}^{N_{modes}} q_i(t)\{\phi_i(x, y, z)\}, \quad (1.2)$$

where $\{w(x, y, z, t)\}$ is the structural displacement at any position and time on the flight vehicle. The vector $\{q_i(t)\}$ is the amplitude function, describing the time history of all the modes of vibration. They are also called the generalized coordinates. The vector ϕ_i represents the normal modes of the structure. The generalized structural mass, damping and stiffness matrices are $[M_s]$, $[D_s]$ and $[K_s]$, respectively. These matrices result from the properties of the structure, contain the system structural dynamics and are typically obtained by using Finite Element (FEM) techniques. Generally, when dealing with the aeroelasticity of aircraft, it is assumed that the structural dynamics are of linear nature (Prananta, 1999). On the other hand, this does not hold for the aerodynamics where the forces and moments that compose the generalized forcing term $\{F(t)\}$ of the aeroelastic EOM are modeled linearly or nonlinearly, depending on the flow regime and the type of aeroelastic phenomena that is to be predicted. For example, limit cycle oscillations cannot be predicted with a fully linear model. The generalized forcing term $\{F(t)\}$ couples the unsteady aerodynamics and inertial loads with the structural dynamics.

Classical aerodynamic models for aeroelastic analysis of a 2D airfoil in incompressible flow (Bisplinghoff et al., 2013) include the Wagner function that describes the response for a unit step change in angle of attack (Wagner, 1925), Küssner's function which gives the response to a sharp edged gust (Küssner, 1935), Theodorsen's function that gives a frequency response to sinusoidal oscillations (Theodorsen, 1935) and the Sear's function which gives the frequency response to a sinusoidal gust (Giesing et al., 1970). Theodorsen's expression for unsteady lift and moment responses due to a sinusoidally oscillating airfoil were a breakthrough in terms of allowing a full understanding of the mechanisms of flutter. Experimental validation was carried out and confirmed that these expressions accurately predicted the lift and moment response over a wide range of frequencies (Halfman, 1952) but are also limited to small oscillatory amplitudes (Cordes et al., 2017) due to the assumptions made prior to deriving Theodorsen's expressions (Dimitradis, 2018). Theodorsen's expressions are still used for conceptual and preliminary design purposes in the industry today (Murua et al., 2012). However,

these analytical response expressions are impractical for more complex configurations such as wings or full scale aircraft (Lucia et al., 2004; Silva and Bartels, 2004). Due to this and the rise of computing power, numerical analysis of linear unsteady aerodynamic responses became the method of choice (Giesing and Kalman, 1971). Specifically, the Doublet Lattice Method (Albano and Rodden, 1969) became the industry standard in the preliminary design phase (Murua et al., 2012; Yurkovich et al., 2001; Burt, 1993; Försching, 1995) and is used for accurate aeroelastic analysis in the subsonic regime (Prananta, 1999; Yurkovich et al., 2001). On the other hand, Stuurman (2016) used a linearized aerodynamic CFD model for modeling the unsteady aerodynamic air loads. Gust response analysis is carried out by adding an additional forcing term to the generalized force term of Equation 1.1. For a gust response analysis, multiple unsteady aerodynamic models can be utilized. Kier (2005) carried out a comparison of different aerodynamic models for a gust response analysis. The models that he compared are the quasi-steady vortex lattice method (VLM), Roger's method for rational function approximation of the doublet lattice method, and strip theory where unsteady effects are modeled with indicial functions such as the Wagner or Küssner Function.

Assuming linear modeling of the structural dynamics, the aerodynamics can be modeled linearly or nonlinearly and depending upon the choice, the solution to the problem is found either using the frequency domain approach or time domain methods, respectively (Bergami, 2008; Prananta, 1999). Since the frequency domain approach assumes a set of linearized EOM, the formulation becomes an eigenvalue problem that can be solved by finding the eigenvalues of system where each eigenvalue is associated with a specific frequency and damping of a particular eigenmode and hence allows for the flutter speed to be determined (Dimitradis, 2018). This is done for a large number of flight speeds and altitudes. Classical methods for solving the eigenvalue problem are the V-g (i.e. k) method (Smilg and Wasserman, 1942) and the p-k method (Hassig, 1971). If the linear aerodynamic model is frequency dependent (e.g. Theodorsen), it can still be solved in the time domain with numerical integration, as long as the frequency dependent terms are transferred into the time domain using rational function approximation such as Roger's approximation (Roger, 1977). Stuurman (2016)'s linearized aerodynamic CFD model produces a linear EOM system that is already only time dependent and can hence be solved either numerically or as an eigenvalue problem. For nonlinear aerodynamic models this cannot be done and they can only be integrated numerically in time.

The coupling of FEM techniques to model the structural dynamics and linearized potential flow equations for modeling aerodynamic terms is the standard industrial approach. However, as high fidelity CFD techniques emerged, it became possible to use nonlinear aerodynamic analysis and transiently simulate aeroelastic phenomena. This allows for the most accurate analysis of the aerodynamics of an aeroelastic system up to date and is particularly useful where nonlinearities dominate or in subsonic/supersonic regime with large angles of attack, where linearized potential flow methods cannot sufficiently describe the aerodynamic response. While computational requirements limit the use of such a method and prevent it from being applied in preliminary design phases (Lucia et al., 2004; Silva and Bartels, 2004), computations have been done on simpler geometries such as 3D wings subjected to a transonic flow regime (Schuster et al., 2003). In the past two decades there have been advances in utilizing reduced-order modeling (ROM) for aeroelastic applications (Schuster et al., 2003). These methods use high fidelity simulations for building ROM models that can then analyze aeroelastic phenomena at a reduced computational cost (Lucia et al., 2004; Silva and Bartels, 2004).

1.3 Research Objective/Question and Plan

Stuurman (2016) used a linearized aerodynamic CFD model to model the aerodynamic forces of a wind turbine blade. These forces will compose the RHS of the EOM given by Equation 1.1. The system stability is then analyzed in order to compute for flutter. The underlying assumption is that this model is valid for any type of airfoil motion, as long as the perturbations are small, such that flow linearity is preserved. The main research objective of this author's Master Thesis is to investigate the *efficacy of this linearized aerodynamic CFD model* for computing aeroelastic instabilities such as flutter. The complete analysis is carried out on a 2D airfoil subject to the incompressible flow regime. The main research question is

Can linearized aerodynamic CFD models, used to model the aerodynamics of an aeroelastic system, be utilized to accurately predict flutter?

Flutter is a neutrally stable point. At the flutter boundary, the airfoil oscillates harmonically. Therefore, in order to be able to accurately compute the flutter boundary, the unsteady aerodynamic model must be capable of accurately computing the unsteady air loads of a harmonically oscillating airfoil. As such, the unsteady lift and moment loads obtained by the linearized aerodynamic CFD model are compared with that of Theodorsen Theory and unsteady OpenFOAM simulations of a harmonically oscillating 2D airfoil. In order to analyze a gust response, a gust forcing term must be added to the RHS of the EOM. Furthermore, the linearized aerodynamic CFD model must be able to predict arbitrary airfoil motion, since an airfoil subject to a specific gust will have an arbitrary-like response. This is not the main focus of this author's Master Thesis and as such is not thoroughly investigated. Nevertheless, some preliminary conclusions are made from the analyses that were carried out when validating the linearized model for harmonic oscillatory motion.

1.4 Thesis Outline

In this section, the structure of the Master Thesis is explained. Chapter 2 deals with dynamic aeroelasticity. The aeroelastic system of a 2D airfoil is introduced. The Theodorsen Aerodynamics are discussed and as well as the flutter computation method (i.e. k method). The linearized aerodynamic CFD model (Stuurman, 2016) is introduced. Finally, flutter prediction and gust response in terms of modal coordinates with the use of the linearized model are explained. Chapter 3 gives an overview of the fundamental concepts of Computational Fluid Dynamics. Chapter 4 explains the reasoning behind the type of 2D airfoil and the magnitude of the Reynolds Number that is chosen for further analysis. In addition, the meshing strategy is explained, boundary conditions and the numerical setup of the unsteady simulations are given, as well as the results of the mesh convergence tests. Chapter 5 compares the unsteady lift and moment coefficients obtained via Theodorsen Aerodynamics and unsteady CFD simulations for various reduced frequencies. Chapter 6 compares the results of the linearized aerodynamic CFD model with the results obtained in Chapter 5. Finally, Chapter 7 gives a thorough conclusion of the linearized model, identifying its advantages and drawbacks.

Chapter 2

Dynamic Aeroelasticity

2.1 Introduction

In this chapter, a thorough description of a dynamic aeroelastic analysis for a 2DOF (Degree of Freedom) airfoil in rigid body motion is given. The airfoil is allowed to only pitch and plunge. The complete aeroelastic system is introduced, composed of the structural dynamics and unsteady aerodynamics (i.e. Theodorsen Theory). Such a system can be then used for flutter analysis, as is shown in Section 2.3. While Theodorsen aerodynamics was considered a breakthrough and allowed for an accurate mathematical analysis of flutter, it is impractical for use in more complex configurations such as wings or full scale aircraft (Lucia et al., 2004; Silva and Bartels, 2004). Therefore, different methods that could deal with such configurations became the industry standard, such as the doublet lattice method. In this Master Thesis, the proposed linearized aerodynamic model obtained from unsteady CFD simulations is analyzed. Its derivation and potential use for computing flutter and gust response is thoroughly explained in Section 2.4.

2.2 Aeroelastic Systems

In this section, the structural dynamics and unsteady aerodynamics that compose the aeroelastic system are explained. This aeroelastic system describes the sinusoidal oscillatory motion of a 2DOF airfoil shown in Figure 2.1. This airfoil is allowed to pitch and plunge and is subject to a constant inflow velocity U . The spring stiffness that opposes the pitching motion is K_α , while the spring stiffness that opposes the plunging motion is K_h . These springs are modeling the actual wing stiffness. The lift and moment act about the elastic axis positioned ba from the airfoil midchord and bx_α from the airfoils center of gravity. The variable a is the dimensionless distance, nondimensionalized by the midchord length b . A positive value indicates the elastic axis is aft of the airfoil midchord and a negative value means its located

prior to the airfoil midchord. The variable x_α is the dimensionless distance, also nondimensionalized by the midchord length b . A positive value of x_α indicates that the airfoils center of gravity is aft of the elastic axis, while a negative value indicates its prior to the elastic axis.

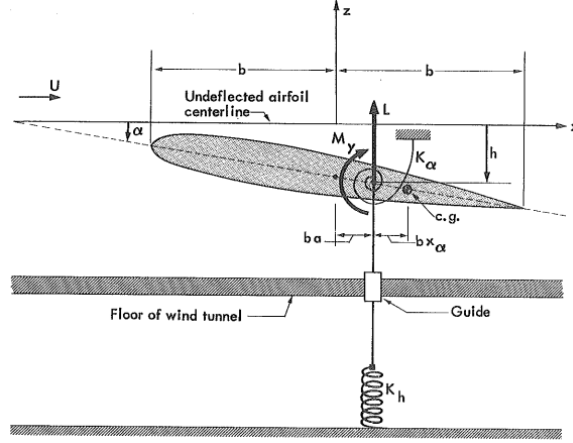


Figure 2.1: 2DOF Aeroelastic System (Bisplinghoff et al., 2013)

2.2.1 Structural Dynamics

The structural dynamics simply define the equations of motion for the 2DOF airfoil. The equations of motion are composed of two equations: the plunge equation and the pitch equation. These two equations can be put in matrix form and are given by Equation 2.1 below. Note that the positive direction of airfoil plunging is downward, while the pitch is positive in the clockwise direction. Furthermore, the lift is defined as positive in the upwards direction while the moment is positive when it acts clockwise about the elastic axis. Note that the motion in pitch is described by the variable θ instead of α , since α will be used to denote the steady state angle of attack when necessary.

$$\begin{bmatrix} m & S_\theta \\ S_\theta & I_\theta \end{bmatrix} \begin{Bmatrix} \ddot{h} \\ \ddot{\theta} \end{Bmatrix} + \begin{bmatrix} K_h & 0 \\ 0 & K_T \end{bmatrix} \begin{Bmatrix} h \\ \theta \end{Bmatrix} = \begin{Bmatrix} -L \\ M_{EA} \end{Bmatrix}, \quad (2.1)$$

where m is the mass of the airfoil section, $S_\theta = mbx_\theta$ is the static unbalance about the elastic axis and $I_\theta = mb^2r_\theta^2$ is the moment of inertia about the elastic axis. Note that r_θ is the dimensionless radius of gyration (dimensionalized by the midchord length b). Equation 2.1 can be derived using Lagrange's equations or Newton's Second Law (Inman and Singh, 1994). The LHS represents the structural dynamics that are linearly modeled and hence are valid only for small perturbations in pitch and plunge from the airfoils equilibrium position. Linearity implies that the two structural matrices are not a function of the airfoil displacement in pitch and plunge. The RHS symbolically represents the lift and moment that contribute to the plunge and pitch, respectively. A more detailed analysis of these terms and their restrictions

are given in the next section. This system is dynamically coupled due to the non-diagonal term S_θ and is usually written in the following form

$$[M_s]\{\ddot{\mathbf{x}}\} + [K_s]\{\mathbf{x}\} = \{\mathbf{F}_{aero}\}, \quad (2.2)$$

where $[M_s]$ is the structural mass matrix and $[K_s]$ is the structural stiffness matrix. $\{\mathbf{x}\} = [h, \theta]^T$ is a vector that contains the degrees of freedom of the system. Finally, $\{\mathbf{F}_{aero}\}$ is a vector of forces, in this case aerodynamic forces, that act on each of the degrees of freedom. Such a system of equations, as is shown by Equation 2.2, could represent a 3D wing where the mass and stiffness matrices would be derived using the Finite-Element Method.

2.2.2 Unsteady Aerodynamics

In this section, an accurate model of unsteady aerodynamics (i.e. Theodorsen Theory) is presented and explained. Theodorsen used a linearized potential flow model to obtain a solution for the unsteady lift and moment on a 2D harmonically oscillating thin airfoil in inviscid, incompressible flow (Theodorsen, 1935). The mathematical representation of the model is given in Figure 2.2 below. The airfoil and wake are represented by a vortex sheet γ_b and γ_w , respectively. The shed circulation is equal and opposite in sign to the change in the total circulation of the airfoil, hence satisfying Kelvin's Theorem (De Breuker, 2018). The wake is considered planar, which is a valid assumption for small perturbation angles and across it the net pressure jump must be zero (Leishman, 2006). The flow is assumed to be attached, which is ensured by enforcing the Kutta condition to be satisfied at the trailing edge of the airfoil (Leishman, 2006; Dimitradis, 2018).

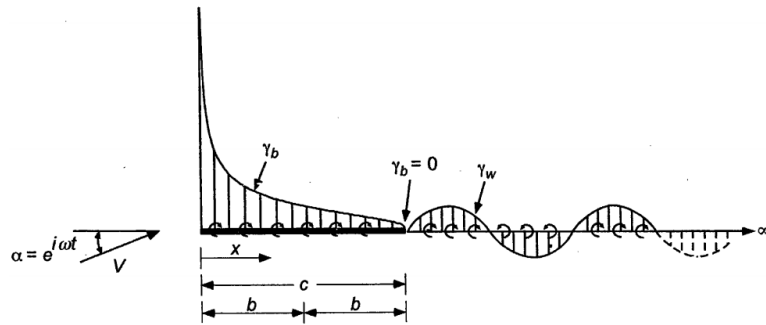


Figure 2.2: Theodorsen Model (Leishman, 2006)

Theodorsen Theory gives the unsteady lift and moment for a harmonically oscillating airfoil (pitch + plunge) in the following form

$$c_l = \frac{\pi b}{U^2} \left[\ddot{h} + U\dot{\theta} - ba\ddot{\theta} \right] + \frac{c_{l,\alpha} C(k)}{U} \left[\dot{h} + U\theta + b \left(\frac{1}{2} - a \right) \dot{\theta} \right], \quad (2.3)$$

$$\begin{aligned}
c_m = & \frac{\pi}{2U^2} \left[ba\ddot{h} - Ub\left(\frac{1}{2} - a\right)\dot{\theta} - b^2\left(\frac{1}{8} + a^2\right)\ddot{\theta} \right] + \\
& + \frac{c_{l,\alpha}C(k)}{2U} \left(a + \frac{1}{2} \right) \left[\dot{h} + U\theta + b\left(\frac{1}{2} - a\right)\dot{\theta} \right],
\end{aligned} \tag{2.4}$$

where $c_{l,\alpha}$ is the steady state lift curve slope. Note that a is the previously introduced dimensionless distance of the elastic axis from the midchord, nondimensionalized by the midchord length b . Furthermore, U is the constant inflow velocity, the pitch θ is defined positive in the clockwise direction while the plunge h is defined positive in the downwards direction. Finally, $C(k)$ is Theodorsen's function. The unsteady lift and moment expressions are composed of the non-circulatory and circulatory terms. The first term in both expressions represents the non-circulatory term that take into account the force and moment required to accelerate the flow in the vicinity of the airfoil (Wright and Cooper, 2008). The second term in both equations is the circulatory term. The circulatory term contains the complex Theodorsen's function $C(k)$ that accounts for the effects of the shed wake on the unsteady circulatory lift and moment (Leishman, 2006). The shed wake creates pressure disturbances that propagate upstream and affect the flowfield around the airfoil and hence the circulation, therefore causing a delay in the buildup of the aerodynamic forces and moments (De Breuker, 2018). Note that the terms in the brackets of the second term in the unsteady lift and moment equations is the apparent angle of attack, comprised of the downwash due to plunging, the actual angle of attack and the downwash due to pitching (Leishman, 2006; De Breuker, 2018). Theodorsen's function, as well as the unsteady lift and moment are only a function of the reduced frequency k

$$k = \omega_{rad}b/U, \tag{2.5}$$

where ω_{rad} is the oscillation frequency in radians. The reduced frequency defines the unsteadiness of the problem, i.e. the importance of vorticity dynamics. As $k \rightarrow 0$, $C(k) \rightarrow 1$ and the unsteady lift and moment equations reduce to the result of the quasi-steady aerodynamic model. Here the effects of the shed wake are not considered. If the non-circulatory aerodynamic terms are not included, since at such low reduced frequencies they are practically negligible, the standard quasi-steady thin-airfoil results is obtained. This model is valid for reduced frequencies of $k \leq 0.05$ (Leishman, 2006).

2.3 Flutter Computation Methods: k Method

Flutter is a neutrally stable point. At the flutter speed, an aeroelastic system, subject to an initial perturbation, will oscillate harmonically. Hence energy would neither be added or extracted from the system causing the system to be conservative (Weisshaar, 2017). Above the flutter speed any perturbation of the aeroelastic system will result in increasing oscillations and eventual wing failure. In this case, the system extracts energy from the airflow. Below the flutter point, the wing dissipates energy to the airflow and all oscillations damp out.

There are multiple flutter computation methods: Theodorsen's method (Fung, 2008), k method (i.e. V-g method) (Smilg and Wasserman, 1942), p method and the $p - k$ method (Hassig, 1971). Theodorsen's method, the k method and the $p - k$ method all compute the flutter speed exactly (Weisshaar, 2017; De Breuker, 2018). However, only the $p - k$ method gives a true value of modal damping (given that the damping is relatively small), for velocities below and above the flutter boundary (Weisshaar, 2017; De Breuker, 2018). The p method gives correct damping values but is only able to approximate the flutter speed (De Breuker, 2018). The k method is the simplest and least computationally expensive method that can exactly compute the flutter speed and is explained in this section. The aeroelastic EOM of the system given by Figure 2.1 is of the following form

$$[M_s] \begin{Bmatrix} \ddot{h} \\ \ddot{\theta} \end{Bmatrix} + [K_s] \begin{Bmatrix} h \\ \theta \end{Bmatrix} = q_\infty [Q_a(k)] \begin{Bmatrix} h \\ \theta \end{Bmatrix}, \quad (2.6)$$

where q_∞ is the freestream dynamic pressure. The matrix $[Q_a(k)]$, given by Equation 2.7 below, is a matrix containing the aerodynamic forces and moments due to harmonically pitching and plunging motions. It is only a function of the reduced frequency k .

$$[Q(k)] = c_{l,\alpha} k^2 \begin{bmatrix} L_h & b[L_\theta - L_h(\frac{1}{2} + a)] \\ b[M_h - L_h(\frac{1}{2} + a)] & b^2[M_\theta - (L_\theta + \frac{1}{2})(\frac{1}{2} + a) + L_h(\frac{1}{2} + a)^2] \end{bmatrix}. \quad (2.7)$$

Note that $c_{l,\alpha}$ is the steady state lift curve slope, b is the midchord length and L_h , L_θ , M_h , M_θ are dimensionless functions of the reduced frequency k (Bisplinghoff et al., 2013). Weisshaar, 2017 provides the expressions for these functions as is shown by the relations below

$$L_h = 1 - i \frac{2C(k)}{k}; \quad L_\theta = \frac{1}{2} - i \frac{[1 + 2C(k)]}{k} - \frac{2C(k)}{k^2}; \quad (2.8)$$

$$M_h = \frac{1}{2}; \quad M_\theta = \frac{3}{8} - i \frac{1}{k}.$$

Note that $M_h = 1/2$ is only true for the incompressible case. The k method assumes that the response of the aeroelastic system given by Equation 2.6 is purely harmonic (i.e. the eigenvalues are purely imaginary). Therefore, the assumed solution is of the following form

$$\begin{Bmatrix} \bar{h} \\ \bar{\theta} \end{Bmatrix} = \begin{Bmatrix} \bar{h} \\ \bar{\theta} \end{Bmatrix} e^{i\omega t}, \quad (2.9)$$

and when substituted into Equation 2.6, the following system is obtained

$$\left[-\omega^2[M_s] + [K_s] \right] \begin{Bmatrix} \bar{h} \\ \bar{\theta} \end{Bmatrix} = q_\infty[Q_a(k)] \begin{Bmatrix} \bar{h} \\ \bar{\theta} \end{Bmatrix}. \quad (2.10)$$

At the flutter speed (i.e. flutter boundary), the aeroelastic system will harmonically oscillate. At other airspeeds, due to aerodynamic damping contained in the aerodynamic matrix $[Q_a(k)]$, the response of the system will not be harmonic; however, the aerodynamics are only valid for a harmonically oscillating airfoil. Therefore, to ensure that the response of the system will always be harmonic, artificial structural damping is added to the system that cancels the aerodynamic damping that is present. The airspeed at which the artificial damping is zero is the flutter speed (De Breuker, 2018). The artificial damping is added to the pitching and plunging components of the stiffness matrix in the following way

$$\left[-\omega^2[M_s] + (1 + ig)[K_s] - q_\infty[Q_a(k)] \right] \begin{Bmatrix} \bar{h} \\ \bar{\theta} \end{Bmatrix} = \{\mathbf{0}\}. \quad (2.11)$$

Note that a negative value of artificial damping g means that the aeroelastic system is damped out in time. It indicates the amount of artificial damping that must be extracted from the system for it to oscillate harmonically. A positive value of artificial damping g means that the aeroelastic systems vibrations are amplified in time. It indicates the amount of artificial damping that must be added to the system for it to oscillate harmonically. The concept of artificial damping is a mathematical tool introduced to ensure that the response of the aeroelastic EOM is always purely harmonic since the equations are only valid for a harmonically oscillating system. The artificial damping values should not be interpreted as the actual damping values of the aeroelastic system (Weisshaar, 2017; De Breuker, 2018). Therefore, the k method only provides physical results at the flutter boundary, where the artificial damping is zero and the response is actually purely harmonic. Finally, Equation 2.11 is rearranged and the eigenvalue analysis is done on the following system of equations

$$[K_s]^{-1} \left[[M_s] + \frac{1}{2}\rho \left(\frac{b}{k} \right)^2 [Q_a(k)] \right] \begin{Bmatrix} \bar{h} \\ \bar{\theta} \end{Bmatrix} = \frac{1 + ig}{\omega^2} \begin{Bmatrix} \bar{h} \\ \bar{\theta} \end{Bmatrix}, \quad (2.12)$$

where for a fixed air density ρ , the LHS of Equation 2.12 and its eigenvalues λ are a function of the reduced frequency k . The eigenvalues will be of the form

$$\lambda_{Re} + i\lambda_{Im} = \frac{1}{\omega^2} + i\frac{g}{\omega^2}. \quad (2.13)$$

The eigenvalue analysis is carried for various values of the reduced frequency k until the damping term (i.e. λ_{Im}) becomes zero. At this point the velocity is backcalculated from the corresponding reduced frequency k (see step 5 of the procedure shown below). The procedure for carrying out the k method is given below

1. Choose a value of the air density ρ . This will model the altitude.
2. Choose a value of the reduced frequency k .
3. Compute the eigenvalues of the LHS of Equation 2.12 for the corresponding value of k .
4. Compute the frequency of each mode with the following formula

$$\omega = \sqrt{\frac{1}{\lambda_{Re}}}. \quad (2.14)$$

5. Compute the velocity and artificial damping from the following formulas, respectively

$$U = \frac{\omega b}{k}, \quad (2.15)$$

$$g = \omega^2 \lambda_{Im}. \quad (2.16)$$

6. Repeat steps 2-5 for various values of k until the damping term g is zero. Backcalculate the speed for the corresponding k and this will be the flutter speed.

2.4 Modal Analysis

In this section, the modal analysis method is explained, where the forces are obtained using a linearized CFD model. Consider the following system of equations of motion

$$[M_s]\{\ddot{\mathbf{x}}\} + [C_s]\{\dot{\mathbf{x}}\} + [K_s]\{\mathbf{x}\} = \{\mathbf{F}(\mathbf{x}, \dot{\mathbf{x}}, \ddot{\mathbf{x}})\}, \quad (2.17)$$

where the number of equations in the system above is equal to the number of degrees of freedom n of the model. The system of equations formulation given by Equation 2.17 can serve as a starting point for an analysis of any type of vibration system, such as a building subject to an earthquake or strong winds. For easier conceptualization, the application of the EOM will be limited to a 3D airplane wing further on. As such, the degrees of freedom can symbolize rigid body motion and/or structural deformation. $[M_s]$ is the structural mass matrix, $[C_s]$ is the structural damping matrix and $[K_s]$ is the structural stiffness matrix. The structural mass, damping and stiffness matrices are all $n \times n$ matrices. If structural linearity is assumed, these matrices will be constant and are not a function of the structural displacement. For complex structures such as 3D airplane wings or even full aircraft configurations, the finite element method is used to discretize the equation describing the structural dynamics in order to obtain the mass, damping and stiffness matrices characterizing the system at the static steady state. The static steady state is defined as the final deformed position of the wing due to steady state aerodynamic loads. The equation describing the structural dynamics could be the linearized beam model, for example. The forcing vector on the RHS of Equation 2.17 is an aerodynamic forcing vector that is dependent on the structural deformation

$$\{\mathbf{F}(\mathbf{x}, \dot{\mathbf{x}}, \ddot{\mathbf{x}})\} = \{F_1(\mathbf{x}, \dot{\mathbf{x}}, \ddot{\mathbf{x}}), F_2(\mathbf{x}, \dot{\mathbf{x}}, \ddot{\mathbf{x}}), F_3(\mathbf{x}, \dot{\mathbf{x}}, \ddot{\mathbf{x}}), \dots, F_n(\mathbf{x}, \dot{\mathbf{x}}, \ddot{\mathbf{x}})\}^T. \quad (2.18)$$

The aerodynamic forcing vector is composed of n forcing terms, each acting on a specific degree of freedom. While the structural dynamics are of linear nature, the aerodynamic forcing can be nonlinear or linear. Modeling the aerodynamic forcing as nonlinear would require a fully transient FSI simulation where the structure is deformed each time step adequately with regards to the present aerodynamic forces. Perhaps even sub-iterations would be required for each time step. Such a methodology is too computationally expensive. Therefore, the aerodynamic forcing term is linearized around the static deformed solution $\{\mathbf{x}_0\}$. The absolute displacement vector is written as

$$\{\mathbf{x}\} = \{\mathbf{x}_0\} + \{\mathbf{x}'\}, \quad (2.19)$$

where $\{\mathbf{x}_0\}$ is the static deformed state and $\{\mathbf{x}'\}$ is the displacement perturbation around the static deformed state. Using this relation, the scalar aerodynamic forcing functions can

be linearized by a Taylor expansion and neglecting higher order terms. For example, the linearized forcing function F_1 is given by the following expression

$$\begin{aligned}
F_1(\mathbf{x}, \dot{\mathbf{x}}, \ddot{\mathbf{x}}) - F_1(\mathbf{x}_0) &\approx \left. \frac{\partial F_1}{\partial x_1} \right|_s x'_1 + \left. \frac{\partial F_1}{\partial x_2} \right|_s x'_2 + \left. \frac{\partial F_1}{\partial x_3} \right|_s x'_3 + \dots + \left. \frac{\partial F_1}{\partial x_n} \right|_s x'_n + \\
&+ \left. \frac{\partial F_1}{\partial \dot{x}_1} \right|_s \dot{x}'_1 + \left. \frac{\partial F_1}{\partial \dot{x}_2} \right|_s \dot{x}'_2 + \left. \frac{\partial F_1}{\partial \dot{x}_3} \right|_s \dot{x}'_3 + \dots + \left. \frac{\partial F_1}{\partial \dot{x}_n} \right|_s \dot{x}'_n + \\
&+ \left. \frac{\partial F_1}{\partial \ddot{x}_1} \right|_s \ddot{x}'_1 + \left. \frac{\partial F_1}{\partial \ddot{x}_2} \right|_s \ddot{x}'_2 + \left. \frac{\partial F_1}{\partial \ddot{x}_3} \right|_s \ddot{x}'_3 + \dots + \left. \frac{\partial F_1}{\partial \ddot{x}_n} \right|_s \ddot{x}'_n.
\end{aligned} \tag{2.20}$$

The partial derivatives, also referred to as linearized coefficients, are evaluated at the steady state solution (i.e. the static deformed solution). They represent a change of the force on the 1st degree of freedom as a result of the individual change in displacement, velocity and acceleration of all the degrees of freedom. In the same way, all the forcing functions can be linearized. Substituting the linearized expressions of all the forcing terms in the expression for the aerodynamic forcing given by Equation 2.18, the RHS of Equation 2.17 can be written as follows

$$\begin{aligned}
\{\mathbf{F}(\mathbf{x}, \dot{\mathbf{x}}, \ddot{\mathbf{x}})\} &\approx \{\mathbf{F}(\mathbf{x}_0)\} + \underbrace{\begin{bmatrix} \left. \frac{\partial F_1}{\partial x_1} \right|_s & \dots & \left. \frac{\partial F_1}{\partial x_n} \right|_s \\ \vdots & \ddots & \vdots \\ \left. \frac{\partial F_n}{\partial x_1} \right|_s & \dots & \left. \frac{\partial F_n}{\partial x_n} \right|_s \end{bmatrix}}_{[K_a]} \begin{Bmatrix} x'_1 \\ \vdots \\ x'_n \end{Bmatrix} + \\
&+ \underbrace{\begin{bmatrix} \left. \frac{\partial F_1}{\partial \dot{x}_1} \right|_s & \dots & \left. \frac{\partial F_1}{\partial \dot{x}_n} \right|_s \\ \vdots & \ddots & \vdots \\ \left. \frac{\partial F_n}{\partial \dot{x}_1} \right|_s & \dots & \left. \frac{\partial F_n}{\partial \dot{x}_n} \right|_s \end{bmatrix}}_{[C_a]} \begin{Bmatrix} \dot{x}'_1 \\ \vdots \\ \dot{x}'_n \end{Bmatrix} + \underbrace{\begin{bmatrix} \left. \frac{\partial F_1}{\partial \ddot{x}_1} \right|_s & \dots & \left. \frac{\partial F_1}{\partial \ddot{x}_n} \right|_s \\ \vdots & \ddots & \vdots \\ \left. \frac{\partial F_n}{\partial \ddot{x}_1} \right|_s & \dots & \left. \frac{\partial F_n}{\partial \ddot{x}_n} \right|_s \end{bmatrix}}_{[M_a]} \begin{Bmatrix} \ddot{x}'_1 \\ \vdots \\ \ddot{x}'_n \end{Bmatrix},
\end{aligned} \tag{2.21}$$

where $[M_a]$, $[C_a]$ and $[K_a]$ are the aerodynamic mass, damping and stiffness matrices, respectively. $\{\mathbf{F}(\mathbf{x}_0)\}$ is the resultant force vector at the static steady state of the 3D wing composed of gravity and the steady state aerodynamic forces and moments. Substituting Equation 2.19 into the LHS of Equation 2.17 and substituting Equation 2.21 into the RHS of Equation 2.17 results in the following

$$\begin{aligned}
[M_s]\{\ddot{\mathbf{x}}_0 + \ddot{\mathbf{x}}'\} + [C_s]\{\dot{\mathbf{x}}_0 + \dot{\mathbf{x}}'\} + [K_s]\{\mathbf{x}_0 + \mathbf{x}'\} &= \\
= \{\mathbf{F}(\mathbf{x}_0)\} + [M_a]\{\ddot{\mathbf{x}}'\} + [C_a]\{\dot{\mathbf{x}}'\} + [K_a]\{\mathbf{x}'\}.
\end{aligned} \tag{2.22}$$

Note that the velocity and acceleration of the initial statically deformed wing (i.e. $\{\dot{\mathbf{x}}_0\}$ and $\{\ddot{\mathbf{x}}_0\}$) is zero. Furthermore, term $[K_s]\{\mathbf{x}_0\}$ is equal to $\{\mathbf{F}(\mathbf{x}_0)\}$ at the initial steady state. As such, Equation 2.22 reduces to

$$[M_s]\{\ddot{\mathbf{x}}'\} + [C_s]\{\dot{\mathbf{x}}'\} + [K_s]\{\mathbf{x}'\} = [M_a]\{\ddot{\mathbf{x}}'\} + [C_a]\{\dot{\mathbf{x}}'\} + [K_a]\{\mathbf{x}'\}. \quad (2.23)$$

In Equation 2.23, only the linearized coefficients (i.e. partial derivatives) of the aerodynamic mass, damping and stiffness matrices remain unknown. However, to determine all the coefficients would be impractical due to the large number of degrees of freedom n . Therefore, modal analysis is used to rewrite the EOM given by Equation 2.23 as a set of modal equations in which only the first k eigenmodes are taken into account, where $k \ll n$. As such, the aerodynamic (and structural) matrices will reduce from $n \times n$ matrices to $k \times k$ matrices (as is shown below), resulting in a significant reduction of partial derivatives that need to be computed in order to build the linearized aerodynamic model. To derive the modal equation, first the displacement $\{\mathbf{x}'\}$, velocity $\{\dot{\mathbf{x}}'\}$ and acceleration $\{\ddot{\mathbf{x}}'\}$ are written as the sum of eigenvectors in the following form

$$\{\mathbf{x}'\} = [\Phi]\{\mathbf{a}\}; \quad \{\dot{\mathbf{x}}'\} = [\Phi]\{\dot{\mathbf{a}}\}; \quad \{\ddot{\mathbf{x}}'\} = [\Phi]\{\ddot{\mathbf{a}}\}, \quad (2.24)$$

where $\{\mathbf{a}\}$ is the amplitude function and is purely a function of time. $[\Phi]$ is a matrix of orthonormal eigenvectors of the system. There are as many eigenmodes (and hence eigenvectors & eigenfrequencies) as there are degrees of freedom. Usually the number of degrees of freedom (i.e. eigenmodes) range into the thousands, but for an adequate analysis using the modal system of equation a set of the first 10 or 20 eigenmodes will suffice (Weisshaar, 2017). The resulting eigenmodes have higher eigenfrequencies that would damp out quickly in reality and as a result would not significantly influence the vibration motion. Therefore, instead of the matrix $[\Phi]$ consisting of n eigenvectors it will contain only k eigenvectors, resulting in a $n \times k$ matrix. The set of n eigenvectors are found by using the free vibration version of Equation 2.23 shown below

$$[M_s]\{\ddot{\mathbf{x}}'\} + [K_s]\{\mathbf{x}'\} = \{\mathbf{0}\}; \quad \{\mathbf{x}'\} = \sum_{i=1}^n \{\Phi_i\} e^{i\omega_i t}, \quad (2.25)$$

where the solution is defined by the second relation (Inman and Singh, 1994). Note that the exclusion of the structural damping term will not change the system eigenfrequencies and eigenvectors. Substituting the solution into the free vibration system and after some mathematical manipulation, an asymmetric eigenvalue problem is obtained

$$\omega^2 \{\Phi\} = [M_s]^{-1} [K_s] \{\Phi\}, \quad (2.26)$$

where the eigenfrequencies and eigenvectors stem from the matrix $[M_s]^{-1}[K_s]$. Each eigenvector $\{\Phi_i\}$ needs to be normalized by scaling it with its corresponding $\alpha_i=1/\sqrt{\{\Phi_i\}^T[M_s]\{\Phi_i\}}$. As such, an orthonormal set of n eigenvectors with respect to the structural mass matrix is obtained (Inman and Singh, 1994). However, only a set of k orthonormal eigenvectors is considered and form the matrix of eigenvectors in the relations given by Equation 2.24. The displacement, velocity and acceleration vectors of Equation 2.24 are then substituted in the EOM given by Equation 2.23. Finally, this system of EOM is multiplied by $[\Phi]^T$ to obtain the following system of equations

$$\begin{aligned} & [\Phi]^T[M_s][\Phi]\{\ddot{\mathbf{a}}\} + [\Phi]^T[C_s][\Phi]\{\dot{\mathbf{a}}\} + [\Phi]^T[K_s][\Phi]\{\mathbf{a}\} = \\ & = [\Phi]^T[M_a][\Phi]\{\ddot{\mathbf{a}}\} + [\Phi]^T[C_a][\Phi]\{\dot{\mathbf{a}}\} + [\Phi]^T[K_a][\Phi]\{\mathbf{a}\}. \end{aligned} \quad (2.27)$$

This is a system of k modal equations. It can be written in its final form as

$$[\tilde{M}_s]\{\ddot{\mathbf{a}}\} + [\tilde{C}_s]\{\dot{\mathbf{a}}\} + [\tilde{K}_s]\{\mathbf{a}\} = [\tilde{M}_a]\{\ddot{\mathbf{a}}\} + [\tilde{C}_a]\{\dot{\mathbf{a}}\} + [\tilde{K}_a]\{\mathbf{a}\}, \quad (2.28)$$

where the structural modal matrices $[\tilde{M}_s]$, $[\tilde{C}_s]$ and $[\tilde{K}_s]$ and the aerodynamic modal matrices $[\tilde{M}_a]$, $[\tilde{C}_a]$ and $[\tilde{K}_a]$ are

$$\begin{aligned} [\tilde{M}_s] &= [\Phi]^T[M_s][\Phi] = \text{diag}(1); & [\tilde{M}_a] &= [\Phi]^T[M_a][\Phi] = \begin{bmatrix} \left. \frac{\partial F_1}{\partial \tilde{a}_1} \right|_s & \cdots & \left. \frac{\partial F_1}{\partial \tilde{a}_k} \right|_s \\ \vdots & \ddots & \vdots \\ \left. \frac{\partial F_k}{\partial \tilde{a}_1} \right|_s & \cdots & \left. \frac{\partial F_k}{\partial \tilde{a}_k} \right|_s \end{bmatrix}; \\ [\tilde{C}_s] &= [\Phi]^T[C_s][\Phi] = \text{diag}(c_k); & [\tilde{C}_a] &= [\Phi]^T[C_a][\Phi] = \begin{bmatrix} \left. \frac{\partial F_1}{\partial \tilde{a}_1} \right|_s & \cdots & \left. \frac{\partial F_1}{\partial \tilde{a}_k} \right|_s \\ \vdots & \ddots & \vdots \\ \left. \frac{\partial F_k}{\partial \tilde{a}_1} \right|_s & \cdots & \left. \frac{\partial F_k}{\partial \tilde{a}_k} \right|_s \end{bmatrix}; \\ [\tilde{K}_s] &= [\Phi]^T[K_s][\Phi] = \text{diag}(\omega_k^2); & [\tilde{K}_a] &= [\Phi]^T[K_a][\Phi] = \begin{bmatrix} \left. \frac{\partial F_1}{\partial a_1} \right|_s & \cdots & \left. \frac{\partial F_1}{\partial a_k} \right|_s \\ \vdots & \ddots & \vdots \\ \left. \frac{\partial F_k}{\partial a_1} \right|_s & \cdots & \left. \frac{\partial F_k}{\partial a_k} \right|_s \end{bmatrix}. \end{aligned} \quad (2.29)$$

The property of eigenvectors are that they are orthonormal with respect to the mass matrix. This results in the diagonalization of the structural modal matrices, where the structural mass matrix is an identity matrix, the structural damping matrix is a diagonal matrix containing the modal damping coefficients and the structural stiffness matrix is a diagonal matrix containing

the square of the modal eigenfrequencies. Usually the modal damping coefficients, obtained from experience or measurements (Inman and Singh, 1994), are fed direct into the modal damping matrix.

The modal aerodynamic matrices are rarely diagonal, and as a result they prevent the EOM given by Equation 2.28 to fully decouple. The full derivations of the modal aerodynamic matrices are shown in Appendix A. The interpretation of the coefficients are slightly different than those seen in Equation 2.21. For example, each column in the aerodynamic modal mass matrix represent the change in the force on a specific mode as result of the change in acceleration of *all* the considered modes. So, $\frac{\partial F_1}{\partial \ddot{a}_1} \Big|_s$ represents a change of the force on mode 1 as a result of the change in acceleration of mode 1, while $\frac{\partial F_1}{\partial \ddot{a}_k} \Big|_s$ represents a change of the force on mode 1 as a result of the change in acceleration of mode k (i.e. the last mode considered). The second column would represent the change of the force on mode 2 as a result of the change in acceleration of *all* the considered modes, and so on. Finally, the columns in the modal damping and stiffness matrix represent the change of the force on a specific mode as a result of the change in velocity and displacement of *all* the considered modes, respectively. Note that the perturbations of the acceleration, velocity and displacement are from the steady state condition.

In order to clearly underline the advantage of modal analysis, note that Equation 2.28 is a modal system of k equations where as Equation 2.23 is a system of n equations ($k \ll n$). Carrying out computations with the modal system, the unknown coefficients present in the aerodynamic modal matrices decrease from $3n^2$ to $3k^2$.

Once the linearized coefficients (i.e. partial derivatives) are found, the aerodynamic forcing term should be able to model arbitrary perturbations of the system about the linearized steady state, as long as the perturbations are small such that the flow is of linear nature.

2.4.1 Coefficient Extraction Method: Theory

In order to be able to carry out a modal analysis, the coefficients that compose the aerodynamic matrices in Equation 2.28 must be computed. Note that the RHS of Equation 2.28 is obtained by substituting the relations given by Equation 2.24 into Equation 2.21 and then multiplying the same equation with $[\Phi]^T$, where $[\Phi]^T$ is an $n \times k$ matrix. Therefore, the following relation holds true

$$[\Phi]^T \{ \mathbf{F}(\mathbf{x}, \dot{\mathbf{x}}, \ddot{\mathbf{x}}) \} - \{ \mathbf{F}(\mathbf{x}_0) \} \approx [\tilde{M}_a] \{ \ddot{\mathbf{a}} \} + [\tilde{C}_a] \{ \dot{\mathbf{a}} \} + [\tilde{K}_a] \{ \mathbf{a} \}. \quad (2.30)$$

Multiplying the force vector with the transpose of the eigenvector matrix maps the resultant force vector on each considered mode. This results in a $k \times 1$ vector. This equation represents the linearized force vector in terms of modal variables, while in Equation 2.21 it represented in terms of degrees of freedom.

In order to extract the unknown coefficients, unsteady CFD simulations are used. Each mode is perturbed from the steady state with a specific amplitude function $a(t)$ for a specific number of time steps. Three time steps is the minimum required. For example, a perturbation only in the first mode of the structure reduces Equation 2.30 to

$$\{\mathbf{F}(\mathbf{a}, \dot{\mathbf{a}}, \ddot{\mathbf{a}})\} - \{\mathbf{F}(\mathbf{a}_0)\} \approx \begin{Bmatrix} \frac{\partial F_1}{\partial \ddot{a}_1} \Big|_s \\ \vdots \\ \frac{\partial F_k}{\partial \ddot{a}_1} \Big|_s \end{Bmatrix} \ddot{a}_1(t) + \begin{Bmatrix} \frac{\partial F_1}{\partial \dot{a}_1} \Big|_s \\ \vdots \\ \frac{\partial F_k}{\partial \dot{a}_1} \Big|_s \end{Bmatrix} \dot{a}_1(t) + \begin{Bmatrix} \frac{\partial F_1}{\partial a_1} \Big|_s \\ \vdots \\ \frac{\partial F_k}{\partial a_1} \Big|_s \end{Bmatrix} a_1(t), \quad (2.31)$$

where the LHS represents the modal forces computed at a specific perturbed state at time t from the unsteady CFD simulations. At time $t = t_1$, only the coefficients remain unknown. Hence Equation 2.31 gives a system of k modal equations, but with $3k$ coefficients, 3 for each modal equation. To provide enough equations to solve for the unknown coefficients, at least two more time steps are needed. Typically, at least 10 are taken. If there are more equations than unknowns, the least squares method is used to obtain the coefficients. Having said this, the coefficients that make up the first column of the aerodynamic mass, damping and stiffness matrix can be computed. Perturbing the structure in mode 2 will give the coefficients of the second column and so on until all the coefficients are found.

In principle, the amplitude function a can be any function of t as long as its first and second derivatives are non-zero. This will ensure that the displacement, velocity and acceleration effects are considered when extracting the coefficients for the linearized model.

Finally, a detailed procedure of this theory is shown in Chapter 6, where the unsteady aerodynamic results that the linearized model gives are evaluated.

2.4.2 Flutter Prediction

Once the coefficients comprising the aerodynamic matrices are found, the system of k modal equations, given by Equation 2.28, is fully defined. Note that the aerodynamic coefficients are found for a specific Reynolds and Mach number and are valid only at these flow parameters. Therefore, using Equation 2.28, an eigenvalue analysis or a numerical transient simulation can be carried out in order to monitor the response and see whether flutter occurs. In order to carry out such an analysis, Equation 2.28 has to be re-written in the space state form (Inman and Singh, 1994). First, Equation 2.28 is written in the following form

$$\{\ddot{\mathbf{a}}\} = -[\tilde{M}]^{-1}[\tilde{C}]\{\dot{\mathbf{a}}\} - [\tilde{M}]^{-1}[\tilde{K}]\{\mathbf{a}\}, \quad (2.32)$$

where $[\tilde{M}] = [\tilde{M}_s] - [\tilde{M}_a]$, $[\tilde{C}] = [\tilde{C}_s] - [\tilde{C}_a]$ and $[\tilde{K}] = [\tilde{K}_s] - [\tilde{K}_a]$.

To transform 2.32 into a first order vector differential equation, the following relations are assumed

$$\{\mathbf{y}_1\} = \{\mathbf{a}\}; \quad \{\mathbf{y}_2\} = \{\dot{\mathbf{a}}\}. \quad (2.33)$$

In Equation 2.33 $\{\mathbf{y}_1\}$ and $\{\mathbf{y}_2\}$, like $\{\mathbf{a}\}$, are only a function of time. Differentiating the two vectors with respect to time results in

$$\{\dot{\mathbf{y}}_1\} = \{\dot{\mathbf{a}}\} = \{\mathbf{y}_2\}; \quad \{\dot{\mathbf{y}}_2\} = \{\ddot{\mathbf{a}}\} = -[\tilde{M}]^{-1}[\tilde{C}]\{\mathbf{y}_2\} - [\tilde{M}]^{-1}[\tilde{K}]\{\mathbf{y}_1\}. \quad (2.34)$$

The coupled system given by the relations above is written in its final space state form as

$$\begin{Bmatrix} \dot{\mathbf{y}}_1 \\ \dot{\mathbf{y}}_2 \end{Bmatrix} = \begin{bmatrix} [0] & [I] \\ -[\tilde{M}]^{-1}[\tilde{K}] & -[\tilde{M}]^{-1}[\tilde{C}] \end{bmatrix} \begin{Bmatrix} \mathbf{y}_1 \\ \mathbf{y}_2 \end{Bmatrix} \quad or \quad \{\dot{\mathbf{y}}\} = [A]\{\mathbf{y}\}, \quad (2.35)$$

where the state $[A]$ matrix is a $2k \times 2k$ matrix. The four matrices that compose the $[A]$ matrix are all $k \times k$ matrices. The vector $\{\mathbf{y}\}$ is a $2k \times 1$ state vector. Assuming the solution $\{\mathbf{y}\} = \{\mathbf{z}\}e^{\lambda t}$ and substituting it into Equation 2.35 results in

$$[I\lambda - [A]]\{\mathbf{z}\}e^{\lambda t} = \{\mathbf{0}\} \quad or \quad [A]\{\mathbf{z}\} = \lambda\{\mathbf{z}\}, \quad (2.36)$$

The relations given by Equation 2.36 represent the standard algebraic eigenvalue problem (Inman and Singh, 1994; Wright and Cooper, 2008). For an oscillatory system, there are $2k$ eigenvalues λ of the state matrix $[A]$ which occur in complex conjugate pairs (Frazer et al., 1938; Collar and Simpson, 1987; Inman and Singh, 1994) as is shown below

$$\lambda_j = -\zeta_j\omega_j \pm i\omega_j\sqrt{1 - \zeta_j^2}, \quad j = 1, 2, \dots, k \quad (2.37)$$

where $i = \sqrt{-1}$ and k is the number of modes. Note that even though there are $2k$ eigenvalues, since they occur in complex conjugate pairs, there will be only k natural frequencies ω_j corresponding to each mode. Furthermore, there are also only k damping ratios ζ_j , corresponding to each mode. If the damping ratio $\zeta_j > 0$, the system oscillations are damped. For $\zeta_j < 0$, the system oscillations are amplified (i.e. flutter occurs). The formulae for computing the damping ratios and natural frequencies are given below

$$\omega_j = \sqrt{\text{Re}(\lambda_j)^2 + \text{Im}(\lambda_j)^2}; \quad \zeta_j = -\frac{\text{Re}(\lambda_j)}{\sqrt{\text{Re}(\lambda_j)^2 + \text{Im}(\lambda_j)^2}}. \quad (2.38)$$

Note for this eigenvalue analysis, initial boundary conditions are irrelevant when determining whether the system is stable or not. If the actual response due to a specific set of boundary conditions is of interest, the system of equations given by Equation 2.35 must be numerically integrated with respect to time using, for example, the Runge-Kutta 4th order method.

2.4.3 Gust Response Analysis

In order to conduct a gust response analysis, a modal gust forcing term is added to the RHS of Equation 2.32. The resulting system of modal equations are given below

$$\{\ddot{\mathbf{a}}\} = -[\tilde{M}]^{-1}[\tilde{C}]\{\dot{\mathbf{a}}\} - [\tilde{M}]^{-1}[\tilde{K}]\{\mathbf{a}\} + [\tilde{M}]^{-1}[\Phi]^T\{\mathbf{f}_{gust}\}, \quad (2.39)$$

where $\{\mathbf{f}_{gust}\}$ is a $n \times 1$ vector containing the force magnitude on all n degrees of freedom at a specific time t . Obviously, this gust vector will change each time step. The gust forcing term is computed using unsteady CFD simulations in the following way: first, the structure is submerged to freestream flow. At a certain time, the boundary conditions are changed such that a vertical gust of a certain profile type is introduced. After a certain amount of time, the boundary conditions are changed to those of the original case and the simulation continues further for a certain number of time steps. During each time step, the force on each degree of freedom of the structure is computed and in that way, the gust forcing term $\{\mathbf{f}_{gust}\}$ at each time step is known. Note that during the simulation, the structure does not deform due to the forces that stem from the applied vertical gust. Assuming linearity of the problem, the gust forcing term can then be added to the system of equations as is shown in Equation 2.39. In order to obtain the gust forcing term acting on each mode (rather than degree of freedom), $\{\mathbf{f}_{gust}\}$ is multiplied by $[\Phi]^T$, a $k \times n$ matrix consisting of k eigenvectors. Finally, the product $[\Phi]^T\{\mathbf{f}_{gust}\}$ becomes a $k \times 1$ vector. Converting Equation 2.39 into the space state form results in the following system

$$\{\dot{\mathbf{y}}\} = [A]\{\mathbf{y}\} + \{\mathbf{f}\}, \quad \text{where} \quad \{\mathbf{f}\} = \left\{ \begin{array}{c} \{\mathbf{0}\} \\ [\tilde{M}]^{-1}[\Phi]^T\{\mathbf{f}_{gust}\} \end{array} \right\}. \quad (2.40)$$

The vector $\{\mathbf{f}\}$ is a $2k \times 1$ vector consisting of a $k \times 1$ zero vector and a $k \times 1$ modal gust forcing term $[\Phi]^T\{\mathbf{f}_{gust}\}$ multiplied by a $k \times k$ matrix denoted as $[\tilde{M}]^{-1}$. The state matrix $[A]$ is identical to that given by Equation 2.35. Equation 2.40 can be numerically integrated with respect to time in order to monitor the structures response due to a vertical gust.

2.5 Concluding Remarks

In this chapter, the aeroelastic system of a 2DOF airfoil and the corresponding EOM are introduced and explained. The expressions of the unsteady aerodynamic forces obtained via Theodorsen are explained and how they can be used to compute the flutter boundary via the classical k method. Furthermore, the linearized aerodynamic model in terms of degrees of freedom n and modal coordinates k is derived. The procedure for computing the partial derivatives, i.e. the linearized coefficients, of the model via unsteady CFD simulations is thoroughly explained. Finally, how the linearized aerodynamic model can be used to compute the flutter boundary and gust response analysis is shown.

The main objective of this author's Master Thesis is to investigate the efficacy of the linearized aerodynamic model for accurately predicting flutter. As such, the model must be able to model unsteady aerodynamic loads for a harmonically oscillating structure. The theoretical basis is laid out in this chapter, while the evaluation of the linearized aerodynamic model is carried out for a 2D airfoil subject to incompressible flow and the results are shown and discussed in Chapter 6.

Computational Fluid Dynamics (CFD)

3.1 Introduction

Computational Fluid Dynamics (CFD) deals with numerically solving the discretized governing fluid dynamics equations. The governing equations can be spatially discretized using the Finite Difference Method (FDM), Finite Element Method (FEM) or Finite Volume Method (FVM). Of these methods, the Finite Volume Method is the most popular industrial method today. It is the basis of the OpenFOAM software that is used in this Master Thesis. In FVM, the integral form of the governing equations are applied to discrete computational cells (i.e. control volumes) within a computational domain and are spatially discretized. This ensures conservative discretization, which is one of the main advantages of the Finite Volume Method (Hirsch, 2007; Ferziger and Peric, 2012). In addition, FVM is easy to implement and can be applied to arbitrary grids. Temporal discretization, for engineering purposes, is typically carried out with an implicit second order accurate numerical scheme, such as BDF2. More information on discretization schemes and solving the discretized system of equations are not presented here but can be found in Hirsch (2007) and Ferziger and Peric (2012).

The focus of this chapter is to introduce the governing fluid dynamics equations and the concept of turbulence modeling. The discretized form of these equations are used for computational analysis. Finally, mesh deformation techniques are discussed since they are needed when motion is imposed upon the 2D airfoil.

3.2 Governing Equations

Typically, the governing equations that describe the fluid dynamics consist of equations for the conservation of mass, conservation of momentum and conservation of energy. In incompressible flows, such as those considered in this Master Thesis, the conservation of mass and momentum equations become independent of the energy equation, i.e. the energy equation decouples. The velocity and pressure field can be solved for by only considering the conservation of mass and momentum equations. The conservation of mass and momentum for an incompressible Newtonian fluid in differential form and written in the Eulerian framework is given by the following two equations

$$\text{Conservation of Mass :} \quad \frac{\partial u_i}{\partial x_i} = 0, \quad (3.1)$$

$$\text{Conservation of Momentum :} \quad \frac{\partial u_i}{\partial t} + u_j \frac{\partial u_i}{\partial x_j} = -\frac{1}{\rho} \frac{\partial p}{\partial x_i} + \nu \frac{\partial^2 u_i}{\partial x_j \partial x_j} + f_i. \quad (3.2)$$

Note that the conservation of momentum equation consists of three scalar equations, i.e. the x , y and z component of the momentum equation. These equations are also referred to as the *Navier-Stokes equations*. A derivation and detailed explanation of Equations 3.1 & 3.2 can be found in any university textbook on fluid dynamics, e.g. [Anderson Jr \(2010\)](#).

3.3 Turbulence Modeling

Theoretically, the *Navier-Stokes equations* along with the continuity equation can be solved numerically and directly, without an appropriate turbulence model. This approach is called Direct Numerical Simulation (DNS). DNS resolves *all* the turbulent length and time scales which implies that the mesh size and time step would need to be sufficiently small. This technique is extremely computationally expensive and is not useful as an engineering approach. However, it is used in research for understanding the fundamental mechanisms of turbulence ([Hirsch, 2007](#)). A less computationally expensive approach is the Large Eddy Simulations (LES) that resolves the largest turbulent length scales and models the smallest ones. The least computationally expensive turbulent modeling approach is Reynolds Averaged Navier-Stokes (RANS) simulations. This is also the least accurate of the methods mentioned, but is still an industrial standard as it provides sufficient accuracy for engineering purposes at a reasonable computational cost. RANS models all the turbulent length scales. This method is used in this Master Thesis and is discussed briefly in the subsequent sections.

3.3.1 Reynolds Averaged Navier-Stokes (RANS)

In order to obtain the governing equations to carry out RANS simulations, the incompressible Navier-Stokes equations as well as the conservation of mass equation are averaged by ensemble such that only the mean component of the physical property in the equations is considered. This process is explained in this section. Any physical property can be decomposed into a mean and fluctuating component about the mean, as is shown by the expression below

$$\phi(\mathbf{x}, t) = \bar{\phi}(\mathbf{x}, t) + \phi'(\mathbf{x}, t). \quad (3.3)$$

This is also referred to as Reynolds decomposition. The physical property can represent components of the velocity vector or the pressure, for example. The mean component $\bar{\phi}(\mathbf{x}, t)$ is defined by ensemble averaging

$$\bar{\phi}(\mathbf{x}, t) = \lim_{N \rightarrow \infty} \frac{1}{N} \sum_{i=1}^N \phi_i(\mathbf{x}, t), \quad (3.4)$$

where N is the number of ensembles, i.e. identically performed experiments (Ferziger and Peric, 2012; Jasak, 1996). Figure 3.1 demonstrates the concept of ensemble averaging. For a specific experiment (e.g. *sample 1*), at a specific location \mathbf{x} , the physical property will change in time, but can be represented as a mean change in time and a fluctuation about the mean value. For another identical experiment (e.g. *sample 2*), the mean change in time will be the same, but the fluctuation will be different and so on. However, averaging over multiple ensembles will cause the fluctuations components to cancel out and the change in the mean value of a physical property to remain, as long as the number of ensembles N is high enough (Ferziger and Peric, 2012). This is also called Reynolds averaging.

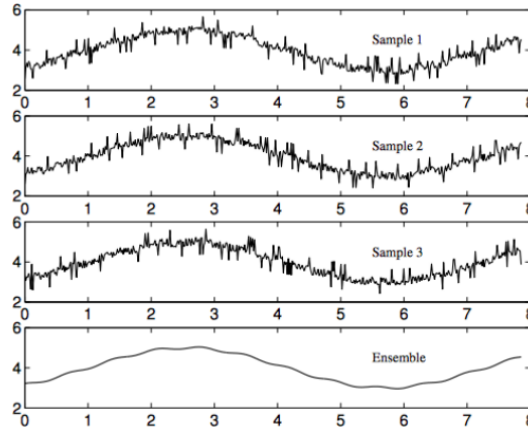


Figure 3.1: Ensemble Averaging of Velocity at a Point in Turbulent Flow (Recktenwald, 2009)

The velocity and pressure are decomposed in the form of Equation 3.3 and substituted in the continuity and Navier-Stokes equations. Reynolds averaging is applied and the resulting equations in terms of means physical quantities are

$$\text{Averaged Conservation of Mass :} \quad \frac{\partial \bar{u}_i}{\partial x_i} = 0, \quad (3.5)$$

$$\text{Averaged Navier - Stokes :} \quad \frac{\partial \bar{u}_i}{\partial t} + \bar{u}_j \frac{\partial \bar{u}_i}{\partial x_j} = -\frac{1}{\rho} \frac{\partial \bar{p}}{\partial x_i} + \nu \frac{\partial^2 \bar{u}_i}{\partial x_j \partial x_j} - \frac{\partial \overline{u'_i u'_j}}{\partial x_j} + f_i. \quad (3.6)$$

From Equation 3.6 it can be seen that there is in fact a fluctuating component in the RANS equations. This is known as the Reynolds or turbulent stress. The averaging process creates more unknowns but without creating additional governing equations. This results in a *closure problem*. Turbulence models are used to apply *closure* to the problem. Similarly to how viscous stresses are proportional to molecular viscosity, Boussinesq provides a approximation for the turbulent shear stress that is proportional to the eddy or turbulent viscosity ν_t (Boussinesque, 1877), as is shown below

$$-\overline{u'_i u'_j} = \nu_t \left(\frac{\partial \bar{u}_i}{\partial x_j} + \frac{\partial \bar{u}_j}{\partial x_i} \right) - \frac{2}{3} \delta_{ij} k, \quad (3.7)$$

where k is the turbulent kinetic energy $u'_i u'_i / 2$. Unlike molecular viscosity, turbulent viscosity is not a property of the fluid but of the flow. Turbulent flow leads to chaotic mixing that increases the diffusion of the flow physical properties, which is modeled by the eddy viscosity.

Typically, the eddy viscosity is modeled as a function of the turbulent kinetic energy k and the turbulence dissipation rate ϵ . Instead of ϵ , the specific turbulence dissipation rate ω can be used, where $\omega = \epsilon/k$. Popular turbulence models for modeling the turbulent viscosity are Spalart-Allmaras, standard k - ϵ , RNG k - ϵ , standard Wilcox k - ω , k - ω SST and k - k_l - ω . Of all the turbulence models mentioned, the most popular model in the industry is Menter's k - ω SST (Menter, 1994). The k - ω SST is used in this Master Thesis and is briefly outlined in the following subsection.

3.3.2 Turbulence Models: k - ω SST

The k - ω SST is a blend of the standard k - ω turbulence model and the standard k - ϵ turbulence model as is briefly explained in this section. The k - ϵ model is robust, reasonably accurate and insensitive to freestream parameters. However, it does not provide accurate results for flows with high adverse pressure gradients and separated flows. On the other hand, the standard

k - ω model shows superior performance for wall-bounded flows and flows with high adverse pressure gradient and/or separation. However, the model is overly sensitive to the freestream value of ω (Menter, 1993). Therefore, Menter (1993) suggested to combine the two models such that the advantages of both are utilized. In the first 50% of the boundary layer, the standard k - ω model of Wilcox is used, after which the model changes gradually to that of the standard k - ϵ towards the boundary layer edge. Note that a k - ω formulation of the k - ϵ model is used. Furthermore, based on the success of the Johnson-King model (Johnson and King, 1985), the eddy viscosity formulations of the k - ω SST model takes into account the principal turbulent shear stress in the adverse pressure gradient regions (Menter, 1993, 1994). This further increases the ability of the model to accurately predict flows with adverse pressure gradients and separation. For more in depth description of the model, see Menter (1994).

3.4 Mesh Deformation Methods

In Fluid-Structure Interaction (FSI) problems, as the structure deforms, the fluid mesh must change. In this Master Thesis, the structure (i.e. airfoil) moves as a result of imposed motion and not as a result of the forces acting on it. One approach is to completely regenerate the computational fluid grid in each time step. However, this has large computational requirements and requires user interaction. Since the mesh would have to be regenerated every time step, a method that can solve this problem automatically is required. Furthermore, the physical conservation laws are not satisfied when a new mesh is generated because physical quantities have to be interpolated from the old mesh to the new mesh (van Zuijlen, 2008). Instead of regenerating the mesh each time step, deforming the mesh is used as a better approach. There are various mesh deformation techniques found in literature, some of which will be discussed in this section.

Mesh deformation based on springs can be used for handling moderate deformations and for structured & unstructured meshes (van Zuijlen, 2008). One such method is the lineal spring analogy method that connects the internal grid point with fictitious springs of a specific stiffness. An equilibrium state is found by performing a force balance on the system of spring elements, where the equilibrium length is equal to the initial length of the spring segments. This mesh deformation method can be improved by additional torsional springs at the mesh vertices. This prevents neighbouring triangles or tetrahedrons from intersecting each other (van Zuijlen, 2008). This is called the torsional spring analogy method (Farhat et al., 1998; Degand and Farhat, 2002). Finally, there exists a semi-torsional spring analogy model similar to the lineal method but with angle information included when computing the spring stiffness (Blom, 2000; Zeng and Ethier, 2005). This model requires less computational effort than the torsional spring analogy method. Furthermore, all these models mentioned suffer from the appearance of hanging nodes that must be removed (van Zuijlen, 2008). Other mesh deformation methods include the least squares method (Wick, 2001), the solid body elasticity approach (Lynch and O'Neill, 1980), laplacian smoothing (Helenbrook, 2003) and the biharmonic operator (Helenbrook, 2003). Finally, a popular method for deforming a computational fluid grid involves the use of radial basis functions which is discussed in more detail in the following subsection.

3.4.1 Radial Basis Function (RBF) Interpolation as a Mesh Deformation Method

RBF is used to interpolate the deformation of the fluid mesh internal nodes given the displacement of the structural nodes on the interface (van Zuijlen, 2008). The interpolation function, used to compute the displacement of the computational mesh, is approximated as the sum of basis functions as is shown below

$$s(\mathbf{x}) = \sum_{j=1}^{n_b} \gamma_j \phi(\|\mathbf{x} - \mathbf{x}_{b_j}\|) + p(\mathbf{x}), \quad (3.8)$$

where $\mathbf{x}_{b_j} = [x_{b_j}, y_{b_j}, z_{b_j}]$ are the centers in which the displacements are known. The number of boundary nodes present is equal to n_b , the radial basis function used is defined by ϕ and $p(\mathbf{x})$ is a polynomial. The following interpolation conditions are used to determine the coefficients γ_j and the polynomial p (De Boer et al., 2007b)

$$s(\mathbf{x}_{b_j}) = \mathbf{d}_{b_j}, \quad (3.9)$$

where \mathbf{d}_{b_j} is a vector of displacement for each boundary point. The second requirement is that the following relation is satisfied

$$\sum_{j=1}^{n_b} \gamma_j q(\mathbf{x}_{b_j}) = 0, \quad (3.10)$$

where q is a polynomial with a degree less than or equal to that of polynomial p . The radial basis function defines the minimal degree of the polynomial p (van Zuijlen, 2008). If the radial basis functions are positive definite and have a degree of less than or equal to 2, linear polynomials for p and hence q can be used (Beckert and Wendland, 2001). All the RBF's mentioned in this section satisfy this criterion. The two aforementioned requirements are put in matrix form as follows

$$\begin{Bmatrix} \mathbf{d}_b \\ 0 \end{Bmatrix} = \begin{bmatrix} [\phi_{b,b}]_{n_b \times n_b} & [P_b]_{n_b \times 4} \\ [P_b^T]_{4 \times n_b} & [0]_{4 \times 4} \end{bmatrix} \begin{Bmatrix} \boldsymbol{\gamma} \\ \boldsymbol{\beta} \end{Bmatrix}, \quad (3.11)$$

where $\boldsymbol{\gamma}$ is a vector of coefficients γ_j and $\boldsymbol{\beta}$ is a vector of coefficients of the linear polynomial p . The matrix $[\phi_{b,b}]$ is the evaluation of the basis function $\phi_{b_i b_j} = \phi(\|\mathbf{x}_{b_i} - \mathbf{x}_{b_j}\|)$ and $[P_b]$ is

a matrix with each row j given by $[1 \ x_{b_j} \ y_{b_j} \ z_{b_j}]$. From Equation 3.11, three sets of γ and β coefficients are computed, a set for the displacements \mathbf{d}_b in the x direction (i.e. $\mathbf{d}_{b,x}$), a set for the displacements \mathbf{d}_b in the y direction (i.e. $\mathbf{d}_{b,y}$) and a set for the displacements \mathbf{d}_b in the z direction (i.e. $\mathbf{d}_{b,z}$). With each set of γ and β coefficients, the displacement in the x , y , and z direction of the internal nodes can be computed by evaluating the interpolation function give by Equation 3.8 at the internal nodes $\mathbf{x}_{in_j} = [x_{in_j}, y_{in_j}, z_{in_j}]$, as is shown below

$$\mathbf{d}_{in_j} = s(\mathbf{x}_{in_j}). \quad (3.12)$$

This expression in matrix form is the following

$$\mathbf{d}_b = \left[[\phi_{in,b}]_{n_{in} \times n_b} \quad [P_{in}]_{n_{in} \times 4} \right] \begin{Bmatrix} \gamma \\ \beta \end{Bmatrix}, \quad (3.13)$$

where n_{in} is the number of internal nodes. The matrix $[\phi_{in,b}]$ is the evaluation of the basis function $\phi_{in_i b_j} = \phi(\|\mathbf{x}_{in_i} - \mathbf{x}_{b_j}\|)$ and $[P_{in}]$ is a matrix with each row j given by $[1 \ x_{in_j} \ y_{in_j} \ z_{in_j}]$.

The radial basis function that can be used are either those of compact support or functions with global support. Compact support functions have a support radius r that defines the area in which the internal points are influenced by the structural deformation. Outside that area, the internal points stay at their initial position regardless of the severity of the structural deformation. Furthermore, when functions with global support are used, each internal grid point in the fluid computational domain is affected by the deformation of the structure. The two functions that give the best quality deformed meshes are the C^2 continuous basis function with compact support (CP C^2) and the Thin Plate Spline (TPS, global support) function shown below respectively,

$$\phi\left(\frac{x}{r}\right) = \left[1 - \left(\frac{x}{r}\right)^4\right] \left[4\left(\frac{x}{r}\right) + 1\right] \quad \text{and} \quad \phi(x) = x^2 \ln(x). \quad (3.14)$$

In this Master Thesis, the global radial basis function IMQB (inverse multiquadratic biharmonics) is utilized since it is available in the foam-extend 3.2 framework. The IMQB radial basis function is given by the following formula

$$\phi(x) = \frac{1}{a^2 + x^2}. \quad (3.15)$$

Note that a is a parameter that controls the shape of the radial basis function (van Zuijlen, 2008). Typically, the values chosen for this parameter are in the range 10^{-5} to 10^{-3} (De Boer et al., 2007b).

3.5 Concluding Remarks

In this chapter, the fundamental tools used in CFD were introduced. The governing equations, i.e. the mass continuity and conservation of momentum, for incompressible flow were given. Furthermore, the averaging of these conservation laws was explained as well as the need for the turbulence modeling of the fluctuating term that arises in the *Reynolds Averaged Navier Stokes Equations*. The k - ω SST turbulence model used in this Master Thesis was briefly introduced. Finally, mesh deformation methods based on radial basis functions were explained, since they are used for deforming the mesh during unsteady CFD simulations where motion of the 2D airfoil is imposed.

Chapter 4

Computational Setup

4.1 Introduction

This chapter presents the computational setup for carrying out the steady and unsteady CFD simulations of this Master Thesis. The mesh strategy is discussed and the mesh convergence tests are shown. The pressure, velocity and turbulent boundary conditions of the utilized k - ω SST model are given. In addition, the numerical schemes and the solver used are presented. Furthermore, the CFD simulations carried out during this Master Thesis are done on a NACA 0009 airfoil submerged in incompressible flow at a freestream Reynolds number of 10^6 . The reasoning behind choosing the NACA 0009 airfoil and the specific freestream flow parameters is also explained in this chapter.

4.2 NACA 0009 Airfoil

The main aim of this Master Thesis is to validate the use of a linearized aerodynamic CFD model in predicting unsteady aerodynamic characteristics of harmonically oscillating airfoils. Its accuracy is analyzed partly by comparing the results with Theodorsen's unsteady aerodynamic coefficients (Theodorsen, 1935). Since these expressions were derived for a flat plate (Dimitradis, 2018), where the flow is attached and thus linear, it would be logical to use a flat plate as a geometry upon which the CFD simulations are carried out. However, the flat plate has a blunt leading and trailing edge. The blunt leading edge would cause convergence issues and if it converged at all, flow separation in the vicinity of the leading edge would occur for small angles of attack, causing it to deviate from the linear regime. Hence, the idea is to choose an airfoil which displays the same aerodynamic behaviour as the flat plate but does not trigger separation due to its curved leading edge. Therefore, the NACA 0009 airfoil is chosen. As such, like the flat plate, it gives zero lift for a zero angle of attack and its moment coefficient is zero at the aerodynamic center. Its $\partial c_l / \partial \alpha$ is approximately the 2π value as cal-

culated by Thin Airfoil Theory (Katz and Plotkin, 2001) for a flat plate. Figure 4.2 depicts the lift-curve slope per degree for different types of NACA airfoils and for different thickness. In addition, a smooth and rough airfoil surface is considered. The Reynolds number is $6 \cdot 10^6$ and the lift-curve slope is measured about the design lift coefficient value of wing sections (Abbott and Von Doenhoff, 1959). This lift coefficient is approximately in the center of the NACA 6-series low-drag range. It is clear that for a NACA 0009 airfoil, the slope is ≈ 0.1097 (i.e. 2π). The coordinates of the NACA 0009 airfoil of unit length are taken from Airfoil Tools Database (airfoiltools.com, 2018) and the profile shape is shown in Figure 4.1 below.

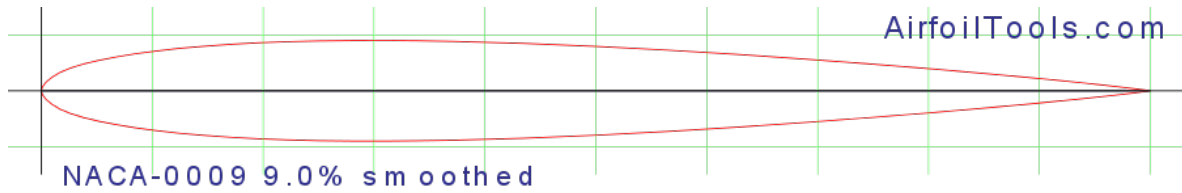


Figure 4.1: NACA 0009 Airfoil (airfoiltools.com, 2018)

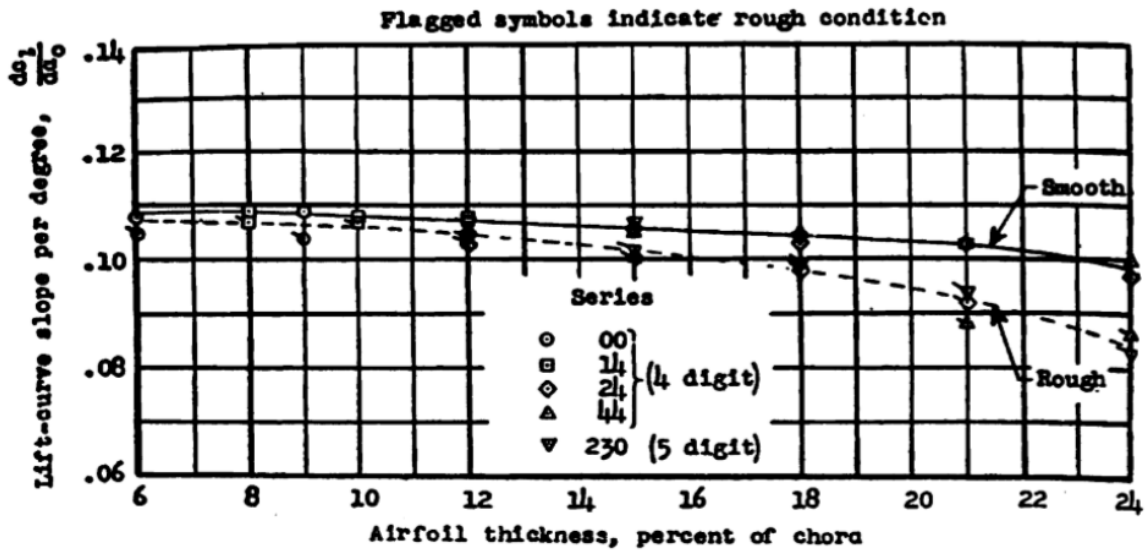


Figure 4.2: $\partial c_l / \partial \alpha$ for Different NACA Airfoil Thickness/Type (Abbott and Von Doenhoff, 1959)

4.3 Flow Parameters: The Reynolds Number

The resultant aerodynamic force on a given airfoil of chord c can be written in functional form as (Leishman, 2006)

$$\frac{F}{\rho V^2 c^2} = f(Re, Ma, k). \quad (4.1)$$

Within the scope of this Master Thesis only incompressible flow is considered. Since the solvers used in OpenFOAM are incompressible it implies that $Ma \equiv 0$. It is important that the aerodynamic steady state lift polars of the NACA 0009 exhibit the same behaviour as that of a flat plate, meaning that its lift-curve slope should be $\approx 2\pi$. For steady state flows, the lift depends only on the Reynolds Number (since $k = 0$). Therefore, a high enough Reynolds number must be chosen such that the airfoil displays linear behaviour for smaller angles of attack but not too high such that the computational mesh for the airfoil becomes so large that the CFD simulations become computationally expensive, particularly for unsteady scenarios.

Reynolds Number Effects

For lower Reynolds numbers, the airfoil deviates from its linear regime and displays nonlinearities in lift that are called low Reynolds number effects. This can be seen in Figure 4.3 below, where lift polars for Reynolds numbers of 100,000, 1,000,000 and 10,000,000. The polars were computed using XFOIL (Drela, 1989) without tripping the boundary layer and thus letting its boundary layer naturally transition from laminar to turbulent. Clearly, the lift polar of $Re = 100,000$ is most effected by the Reynolds number effects. The Reynolds number effects are a result of the laminar boundary layer which is very sensitive to adverse pressure gradients and hence prone to transition and separation (Schlichting and Gersten, 2016). For example, for $\alpha = 1^\circ$, the boundary layer is fully laminar; however, separation on the suction side occurs at ≈ 0.65 , resulting in a lower lift value. Increasing the angle of attack results in a laminar separation bubble, where the flow manages to reattach and transition is triggered. Furthermore the LSB changes in length and moves towards to leading edge of the airfoil. These effects result in a nonlinear lift polar. For $Re = 1,000,000$ and $\alpha > 4.5^\circ$ a small LSB forms near the leading edge, which is why the lift polar does not deviate for the linear regime substantially. For $Re = 10,000,000$, the boundary layer transition before a LSB forms and the low Reynolds number effects are completely eliminated.

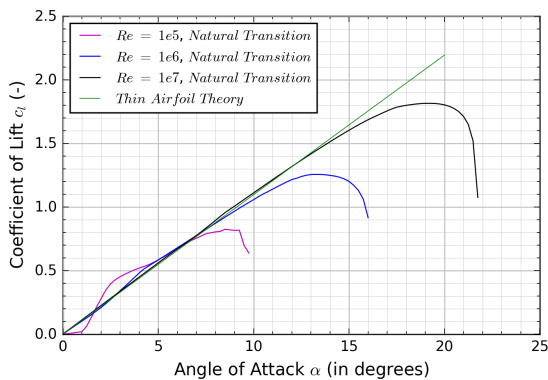


Figure 4.3: XFOIL Lift Polars, Natural Transition

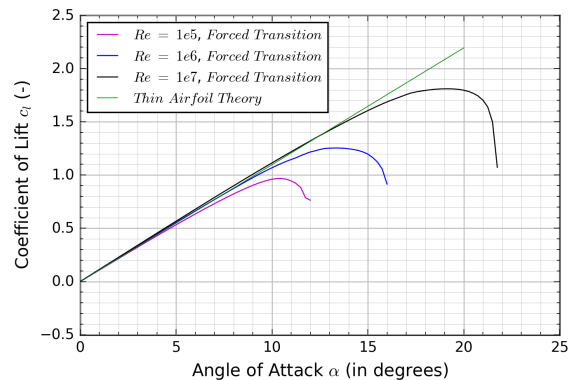


Figure 4.4: XFOIL Lift Polars, Forced Transition

For CFD simulations using turbulence models that are capable of predicting boundary layer transition, the Reynolds number should be at least 1,000,000, but preferably even higher. Due to the fact that the chosen $k-\omega$ SST turbulence model in foam-extend 3.2 cannot compute laminar to turbulent boundary layer transition, the boundary layer is assumed turbulent

throughout the airfoil. A fully turbulent boundary layer eliminates the nonlinear low Reynolds number effects, as can be seen in Figure 4.4 above. Here the boundary layer is tripped at the leading edge and any deviation from the thin airfoil theory is due to trailing edge separation. Assuming fully turbulent boundary layer significantly increases the error computed in drag, but not for lift. Fortunately, for airfoil flutter computations, the drag forces are of minor significance and the use of a fully turbulent boundary layer will not alter the results. A Reynolds number of 1,000,000 is chosen as the flow parameter for all steady and unsteady CFD simulations carried out in this Master Thesis. Its lift polar is of linear nature for a large enough range of angles of attack and the mesh size is sufficiently small.

4.4 Meshing Strategy

The ANSYS ICEM CFD meshing software is used for creating a computational mesh around the NACA 0009 airfoil. The coordinates taken from the Airfoil Tools Database (airfoiltools.com, 2018) are imported into the meshing software. The airfoil coordinates result in a NACA 0009 airfoil of unit length with a sharp trailing edge. Since blunt trailing edge allows for a better mesh quality and numerical convergence (Fehrs et al., 2014), the NACA 0009 airfoil geometry was altered to have a blunt trailing edge thickness $t/c = 0.00114$ at $x/c = 0.99572$. Such an alteration will not have an affect on the numerical accuracy. The mesh shown in Figures 4.5, 4.6 & 4.7, is the final mesh chosen after a mesh convergence study (see Section 4.4.1), upon which all the steady and unsteady CFD simulations are carried out.

The meshing technique that is used is similar to that of Fehrs et al. (2014). In the near vicinity of the airfoil a structured O-grid type mesh is utilized and enclosed with a structured C-grid that includes a structured wake region (see Figure 4.6 & 4.7). The remaining part of the flowfield is an unstructured all-quad domain (see Figure 4.5). The origin of the mesh is at the airfoils leading edge and the farfield has a radius of $100c$. A large farfield minimizes the influence of the farfield boundary conditions on the lift and drag results, which can be significant particularly for larger angles of attack (<http://www.nasa.gov>, 2018).

The unstructured mesh is denser in the wake region than in other areas in order to resolve the flow dynamics that have an influence on the airfoils aerodynamic forces. Its the finest near the airfoil and becomes courser further downstream of the airfoil. The structured region extends to $\approx 0.5c$ above and below the airfoil with a structured wake length of $\approx 1c$. In the vicinity of the airfoil, the wake is chosen to be structured for better convergence and accuracy in an area with significant gradients. It has been shown that larger structured wake regions do not improve the accuracy of the results (see Section 4.4.1).

The final mesh has a total of 101,184 cells. It is a 2D mesh with a unit length in the z direction. The number of divisions on the suction and pressure sides is 230. Near the leading and trailing edges the distribution of the divisions is finer than around the mid-chord. The number of divisions on the blunt trailing edge is 19. Furthermore, the structured wake region has a total of 119 divisions in the x direction. In the direction normal to the airfoils pressure and suction surfaces, the number of divisions are 117 with an expansion ratio of 1.1.

The mesh is used to simulate flows of a Reynolds number of 1,000,000. The low Re $k-\omega$ SST turbulence model used for the CFD simulations resolves the boundary layer to the viscous sub-layer and hence requires the y^+ in the first cell to be less than 1 for accurate results, although meshes with $y^+ < 3$ have given good results (Menter, 1993, 1994). The height of the first cell is made to be 0.00001m, which corresponds to a y^+ value of ≈ 0.425 . Table 4.1 summarizes the most important mesh topology parameters that ensure convergence and numerical accuracy.

Table 4.1: Mesh Topology Parameters

No. of Cells	Max. Non-Ortho	Average Non-Ortho	Max. Skewness	y^+
101,184	42.361	6.329	1.076	0.425

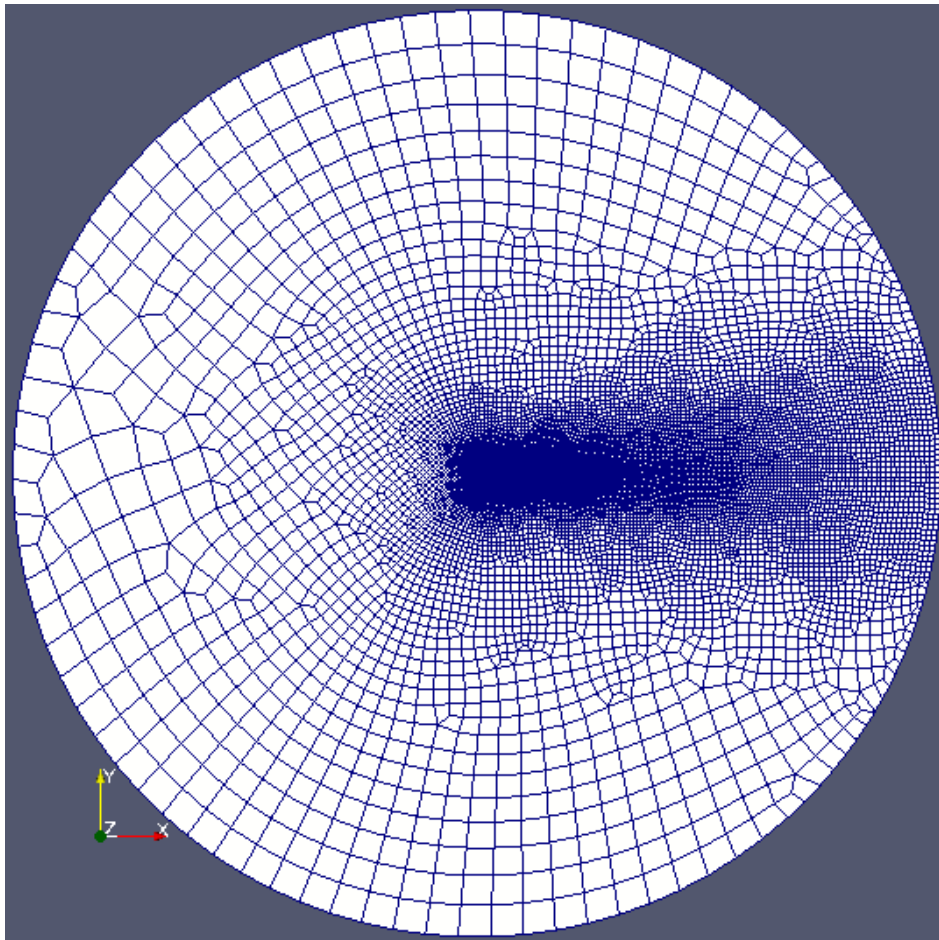


Figure 4.5: Farfield

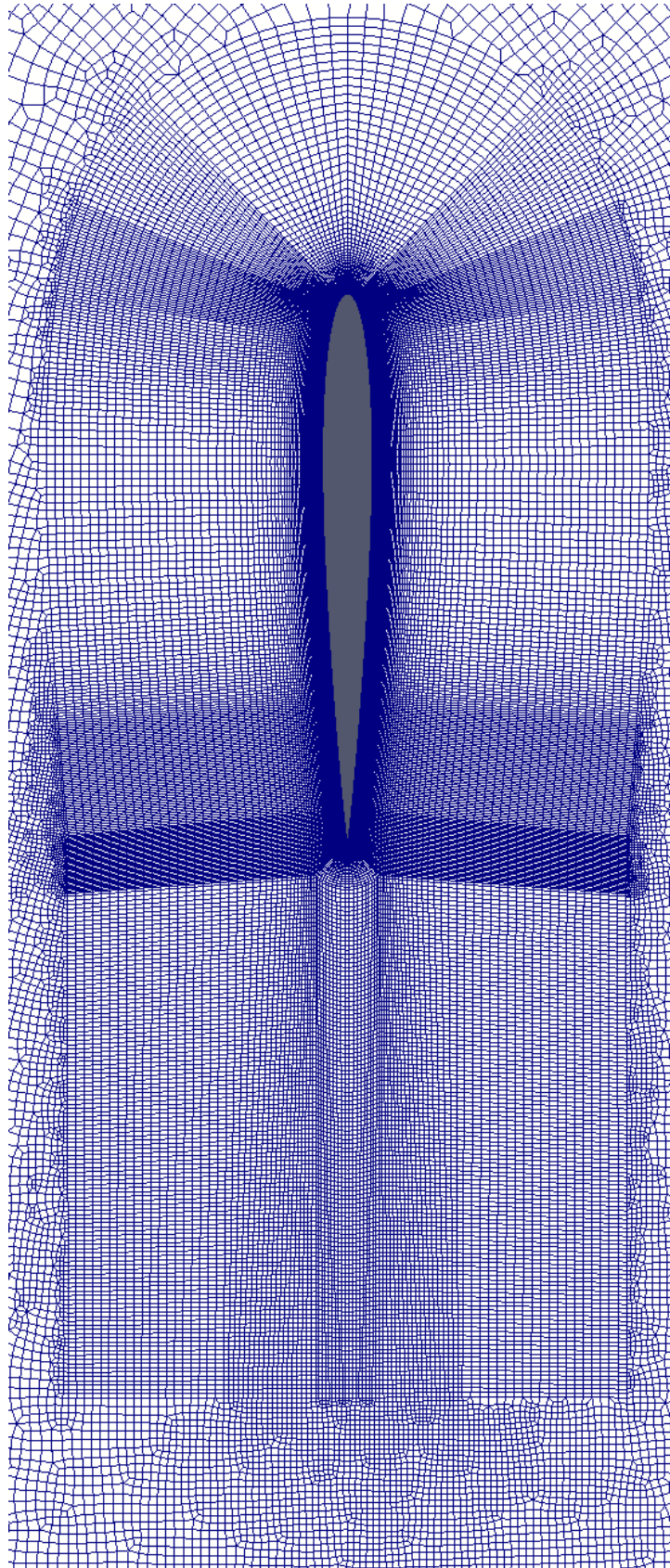


Figure 4.6: Structured C - Grid Around NACA 0009 Airfoil + Unstructured Farfield

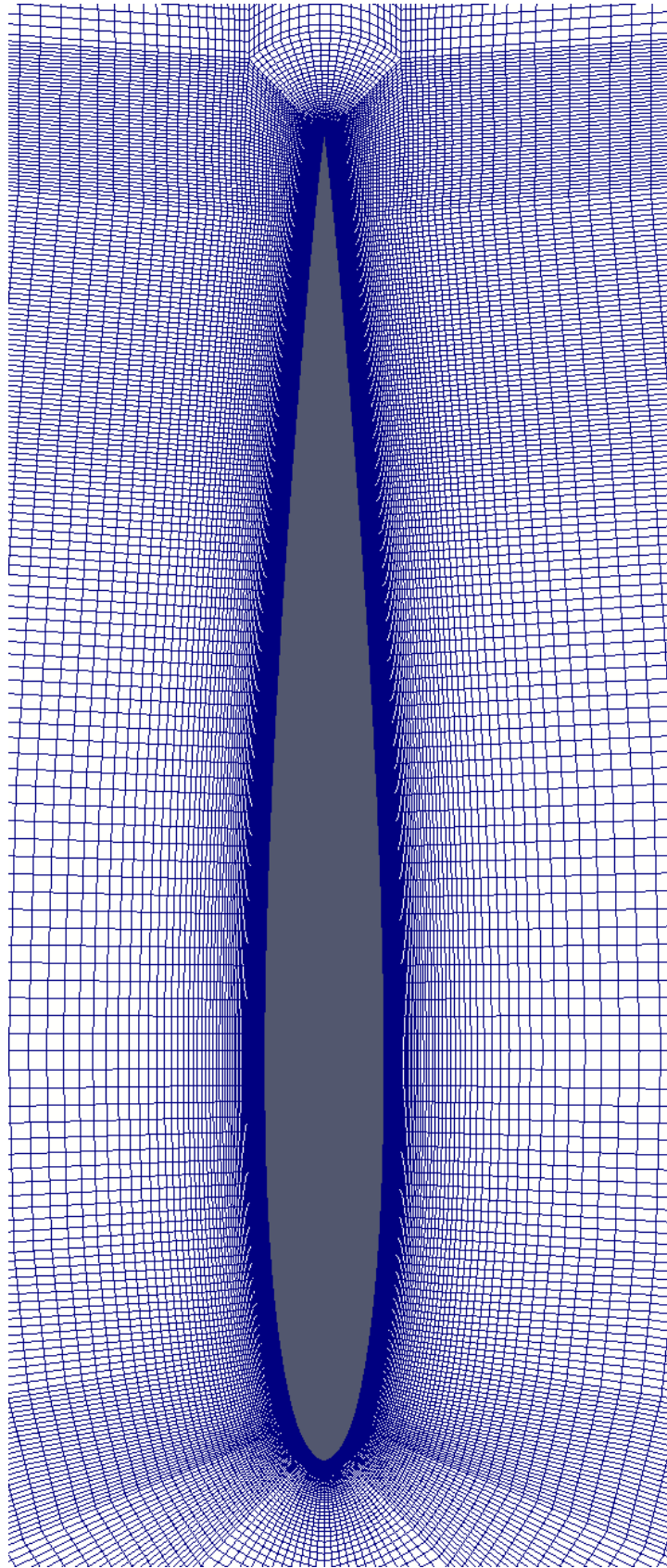


Figure 4.7: Structured O - Grid Around NACA 0009 Airfoil + Structured C - Grid Region

4.4.1 Mesh Convergence Tests

The mesh convergence tests were carried out by comparing the steady state lift and drag polars for four different meshes, whose topology parameters are given in Table 4.2. The boundary conditions and numerical schemes used are given in Section 4.5 & 4.6. Mesh 3 represents the mesh chosen for all further CFD computations and was shown in Figures 4.5, 4.6 & 4.7.

Table 4.2: Mesh Topology Parameters for Different Meshes

	Mesh 1	Mesh 2	Mesh 3	Mesh 4
No. of Cells	270,151	132,494	101,184	70,717
Max. Non-Ortho	42.322	42.361	42.361	42.361
Average Non-Ortho	5.293	5.715	6.329	7.093
Max Skewness	1.052	1.075	1.076	1.161
No. of Divisions Top / Bottom	230 / 230	230 / 230	230 / 230	150 / 150

All meshes have a y^+ of ≈ 0.425 and the number of divisions on the trailing edge are 19. Mesh 2 differs from Mesh 3 in that the number of divisions in the structured region in the direction normal to the airfoil is greater. Furthermore, Mesh 1 differs from Mesh 2 in that the wake length is now $\approx 5c$ rather than $\approx 1c$. Also, the farfield is much finer both upstream and downstream of the airfoil. Finally, Mesh 4 differs from Mesh 3 in that it has a smaller number of division on the top and bottom (i.e. suction and pressure) side of the airfoil. Its mesh is also coarser in the structured region in the direction normal to the airfoil.

From Figure 4.8 it is clear that the lift polars deviate for the coarsest mesh (i.e. Mesh 4). The same conclusion can be made for the drag polar (see Figure 4.9). Mesh 3 is the coarsest mesh that does not significantly deviate from the finest mesh (i.e. Mesh 1) lift and drag polars. As such, it is chosen as the mesh upon which all further CFD simulations are done.

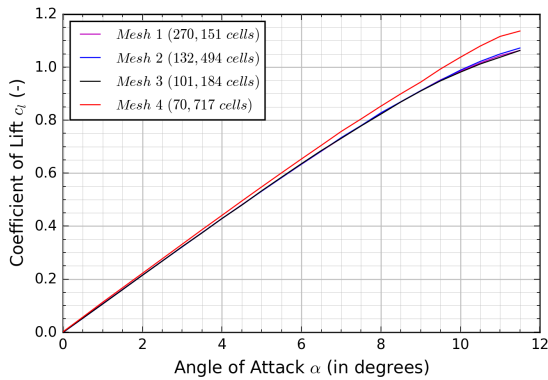


Figure 4.8: Lift Polars, $Re = 1,000,000$

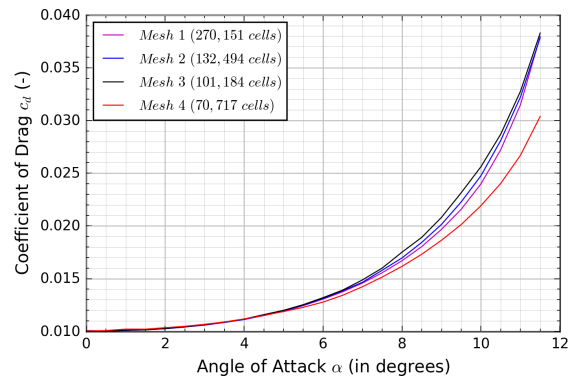


Figure 4.9: Drag Polars, $Re = 1,000,000$

4.5 Boundary Conditions

In this section, the choice of boundary conditions for the pressure p , velocity U , turbulent kinetic energy k , turbulent viscosity ν_t and the turbulent specific dissipation rate ω is explained. These will be used for steady & unsteady CFD simulations. The boundary conditions are prescribed on a total of four boundary patches. The boundary patch named "farfield" represents the boundary encompassing the whole computational domain. The boundary patch named "top" represents the suction side of the NACA 0009 airfoil, while the boundary patch named "bottom" represents the pressure side. Finally, the boundary patch named "te" represents the blunt trailing edge of the NACA 0009 airfoil.

4.5.1 Pressure & Velocity Boundary Conditions

At the inlet boundary, the velocity field is prescribed while the pressure is taken to be zero gradient (Hirsch, 2007). At the outlet, the boundary conditions are specified such that the overall mass balance for the computational domain is ensured (Jasak, 1996). This results in prescribing the pressure and having a zero gradient velocity boundary condition. In OpenFOAM, the boundary patch "farfield" will incorporate the inlet and outlet boundary conditions in the following way:

Pressure

For the pressure, the "farfield" boundary condition is specified as "outletInlet". This implies that if the computed flux is leaving the computational domain, a fixed value pressure boundary condition is prescribed. The fixed value of pressure is taken as 0. If the computed flux is entering the computational domain, a zero gradient boundary condition for pressure is prescribed.

Note that at the wall (i.e. at the "top", "bottom" & "te"), a zero-gradient boundary condition for pressure is prescribed.

Velocity

For the velocity, the "farfield" boundary condition is specified as "inletOutlet". This implies that if the computed flux is entering the computational domain, a fixed value velocity boundary condition is prescribed. A freestream velocity of 50 m/s is used. If the computed flux is leaving the computational domain, a zero gradient boundary condition for velocity is prescribed.

Note that at the wall (i.e. at the "top", "bottom" & "te"), the velocity of the fluid is equal to the velocity of the wall. For a fixed airfoil, a fixed value boundary condition of zero is prescribed for the velocity in the steady and unsteady simulations. However, for unsteady simulations *with a moving airfoil*, a `movingWallVelocity` boundary condition is used.

4.5.2 Turbulent Boundary Conditions

For the $k - \omega$ SST turbulence model, the turbulent kinetic energy, turbulent viscosity and specific rate of dissipation must be computed and appropriately assigned at the inlet, outlet and wall.

Turbulent Kinetic Energy

The turbulent kinetic energy is prescribed at the inlet and taken as zero-gradient at the outlet (Jasak, 1996). Hence, the same "inletOutlet" boundary condition for the "farfield" is used as described for the velocity. The turbulent kinetic energy is a function of the freestream turbulent intensity and the freestream velocity as follows

$$k_{inlet} = \frac{3}{2} \left[U \left(\frac{I}{100} \right) \right]^2, \quad (4.2)$$

where I (in %) is the turbulent intensity. Flow over an aircraft airfoil corresponds to a low turbulence case where the turbulence intensity is well below 1% (cfd online.com, 2018). A turbulence intensity of 0.1% is chosen. With a freestream velocity of 50 m/s, the turbulence kinetic energy k is $0.00375 \text{ m}^2/\text{s}^2$ at the inlet.

At the wall, the turbulent kinetic energy is zero (Menter, 1993, 1994). The low Re $k - \omega$ SST turbulence model resolves the boundary layer to the viscous sublayer where $y^+ < 5$. In this region, the turbulence is damped out and the boundary layer is dominated by viscous forces (White and Corfield, 2006), resulting in a turbulent kinetic energy of zero.

Specific Rate of Dissipation

Similar to the velocity and turbulent kinetic energy, the specific rate of dissipation is prescribed at the inlet and taken as zero gradient at the outlet (Jasak, 1996). The value of ω at the inlet is (Menter, 1993, 1994)

$$\omega_{inlet} = \frac{k_{inlet}}{\nu_t}, \quad (4.3)$$

where k is computed from Equation 4.2. The turbulent viscosity is chosen such that it is between one and ten times the value of the molecular kinematic viscosity. In this Master Thesis, the turbulent viscosity is chosen to be equal to the kinematic viscosity, i.e. $0.000049786 \text{ m}^2/\text{s}$. This results in a specific dissipation rate of 75.3224 s^{-1} .

At the wall, ω is computed from the following formula given in [Menter \(1993, 1994\)](#)

$$\omega_{wall} = 10 \frac{6\nu}{\beta_1(\Delta y)^2}, \quad (4.4)$$

where β_1 is a constant equal to 0.075 and Δy is the distance (in meters) to the first computational node away from the wall, i.e. half the height of the first computational cell. For the airfoil mesh used in this Master Thesis, the height of the first cell away from the wall (i.e. airfoil) is 0.00001m. This results in ω_{wall} to be 1593152000 s⁻¹.

Turbulent Viscosity

At the inlet and outlet, the turbulent viscosity is computed using the turbulent kinetic energy and the specific rate of dissipation. Therefore, for the boundary patch "farfield", the boundary condition of type "calculated" is used.

Similarly to the turbulent kinetic energy, the turbulent viscosity is zero at the wall ([Menter, 1993, 1994](#)).

4.6 Finite Volume Schemes & Solution Algorithm

The finite volume schemes used in the steady state CFD simulations are given in Table 4.3. For steady state cases, the `consistentSimpleFoam` algorithm is used.

Table 4.3: Finite Volume Schemes for Steady State Cases

General Discretization Term	Specific Discretization Term	Scheme
ddtSchemes	default	steadyState
gradSchemes	default	Gauss linear
divSchemes	default div(phi,U) div(phi,k) div(phi,omega) div((nuEff*dev(grad(U).T()))) div((nuEff*dev(T(grad(U))))))	none Gauss linearUpwind Gauss linear Gauss upwind Gauss upwind Gauss linear Gauss linear
laplacianSchemes	default	Gauss linear corrected
interpolationSchemes	default	linear
snGradSchemes	default	corrected

Table 4.4 below show the finite volumes schemes used for unsteady simulations. For the unsteady cases where mesh motion is included, the `consistentPimpleDyMFoam` solver is used. The RBF used for mesh deformation is IMQB.

Table 4.4: Finite Volume Schemes for Unsteady State Cases

General Discretization Term	Specific Discretization Term	Scheme
ddtSchemes	default ddt(k) ddt(omega)	bdf2 boundedBackward boundedBackward
gradSchemes	default	Gauss linear
divSchemes	default div(phi,U) div(phi,k) div(phi,omega) div((nuEff*dev(grad(U).T())))	none Gauss linearUpwind Gauss linear Gauss upwind Gauss upwind Gauss linear
laplacianSchemes	default	Gauss linear corrected
interpolationSchemes	default	linear
snGradSchemes	default	corrected

4.7 Concluding Remarks

In this chapter the reasoning behind choosing the NACA 0009 airfoil as well as a Reynolds number of 10^6 is thoroughly explained. The computational setup for all steady & unsteady CFD simulations that are to be carried out is presented. Specifically, the meshing strategy as well as the mesh used for all steady & unsteady CFD simulations is shown. The results of a mesh convergence study were also given. The boundary conditions for the pressure p , velocity U , turbulent kinetic energy k , specific dissipation rate ω and turbulent viscosity ν_t are explained. Finally, the numerical schemes and solvers used for the steady and unsteady CFD simulations are given.

Validation of OpenFOAM Unsteady Aerodynamic Modeling

5.1 Introduction

In this chapter, the OpenFOAM unsteady lift and moment for an oscillating NACA 0009 airfoil at reduced frequencies 0.1, 0.2, 0.3, 0.4, 0.6, 0.8 & 1 are compared with the results obtained by Theodorsen Theory, a benchmark result that has been validated experimentally (Halfman, 1952). The NACA 0009 airfoil undergoes imposed oscillatory pitching motion about its midchord and is subject to a steady flow velocity of 50 m/s (i.e. $Re = 10^6$). The airfoil oscillates $\pm 1^\circ$ about the steady state angle of attack in the following way

$$\theta(t) = \alpha_{ss} - \bar{\theta} \sin(2\pi ft), \quad (5.1)$$

where $\bar{\theta}$ is the oscillation amplitude of 1° , α_{ss} is the steady state angle of attack of 1° and f is the oscillation frequency in Hertz. The mesh deformation technique used to deform the mesh each time step is the RBF IMQB (De Boer et al., 2007a). Only pitching motion is considered for validation, rather than pitching & plunging, because it constitutes the majority of the unsteady lift and moment.

5.2 Comparison of Unsteady Lift for Different Reduced Frequencies with Theodorsen Theory

In this section, only the OpenFOAM unsteady lift computations are compared with Theodorsen theory. The Theodorsen lift expression for a pitching airfoil is derived and the

formulae for computing the normalized amplitude and phase angle with Theodorsen theory and OpenFoam are shown. Finally, the results are compared with each other.

5.2.1 Theodorsen Lift for a Harmonically Pitching Airfoil

For a purely pitching airfoil about its midchord, $h = \dot{h} = \ddot{h} = 0$. Furthermore, $a = 0$ (the elastic axis is at the airfoil midchord). Taking this into consideration, the Theodorsen lift expression given by Equation 2.3 reduces to the following

$$c_l = \frac{\pi b}{U^2} \left[U \dot{\theta} \right] + \frac{c_{l,\alpha} C(k)}{U} \left[U \theta + \frac{b}{2} \dot{\theta} \right], \quad (5.2)$$

where the first term is the non-circulatory part (i.e. the apparent mass) and the second and third terms are the circulatory part of the lift equation. The lag effect of the circulatory part due to the wake is introduced via Theodorsen's Function $C(k)$. In order to obtain the final expression of lift for harmonic motion, the following relations representing oscillatory pitching motion must be substituted into Equation 5.2.

$$\theta = \bar{\theta} e^{i\omega t}; \quad \dot{\theta} = i\omega \bar{\theta} e^{i\omega t}; \quad \ddot{\theta} = -\omega^2 \bar{\theta} e^{i\omega t}. \quad (5.3)$$

These relations describe a purely harmonically oscillating airfoil in pitch, where ω is the oscillation frequency (in radians) and $\bar{\theta}$ is the oscillation amplitude (i.e. 1°) about the steady state angle of attack α_{ss} . The real part of θ , $\dot{\theta}$ and $\ddot{\theta}$ describe the actual pitching displacement, velocity and acceleration, respectively. The expression for $\ddot{\theta}$ is not used here since it is not present in Equation 5.2, but will be needed for the Theodorsen moment expression given in the next section. The steady state lift value is also added to Equation 5.2 such that the final expression for the Theodorsen lift is

$$c_l = c_{l,ss} + \left[\left\{ i\pi k + c_{l,\alpha} C(k) + \frac{c_{l,\alpha} C(k)}{2} ik \right\} \bar{\theta} \right] e^{i\omega t}, \quad (5.4)$$

where the reduced frequency k is $\omega b/U$. Furthermore, the $c_{l,ss}$ corresponds to the steady state lift of the angle of attack about which the airfoil is oscillating (i.e. 1°). The actual Theodorsen lift is computed with the real part Equation 5.4 which is then used for evaluating the OpenFOAM results. Thin Airfoil Theory (Katz and Plotkin, 2001) suggests that the value of 2π is used for $c_{l,\alpha}$ and hence the steady state lift value $c_{l,ss}$ will be $2\pi\alpha$. These values will be slightly different than those obtained via CFD. In order to eliminate the differences caused by the use of different constants, those obtained by CFD are used for the Theodorsen model as well. Hence, the steady state value $c_{l,ss}$ is 0.108 at 1° and $c_{l,\alpha}$ is 1.9697π .

Theodorsen Normalized Amplitude (for Unsteady Lift)

The expression for lift given by Equation 5.4 gives a specific hysteresis loop for a given value of the reduced frequency k . As $k \rightarrow 0$, the hysteresis loop collapses to a linear curve that is identical to the steady state polar. This means that the oscillation frequency is so small that the unsteady lift expression actually correspond to those computed by the steady state. The normalized amplitude (Leishman, 2006) shown below is the ratio of the maximum lift of the purely oscillating part (the term in the square brackets in Equation 5.4) and the maximum lift as $k \rightarrow 0$ (i.e. the steady state lift obtained by Thin Airfoil Theory)

$$\sigma_{c_{l,theo}} = \frac{|c_l - c_{l,ss}|}{c_{l,\alpha}|\bar{\theta}|}, \quad (5.5)$$

where the $c_{l,\alpha}$ is taken from CFD computations. Substituting Equation 5.4 into Equation 5.5, the final expression for computing the normalized amplitude becomes

$$\sigma_{c_{l,theo}} = \frac{1}{c_{l,\alpha}} \left| i\pi k + c_{l,\alpha}C(k) + \frac{c_{l,\alpha}C(k)}{2}ik \right|. \quad (5.6)$$

Theodorsen Phase Angle (for Unsteady Lift)

The phase angle gives information on how much the maximum unsteady lift leads or lags the maximum steady state lift, where the steady state lift is in phase with the angle of attack. Hence, if the phase angle is positive, the unsteady lift will lead the steady state lift. If the phase angle is negative, the unsteady lift will lag the steady state lift. The phase angle is defined by the term in the square brackets of Equation 5.4, which is generally a complex number for a certain value of k . However, for example for $k \rightarrow 0$, the complex number becomes real and there will be no phase lag. Therefore, the unsteady lift will be in phase with the angle of attack (i.e. it will be identical to the steady state lift for a given angle of attack). The phase angle is computed by the following formula

$$\phi_{c_{l,theo}} = \tan^{-1} \left[\frac{\text{imag} \left[\left\{ i\pi k + c_{l,\alpha}C(k) + \frac{c_{l,\alpha}C(k)}{2}ik \right\} \bar{\theta} \right]}{\text{real} \left[\left\{ i\pi k + c_{l,\alpha}C(k) + \frac{c_{l,\alpha}C(k)}{2}ik \right\} \bar{\theta} \right]} \right]. \quad (5.7)$$

OpenFOAM Normalized Amplitude (for Unsteady Lift)

The OpenFOAM normalized amplitude is computed in the exact same manner as for the Theodorsen normalized amplitude. The only difference is that the c_l in Equation 5.5 is taken from the unsteady CFD simulations.

OpenFOAM Phase Angle (for Unsteady Lift)

The OpenFOAM phase angle is computed in a different manner than for Theodorsen, since an analytical expression like for the unsteady Theodorsen lift (see Equation 5.7) does not exist. The CFD simulations give a discrete set of c_l values, each corresponding to a specific time t_n . Furthermore, the angle of attack at t_n can be calculated because the imposed (sinusoidal) motion is known. Both $\theta(t)$ and $c_l(t)$ will reach their maximum (or minimum) value at a certain time. The phase angle will characterize the difference in time for reaching this maximum value. Taking this into account, the formula used to calculate the phase angle for the results obtained via OpenFOAM is

$$\phi_{c_l, OpenFOAM} = \frac{t_{\theta, max} - t_{c_l, max}}{T} \cdot 360^\circ, \quad (5.8)$$

where T is the period. The formula also takes into account the sign of the phase angle. So, if c_l reaches its maximum value after θ , the phase angle is negative. If c_l reaches its maximum value before θ , the phase angle is positive. Of course, the phase angle is zero if c_l and θ reach their maximum at the same time and c_l is in phase with the steady state lift.

5.2.2 Convergence Criterion for Unsteady OpenFOAM Simulations

The unsteady CFD simulations are carried out for a certain number of periods that are needed for the unsteady lift to become truly periodic. The number of periods required depends on the reduced frequency, but usually at least 2 are needed. Figure 5.1 shows the unsteady c_l and θ change in time for a reduced frequency of 0.8. However, it is hard to see from this figure whether the unsteady lift is truly harmonic. The c_l vs. θ (see Figure 5.2) is a better representation for deciding whether the unsteady lift converged to its periodic solution. Therefore, as the CFD simulations are being done, this plot is repeatedly constructed until it becomes clear that the results have converged to a periodic solution.

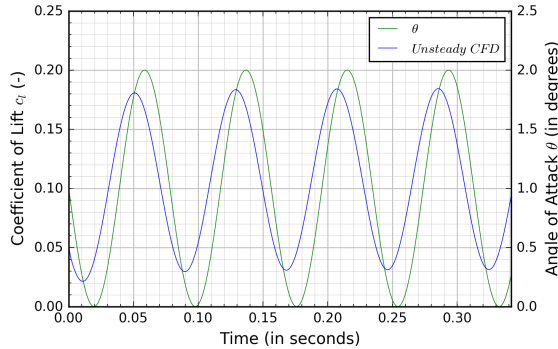


Figure 5.1: c_l vs. time, $k = 0.8$

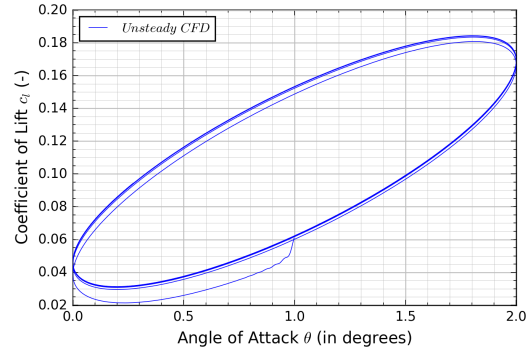


Figure 5.2: c_l vs. θ , $k = 0.8$

5.2.3 Unsteady Lift Results

The Figures 5.3 to 5.8 below show the OpenFOAM/Theodorsen c_l vs. $time$ and c_l vs. θ plots for reduced frequencies 0.2, 0.6 & 1. For the Theodorsen c_l vs. $time$ plots, the real part of the Theodorsen lift (see Equation 5.4) is plotted with respect to time. For the Theodorsen c_l vs. θ plots, the real part of the Theodorsen lift is plotted with respect to the real part of harmonic angle of attack θ (the first expression in Equation 5.3). It is clear that the results compare well. Such good agreement is also seen in the plots for reduced frequencies of 0.1, 0.3, 0.4 & 0.8 (see Appendix B).

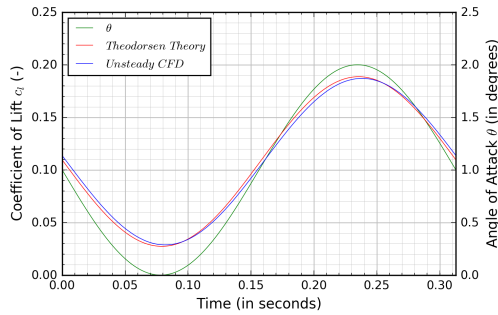


Figure 5.3: c_l vs. $time$, $k = 0.2$

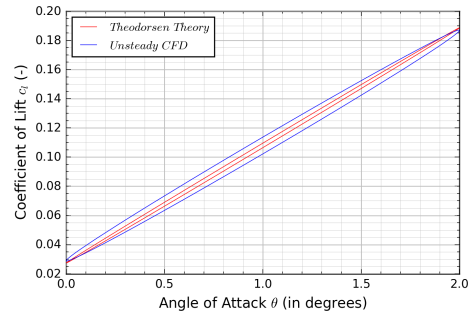


Figure 5.4: c_l vs. θ , $k = 0.2$

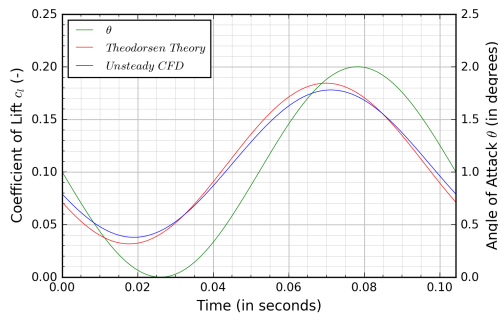


Figure 5.5: c_l vs. $time$, $k = 0.6$

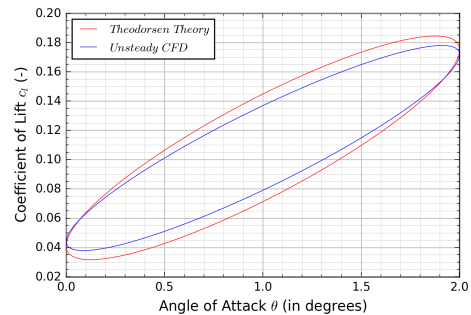


Figure 5.6: c_l vs. θ , $k = 0.6$

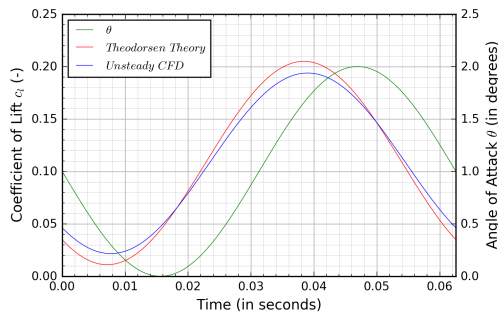


Figure 5.7: c_l vs. $time$, $k = 1$

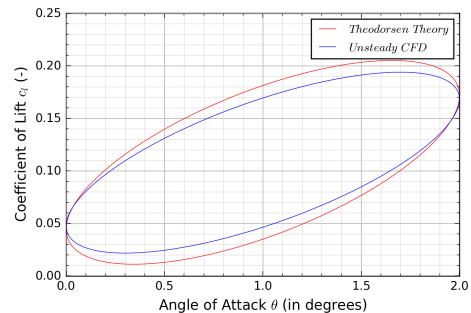


Figure 5.8: c_l vs. θ , $k = 1$

Comparing the normalized amplitudes and phase angle will give further indication on how well the OpenFOAM results compare with Theodorsen. Figures 5.9 and 5.10 below depict

the normalized amplitude and phase angle of the lift obtained by unsteady CFD simulations and Theodorsen Theory. The results for all reduced frequencies are shown in these plots. The normalized lift amplitude shows the ratio of the maximum unsteady lift amplitude and the maximum steady state lift amplitude. The difference in OpenFOAM and Theodorsen Theory grows for an increasing reduced frequency. However, for reduced frequencies smaller than 0.4, the difference is only 5%. The maximum deviation is at $k = 1$ and is $\approx 11\%$. The phase angle describes the phase shift between the unsteady lift and the steady state angle of attack (i.e. the steady state lift). The difference in the computed phase angle of OpenFOAM and Theodorsen Theory seems to be independent of the reduced frequencies and is only a few degrees. If the difference in the phase angle between OpenFOAM and Theodorsen for the worst case scenario would be considered 180° , meaning that the two results are completely out of phase, a few degrees difference seems to indicate a perfect correlation.

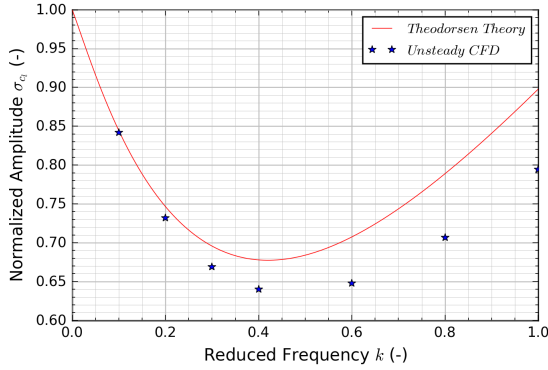


Figure 5.9: σ_{c_l} vs. k (for unsteady lift)

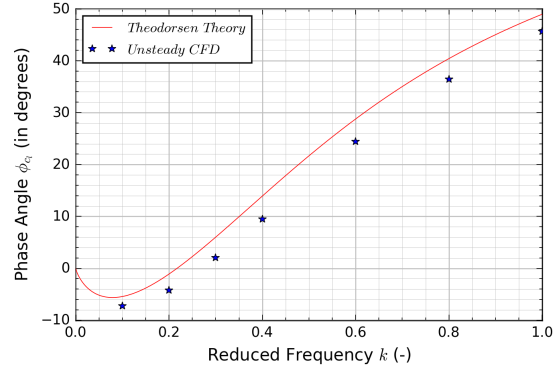


Figure 5.10: ϕ_{c_l} vs. k (for unsteady lift)

5.3 Comparison of Unsteady Moment for Different Reduced Frequencies with Theodorsen Theory

In this section, only the OpenFOAM unsteady moment computations are compared with Theodorsen Theory. The Theodorsen moment expression for a pitching airfoil is derived and the formulae for computing the normalized amplitude and phase angle with Theodorsen Theory and OpenFOAM is shown. Finally, the results are compared with each other. Note that the convergence criterion used to determine whether the unsteady moment has reached its periodic solution is identical to that explained for the lift (see Section 5.2.2).

5.3.1 Theodorsen Moment for a Harmonically Pitching Airfoil

In this section the Theodorsen moment about the airfoil midchord for a harmonically pitching airfoil is derived. The assumptions made in the Theodorsen lift derivations at the beginning of Section 5.2.1 still hold here as well. Therefore, the Theodorsen moment expression given

by Equation 2.4 reduces to

$$c_m = \frac{\pi}{2U^2} \left[-\frac{Ub}{2}\dot{\theta} - \frac{b^2}{8}\ddot{\theta} \right] + \frac{c_{l,\alpha}C(k)}{4U} \left[U\theta + \frac{b}{2}\dot{\theta} \right], \quad (5.9)$$

where the first two terms represent the non-circulatory part and the last two the circulatory part. In order to obtain the Theodorsen moment for harmonic airfoil motion, the expressions given by Equation 5.3 are substituted in Equation 5.9. Furthermore, as in the case for the Theodorsen lift, a steady state moment is added corresponding to the angle of attack about which the airfoil is oscillating (i.e. 1°). The final moment expression is as follows

$$c_m = c_{m,ss} + \left[\left\{ -\frac{i\pi k}{4} + \frac{\pi k^2}{16} + \frac{c_{l,\alpha}C(k)}{4} + \frac{ik}{8}c_{l,\alpha}C(k) \right\} \bar{\theta} \right] e^{i\omega t}, \quad (5.10)$$

where the steady state moment is about the airfoil midchord. Thin Airfoil Theory computes this value as $c_{m,AC} + c_{l,ss}/4$ (i.e. $0.25c_{l,\alpha}\alpha$, because $c_{m,AC}=0$). Typically 2π is used for the value of $c_{l,\alpha}$. However, the $c_{l,\alpha}$ computed by OpenFOAM is slightly different. In addition, $c_{m,AC}$ is a small non-zero value for an angle of attack of 1° . As was done for the steady state lift $c_{l,ss}$ (see the end of Section 5.2.1), the OpenFOAM value of 0.00046 for $c_{m,AC}$ is used and 1.9697π for $c_{l,\alpha}$. Hence $c_{m,ss} = 0.02746$. Even though these are differences in value of a few percent, it will eliminate errors arising due to the use of different constants.

Theodorsen Normalized Amplitude (for Unsteady Moment)

The normalized amplitude for the moment is computed in a similar manner as for the lift

$$\sigma_{c_m,theo} = \frac{|c_m - c_{m,ss}|}{0.25c_{l,\alpha}|\bar{\theta}|}, \quad (5.11)$$

where the denominator represents the maximum moment about the airfoil midchord for $k \rightarrow 0$. Note that the denominator term stems from Thin Airfoil Theory. Substituting Equation 5.10 into Equation 5.11, the final expression of the normalized amplitude for the Theodorsen moment becomes

$$\sigma_{c_m,theo} = \frac{1}{c_{l,\alpha}} \left| -i\pi k + \frac{\pi k^2}{4} + c_{l,\alpha}C(k) + \frac{ik}{2}c_{l,\alpha}C(k) \right|. \quad (5.12)$$

Theodorsen Phase Angle (for Unsteady Moment)

The Theodorsen moment phase angle is computed in exactly the same manner as for the Theodorsen lift phase angle given by Equation 5.7. The only difference will be the argument of the equation

$$\phi_{c_m, theo} = \tan^{-1} \left[\frac{\text{imag} \left[\left\{ -\frac{i\pi k}{4} + \frac{\pi k^2}{16} + \frac{c_{l,\alpha} C(k)}{4} + \frac{ik}{8} c_{l,\alpha} C(k) \right\} \bar{\theta} \right]}{\text{real} \left[\left\{ -\frac{i\pi k}{4} + \frac{\pi k^2}{16} + \frac{c_{l,\alpha} C(k)}{4} + \frac{ik}{8} c_{l,\alpha} C(k) \right\} \bar{\theta} \right]} \right]. \quad (5.13)$$

As was the case for the Theodorsen lift phase angle, a negative phase angle means the moment is lagging the steady state solution while a positive angle means the moment is leading the steady state solution.

OpenFOAM Normalized Amplitude (for Unsteady Moment)

The normalized amplitude computed using the OpenFOAM results is done using Equation 5.11. However, now the values for c_m come from the unsteady CFD simulations.

OpenFOAM Phase Angle (for Unsteady Moment)

The phase angle for OpenFOAM moment is computed using the following formula (similar to Equation 5.8)

$$\phi_{c_m, OpenFOAM} = \frac{t_{\theta, max} - t_{c_m, max}}{T} \cdot 360^\circ. \quad (5.14)$$

5.3.2 Unsteady Moment Results

The Figures 5.11 to 5.16 below show the OpenFOAM/Theodorsen c_m vs. *time* and c_m vs. θ plots for reduced frequencies 0.2, 0.6 & 1. For the Theodorsen c_m vs. *time* plots, the real part of the Theodorsen moment (see Equation 5.10) is plotted with respect to time. For the Theodorsen c_m vs. θ plots, the real part of the Theodorsen moment is plotted with respect to the real part of harmonic angle of attack θ (the first expression in Equation 5.3). It is clear that the results compare well. Such good agreement is also seen in the plots for reduced frequencies of 0.1, 0.3, 0.4 & 0.8 (see Appendix C).

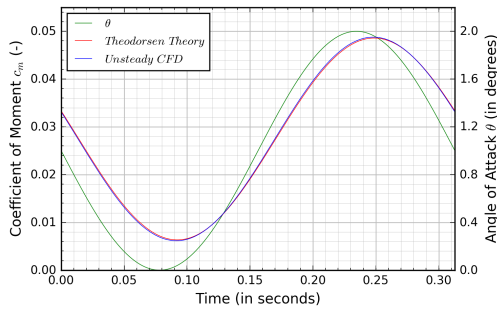


Figure 5.11: c_m vs. *time*, $k = 0.2$

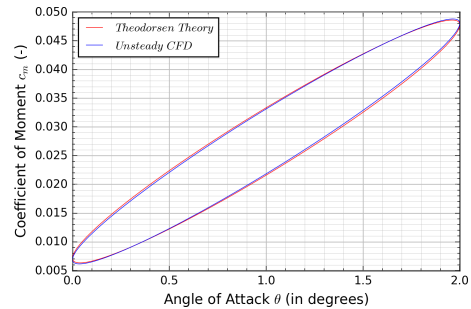


Figure 5.12: c_m vs. θ , $k = 0.2$

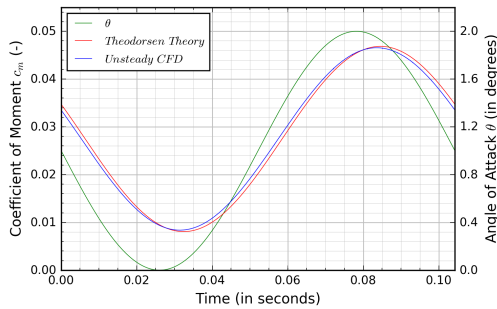


Figure 5.13: c_m vs. *time*, $k = 0.6$

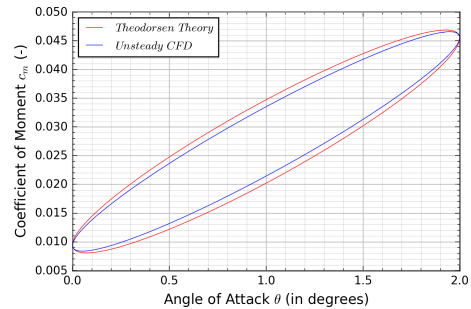


Figure 5.14: c_m vs. θ , $k = 0.6$

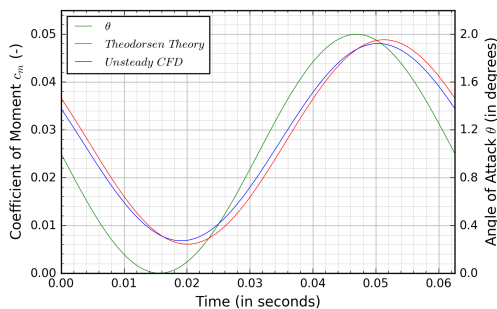


Figure 5.15: c_m vs. *time*, $k = 1$

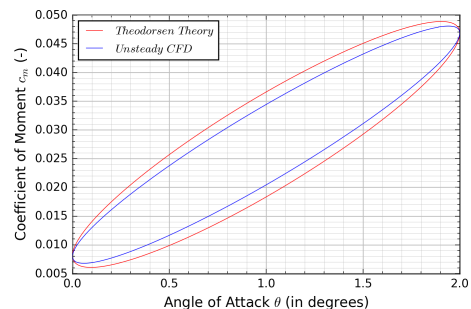


Figure 5.16: c_m vs. θ , $k = 1$

Comparing the normalized amplitudes and phase angle will give further indication on how well the OpenFOAM results compare with Theodorsen. Figures 5.17 and 5.18 below depict the normalized amplitude and phase angle of the unsteady moment obtained by OpenFOAM

and Theodorsen Theory. The results for all reduced frequencies are shown in these plots. For the normalized moment amplitude, the maximum deviation between OpenFOAM and Theodorsen is $\approx 4\%$. These results match even better than those obtained for the normalized lift amplitude. For the phase angle, the difference between OpenFOAM and Theodorsen for smaller reduced frequencies is a few degrees, but tends to grow as the reduced frequency increases. The maximum deviation is $\approx 7^\circ$ for a reduced frequency of 0.8. Again, if a phase difference of 180° between OpenFOAM and Theodorsen is considered the worst case scenario, the matching in these results can be considered good. When compared with the OpenFOAM and Theodorsen correlation for the lift phase angle, it seems that this correlation is slightly better for lower reduced frequencies and slightly worse for higher reduced frequencies.

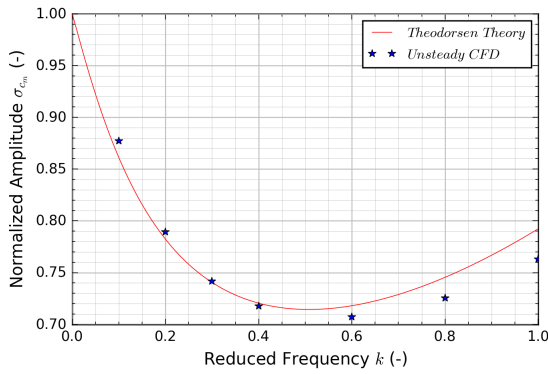


Figure 5.17: σ_{c_m} vs. k (for unsteady moment)

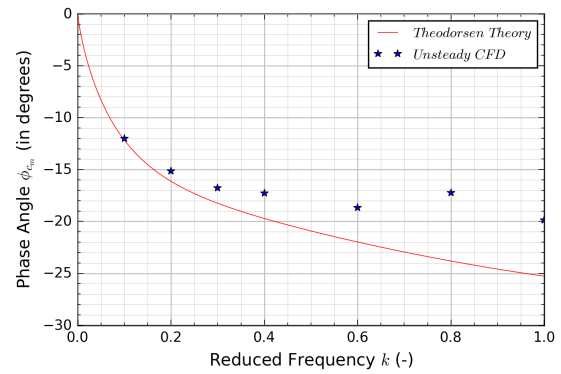


Figure 5.18: ϕ_{c_m} vs. k (for unsteady moment)

5.4 Concluding Remarks

The aim of this chapter was to validate OpenFOAM's capability in predicting the unsteady lift and moment for different reduced frequencies. This was done for a harmonically pitching (1 DOF) NACA 0009 airfoil about its midchord and the steady state angle of $\alpha_{ss}=1^\circ$. The oscillation amplitude was $\bar{\theta}=1^\circ$ and the airfoil was subject to a constant inflow velocity of 50 m/s (i.e. $Re = 10^6$). The results were compared with the benchmark Theodorsen Theory.

The results, for the most part, are excellent. Only the normalized lift amplitude has a slightly higher deviance from Theodorsen Theory for reduced frequencies close to 1 than is the case for lower reduced frequencies. The same trend is apparent in the phase angle of the unsteady moment. Even though Theodorsen Theory is a benchmark result that has been validated experimentally, it is still a low fidelity model and the results obtained by the high fidelity simulations carry significance. Therefore, it might be possible that the OpenFOAM simulations provide more accurate results than Theodorsen Theory for higher reduced frequencies. The results of both models will serve as reference data when validating the unsteady lift and moment computed by the linearized aerodynamic models shown in the next chapter.

The effort was made to conduct such an analysis because, in an aeroelastic system, it is of major importance to predict the unsteady air loads in order to accurately calculate aeroelastic phenomena such as flutter (Weisshaar, 2017). Small changes in phase shift, for example, could be the difference in whether the structure dissipates or extracts energy into the airstream (Bisplinghoff et al., 2013). A good agreement between Theodorsen Theory and OpenFOAM allows OpenFOAM to be used in a transient FSI simulation for flutter computation and even gust analysis.

In addition, validating that OpenFOAM can accurately predict unsteady forces due to perturbed motion will imply that it can be used to build the linearized aerodynamic lift and moment models shown in the next chapter. Had the agreement of the results been unsatisfactory, there would be no justification for using unsteady OpenFOAM simulations in building these linearized aerodynamic lift and moment models.

Chapter 6

Validation of Linearized Aerodynamic CFD Modeling

6.1 Introduction

In this chapter the aerodynamic forces of a 1 DOF pitching airfoil about its midchord, subject to an inflow velocity of 50 m/s (i.e. $Re = 10^6$), are linearized about the steady state angle of attack $\alpha_{ss}=1^\circ$. The linearized coefficients are constant and are computed using the results of unsteady CFD simulations. Note that these parameters are identical to those chosen in the previous chapter, where the nonlinear unsteady CFD results were compared to Theodorsen Theory. The constructed linearized CFD model should be able to predict the unsteady lift and moment for any type of perturbation $\theta'(t)$ about the steady state angle of attack α_{ss} , as long as the perturbations are small enough, such that the flow linearity is preserved. Therefore, the unsteady lift and moment response obtained by the linearized model for a sinusoidally pitching airfoil about the steady state angle of attack $\alpha_{ss} = 1^\circ$ and an oscillation amplitude of $\pm 1^\circ$ is compared with the nonlinear CFD results and Theodorsen Theory. In such a way, the linearized aerodynamic model can be validated, at least for oscillatory motion. Good agreement with nonlinear CFD results and Theodorsen Theory implies that the linearized aerodynamic CFD model could be used to accurately compute the flutter boundary. The linearization method can be applied to the aerodynamic forces that act on a n degree of freedom system, such as a 3D wing, for example. These linearized forces will compose the RHS of the EOM (see Section 2.4).

6.2 The Linearization Technique

For an airfoil restricted to pure pitching motion, the unsteady lift c_l and moment c_m is a function of the angle of attack θ , the angular velocity $\dot{\theta}$ and the angular acceleration $\ddot{\theta}$. In

this case, the linearization process is done in terms of the degrees of freedom rather than in modal coordinates, because there is only one degree of freedom and there is no advantage to tackle the problem in terms of modal analysis. Therefore, the linear equations for the unsteady lift and moment about the steady state can be written as the following

$$c_l(\theta, \dot{\theta}, \ddot{\theta}) \approx c_{l,ss} + \left. \frac{\partial c_l}{\partial \theta} \right|_s \theta' + \left. \frac{\partial c_l}{\partial \dot{\theta}} \right|_s \dot{\theta}' + \left. \frac{\partial c_l}{\partial \ddot{\theta}} \right|_s \ddot{\theta}', \quad (6.1)$$

$$c_m(\theta, \dot{\theta}, \ddot{\theta}) \approx c_{m,ss} + \left. \frac{\partial c_m}{\partial \theta} \right|_s \theta' + \left. \frac{\partial c_m}{\partial \dot{\theta}} \right|_s \dot{\theta}' + \left. \frac{\partial c_m}{\partial \ddot{\theta}} \right|_s \ddot{\theta}', \quad (6.2)$$

where θ' , $\dot{\theta}'$ and $\ddot{\theta}'$ are the perturbation pitch displacement, velocity and acceleration, respectively from the steady state. These variables are purely a function of time. The partial derivatives in Equations 6.1 & 6.2 represent the linearized lift and moment coefficients, respectively. Once they are found, the linearized model is complete. An accurate unsteady lift and moment response should be able to be obtained for any $\theta'(t)$ about the steady state angle of attack α_{ss} , as long as the perturbations are small enough such that the flow remains of linear nature.

6.2.1 Coefficient Extraction Method

In order to find the coefficients, the airfoil is perturbed with a function $\theta'(t)$, and hence $\dot{\theta}'(t)$ & $\ddot{\theta}'(t)$, for a finite number of time steps. The state from which the perturbations take place is the computed steady state solution at $\alpha_{ss} = 1^\circ$. At each time t , the unsteady lift and moment that compose the LHS of Equations 6.1 & 6.2 are computed with unsteady CFD simulations and the perturbation displacement, velocity and acceleration on the RHS can be calculated, leaving the coefficients as the unknowns. The number of equations for the lift and moment is equal to the number of time steps taken. Note that at least three time steps are needed, because there are three unknown coefficients in both the linearized unsteady lift and moment models. In this Master Thesis, 20 time steps were chosen. As was stated in Section 2.4, in principle, any $\theta'(t)$ can be chosen as long as $\dot{\theta}'(t)$ & $\ddot{\theta}'(t)$ are non zero and the perturbed displacement, velocity and acceleration are not linearly dependent on each other. In this Master Thesis, the perturbation functions $\theta'(t)$, $\dot{\theta}'(t)$ and $\ddot{\theta}'(t)$ are

$$\theta' = \bar{\theta}t^3; \quad \dot{\theta}' = 3\bar{\theta}t^2; \quad \ddot{\theta}' = 6\bar{\theta}t, \quad (6.3)$$

where $\bar{\theta}$ is the perturbation rate. Perturbing the airfoil for 20 time steps will give 20 lift equations of the form of Equation 6.1 and 20 moment equations of the form of Equation 6.2, with three unknown coefficients for the linearized lift model and for the linearized moment

model. The system of equation for the linearized lift are written in the form of $\{\mathbf{f}\} = [\mathbf{A}]\{\mathbf{b}\}$ as is shown below

$$\begin{Bmatrix} \Delta c_{l,t_4} \\ \Delta c_{l,t_5} \\ \vdots \\ \Delta c_{l,t_{20}} \end{Bmatrix} = \begin{bmatrix} \bar{\theta}t_4^3 & 3\bar{\theta}t_4^2 & 6\bar{\theta}t_4 \\ \bar{\theta}t_5^3 & 3\bar{\theta}t_5^2 & 6\bar{\theta}t_5 \\ \vdots & \vdots & \vdots \\ \bar{\theta}t_{20}^3 & 3\bar{\theta}t_{20}^2 & 6\bar{\theta}t_{20} \end{bmatrix} \begin{Bmatrix} \left. \frac{\partial c_l}{\partial \theta} \right|_s \\ \left. \frac{\partial c_l}{\partial \theta} \right|_s \\ \left. \frac{\partial c_l}{\partial \theta} \right|_s \end{Bmatrix}, \quad (6.4)$$

where $\Delta c_{l,t_4} = c_l(t_4) - c_{l,ss}(t_4)$, $\Delta c_{l,t_5} = c_l(t_5) - c_{l,ss}(t_5)$, ..., $\Delta c_{l,t_{20}} = c_l(t_{20}) - c_{l,ss}(t_{20})$. Note that the first 3 time steps are omitted, because the CFD solver cannot accurately calculate the airfoil boundary velocity and acceleration terms (see Appendix D for a more detailed clarification). Δc_l represents the change in lift due to the perturbed motion relative to the *steady* state. The *steady* state lift is calculated at each specific time t for a unperturbed airfoil using the `consistentPimpleFoam` solver because, if the steady state lift solution of the `consistentSimpleFoam` solver is used, the computed Δc_l will be inaccurate, as is explained later in the paragraph. This is of particular importance if the perturbed motion is small. The reasoning behind this is the following: the initial steady state solution from which the airfoil is perturbed is obtained by the solver `consistentSimpleFoam` and the convergence criterion for the pressure, momentum, k and ω equations is 10^{-5} . This convergence criterion is low enough to provide accurate lift results; however, if a transient simulation using `consistentPimpleFoam` for the fixed airfoil is carried out using the steady state solution as an initial condition, the lift value will change slightly after each time step. The difference in lift will increase the longer the transient simulation runs but will reach a finite value after a certain amount of time. If significant, this change in lift could have a large influence on the computed linearized coefficients and is explained on the following page. Decreasing the convergence criterion would certainly give a better estimate of the steady state lift and hence decrease these changes in lift (but a true steady state may never be attainable because the flow is not 100% steady); however, it was seen that it caused convergence issues. So, when the airfoil is perturbed its change in lift will consist of a change in total lift due to the perturbation and a *significant* change in total lift due to the fact that the initial conditions was not the *converged enough* steady state solution (due to a too high convergence criterion).

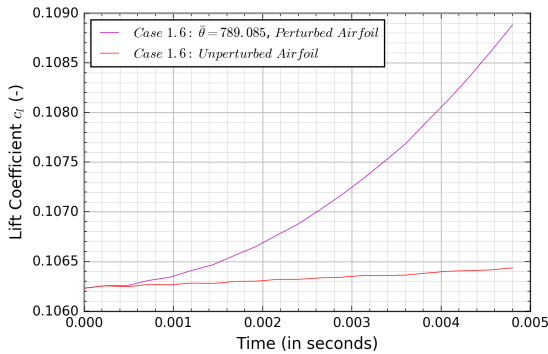


Figure 6.1: Case 1.6: c_l vs. $time$

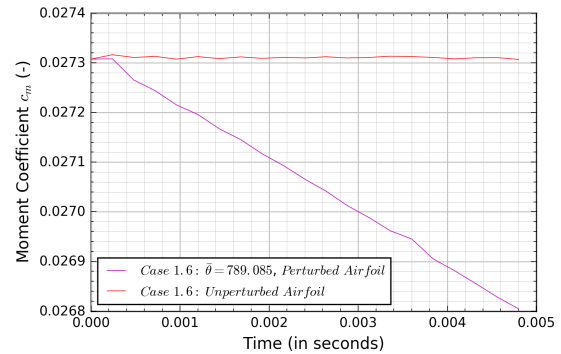


Figure 6.2: Case 1.6: c_m vs. $time$

This is clear from the Figure 6.1 & 6.2 above. Figure 6.1/6.2 shows the lift/moment response due to the perturbed airfoil and the lift/moment response due to the unperturbed airfoil for 20 time steps. The perturbation parameters are those of Case 1.6 and are given in Table 6.1. Here it is clearly visible that the lift response for the unperturbed airfoil changes, due to the fact that the initial solution was not the *converged enough* steady state solution. This can be seen for the moment as well. For a transient simulation of 20 time steps, the lift & moment for the unperturbed airfoil scenario will change less than 1%. However, this change can be significant because the LHS of Equation 6.4 represents the difference in the total lift of the perturbed and unperturbed state. So if the perturbed motion is very small for each time step, the order of magnitude of the change in perturbed c_l can be similar to the order of magnitude of the change in the *steady* state lift. Therefore, not taking into account the *steady* state lift at each time t , the values of the LHS can change drastically, resulting in an inaccurate computations of the linearized coefficients. Finally, in matrix form, Equation 6.4 can be written as

$$[A]\{\mathbf{b}\} = \{\mathbf{f}\}. \quad (6.5)$$

Since Equation 6.5 is an over-determined system because more than 3 time steps are included, the least squares method is used to obtain the linearized lift coefficients given by vector $\{\mathbf{b}\}$

$$\{\mathbf{b}\} = [[A]^T[A]]^{-1}[A]^T\{\mathbf{f}\}. \quad (6.6)$$

The exact same methodology is used to obtain the linearized moment coefficients.

6.3 Results

In this section, the constant coefficients for the linearized lift and moment models are found. The unsteady lift and moment, computed with the linearized coefficients, is compared to Theodorsen Theory and the nonlinear unsteady CFD results shown in Section 5. The perturbation defined by Equation 6.3 is imposed and the method mentioned in the previous section for determining the coefficients is used. In order to define the perturbation motion $\theta'(t)$ (and hence $\dot{\theta}'(t)$ & $\ddot{\theta}'(t)$), the perturbation rate $\bar{\theta}$, the time step Δt and the number of time steps must be specified. The extracted coefficients should be constant and independent of the linearization parameters chosen. However, preliminary results showed that this is not the case. Therefore, a more thorough analysis of the linearization method is carried out by computing the lift & moment coefficients for various linearization parameters.

The number of time steps chosen is 20. A larger amount of time steps can be taken but this would increase the simulation time and make the parametrization study inefficient. Furthermore, increasing the number of time steps should not influence the values of the obtained

coefficients. In order to fully define the perturbation equation, the perturbation rate $\bar{\theta}$ and time step Δt must be defined. However, to the author, it is hard to physically interpret the value of the perturbation rate $\bar{\theta}$ and it is unclear as to what time step Δt should be chosen. Instead, the final perturbation angle θ_{final} and the final perturbation angular velocity $\dot{\theta}'_{final}$ are prescribed and the perturbation rate $\bar{\theta}$, the final time t_{final} and time step Δt are calculated from the following relations

$$t_{final} = \frac{3\theta'_{final}}{\dot{\theta}'_{final}}; \quad \Delta t_{final} = \frac{3\theta'_{final}}{20\dot{\theta}'_{final}}; \quad \bar{\theta} = \frac{\dot{\theta}'_{final}{}^3}{27\theta_{final}{}^2}. \quad (6.7)$$

These relations are derived from the first two relations given by Equation 6.3 and evaluated at the final time. For $\theta'_{final} = 0.005^\circ$ and a $\dot{\theta}'_{final}$ of $100^\circ/s$, $50^\circ/s$, $25^\circ/s$, $12.5^\circ/s$, $6.25^\circ/s$, $3.125^\circ/s$ and $1.5625^\circ/s$, the perturbation rate $\bar{\theta}$ and time step Δt is computed (see Table 6.1) and the transient CFD simulations are carried out in order to obtain the lift and moment coefficients. The same is done for $\theta'_{final} = 0.05^\circ$ and a $\dot{\theta}'_{final}$ of $100^\circ/s$, $50^\circ/s$, $25^\circ/s$ and $12.5^\circ/s$ (see Table 6.4).

Since the linearized coefficients are computed by perturbing the airfoil about its midchord from the steady state angle of attack $\alpha_{ss} = 1^\circ$ and an inflow velocity of 50 m/s (i.e. $Re = 10^6$), the unsteady linearized lift and moment expressions are valid only for a perturbed airfoil with these parameters, as long as the perturbations are small. This includes sinusoidal perturbations as well. So, in order to analyze the validity of the coefficients in computing unsteady aerodynamic forces, the normalized amplitude and phase angle for the lift & moment is compared with Theodorsen Theory and the nonlinear unsteady CFD results. The expressions below describe the formulae for computing the linearized unsteady lift and moment of a sinusoidally pitching airfoil. They are obtained by substituting $\theta' = \bar{\theta}e^{i\omega t}$, $\dot{\theta}' = i\omega\bar{\theta}e^{i\omega t}$ & $\ddot{\theta}' = -\omega^2\bar{\theta}e^{i\omega t}$ into Equation 6.1 and 6.2

$$c_l \approx c_{l,ss} + \left[\left\{ \left. \frac{\partial c_l}{\partial \theta} \right|_s + i\omega \left. \frac{\partial c_l}{\partial \dot{\theta}} \right|_s - \omega^2 \left. \frac{\partial c_l}{\partial \ddot{\theta}} \right|_s \right\} \bar{\theta} \right] e^{i\omega t}, \quad (6.8)$$

$$c_m \approx c_{m,ss} + \left[\left\{ \left. \frac{\partial c_m}{\partial \theta} \right|_s + i\omega \left. \frac{\partial c_m}{\partial \dot{\theta}} \right|_s - \omega^2 \left. \frac{\partial c_m}{\partial \ddot{\theta}} \right|_s \right\} \bar{\theta} \right] e^{i\omega t}. \quad (6.9)$$

Note that here $\bar{\theta}$ represents the oscillation amplitude. The expression for the reduced frequency $k = \omega b/U$ is used to obtain the final form of the unsteady linearized lift and moment equations

$$c_l \approx c_{l,ss} + \left[\left\{ \left. \frac{\partial c_l}{\partial \theta} \right|_s + i \frac{Uk}{b} \left. \frac{\partial c_l}{\partial \dot{\theta}} \right|_s - \left(\frac{Uk}{b} \right)^2 \left. \frac{\partial c_l}{\partial \ddot{\theta}} \right|_s \right\} \bar{\theta} \right] e^{i\omega t}, \quad (6.10)$$

$$c_m \approx c_{m,ss} + \left[\left\{ \frac{\partial c_m}{\partial \theta} \Big|_s + i \frac{Uk}{b} \frac{\partial c_m}{\partial \dot{\theta}} \Big|_s - \left(\frac{Uk}{b} \right)^2 \frac{\partial c_m}{\partial \ddot{\theta}} \Big|_s \right\} \bar{\theta} \right] e^{i\omega t}. \quad (6.11)$$

For a given set of constant linearized lift and moment coefficients, the normalized amplitude and phase angles of the lift and moment can be computed as a function of the reduced frequency k . The linearized aerodynamic forces are not only dependent on k as is seen in Theodorsen Theory, but on the Reynolds Number as well, because that is the flow parameter about which the linearized models were built.

Note that the linearized unsteady lift and moment expressions given by Equations 6.10 and 6.11 are similar to the Theodorsen lift and moment equations (see Equation 5.4 and 5.10). The difference is the argument in the curly brackets.

Normalized Lift & Moment Amplitude: Linearized CFD Model

The linearized lift and moment normalized amplitudes are calculated in the same manner as for Theodorsen Theory, with the formulae shown below

$$\sigma_{c_{l,linearized}} = \frac{1}{c_{l,\alpha}} \left| \frac{\partial c_l}{\partial \theta} \Big|_s + i \frac{Uk}{b} \frac{\partial c_l}{\partial \dot{\theta}} \Big|_s - \left(\frac{Uk}{b} \right)^2 \frac{\partial c_l}{\partial \ddot{\theta}} \Big|_s \right|, \quad (6.12)$$

$$\sigma_{c_{m,linearized}} = \frac{1}{0.25c_{l,\alpha}} \left| \frac{\partial c_m}{\partial \theta} \Big|_s + i \frac{Uk}{b} \frac{\partial c_m}{\partial \dot{\theta}} \Big|_s - \left(\frac{Uk}{b} \right)^2 \frac{\partial c_m}{\partial \ddot{\theta}} \Big|_s \right|. \quad (6.13)$$

Lift & Moment Phase Angle: Linearized CFD Model

Equations 6.14 and 6.15 below give the linearized lift and moment phase angle. They are calculated also in the same manner as for Theodorsen Theory and are shown below

$$\phi_{c_{l,linearized}} = \tan^{-1} \left[\frac{\text{imag} \left[\left\{ \frac{\partial c_l}{\partial \theta} \Big|_s + i \frac{Uk}{b} \frac{\partial c_l}{\partial \dot{\theta}} \Big|_s - \left(\frac{Uk}{b} \right)^2 \frac{\partial c_l}{\partial \ddot{\theta}} \Big|_s \right\} \bar{\theta} \right]}{\text{real} \left[\left\{ \frac{\partial c_l}{\partial \theta} \Big|_s + i \frac{Uk}{b} \frac{\partial c_l}{\partial \dot{\theta}} \Big|_s - \left(\frac{Uk}{b} \right)^2 \frac{\partial c_l}{\partial \ddot{\theta}} \Big|_s \right\} \bar{\theta} \right]} \right], \quad (6.14)$$

$$\phi_{c_{m,linearized}} = \tan^{-1} \left[\frac{\text{imag} \left[\left\{ \frac{\partial c_m}{\partial \theta} \Big|_s + i \frac{Uk}{b} \frac{\partial c_m}{\partial \dot{\theta}} \Big|_s - \left(\frac{Uk}{b} \right)^2 \frac{\partial c_m}{\partial \ddot{\theta}} \Big|_s \right\} \bar{\theta} \right]}{\text{real} \left[\left\{ \frac{\partial c_m}{\partial \theta} \Big|_s + i \frac{Uk}{b} \frac{\partial c_m}{\partial \dot{\theta}} \Big|_s - \left(\frac{Uk}{b} \right)^2 \frac{\partial c_m}{\partial \ddot{\theta}} \Big|_s \right\} \bar{\theta} \right]} \right]. \quad (6.15)$$

6.3.1 Case 1

In this section, a detailed analysis of the results obtained for Case 1 is provided. For this case, the final perturbed angle of attack θ'_{final} is 0.005° and the final angular velocity $\dot{\theta}'_{final}$ is $100^\circ/s$, $50^\circ/s$, $25^\circ/s$, $12.5^\circ/s$, $6.25^\circ/s$, $3.125^\circ/s$ and $1.5625^\circ/s$. For each combination, the perturbation rate $\bar{\theta}$ and time step Δt is computed from the expressions given by Equation 6.7. The values computed are shown in Table 6.1 below. Various perturbations rates are considered to analyze whether the linearized lift and moment coefficients are independent of the perturbation rate. The final perturbed angle of attack is kept at a small value of 0.005° to ensure flow linearity. Note that for a given subcase, changing the time step (and hence number of time steps in order for θ'_{final} and t_{final} to remain the same value) will not influence the linearized lift and moment coefficients as is shown in the end of this section (**A Comment on the CFL Number** paragraph). With these parameters, the transient CFD simulations are carried out and the linearized lift and moment coefficients obtained are shown in Table 6.2 and 6.3, respectively. The CFL_{max} corresponding to the time step Δt is also given in Table 6.1 as well as the final angular acceleration (computed with last expression from Equation 6.3). Note that within this section θ'_{final} , $\dot{\theta}'_{final}$ and $\ddot{\theta}'_{final}$ are discussed in terms of degrees rather than radians. However, the perturbation rate $\bar{\theta}$ is discussed in radians.

Note that while the linearized lift and moment coefficients were computed for the whole range of $\dot{\theta}'_{final}$, the coefficients for a $\dot{\theta}'_{final}$ of $100^\circ/s$, $50^\circ/s$ and $25^\circ/s$ provide normalized amplitudes and phase angles that significantly differ from those obtained for a $\dot{\theta}'_{final}$ of $12.5^\circ/s$, $6.25^\circ/s$, $3.125^\circ/s$ and $1.5625^\circ/s$. Therefore, these cases are not included in the plots shown in this section but are presented in Appendix E.

Table 6.1: Case 1: Linearization Parameters, $\theta'_{final} = 0.005^\circ$

Case	$\dot{\theta}'_{final}$ ($^\circ/s$)	t_{final} (s)	Δt (s)	CFL_{max} (-)	$\bar{\theta}$ (rad/s ³)	$\ddot{\theta}'_{final}$ ($^\circ/s^2$)
1.1	100	1.5e-4	7.5e-6	1.59	25,856,729.659	1,333,333.333
1.2	50	3e-4	1.5e-5	3.19	3,232,091.207	333,333.333
1.3	25	6e-4	3e-5	6.37	404,011.401	83,333.333
1.4	12.5	1.2e-3	6e-5	12.74	50,501.425	20,833.333
1.5	6.25	2.4e-3	1.2e-4	25.49	6,312.678	5,208.333
1.6	3.125	4.8e-3	2.4e-4	50.97	789.085	1,302.083
1.7	1.5625	9.6e-3	4.8e-4	101.95	98.636	325.521

As can be seen from Table 6.1 above, the values of $\dot{\theta}'_{final}$ decrease by a factor of 2. This causes the t_{final} , Δt and hence CFL_{max} to increase by a factor of 2. At a certain $\dot{\theta}'_{final}$, the value of Δt and hence CFL_{max} will be too large for stable transient simulations to be possible. Therefore, the minimum final angular velocity considered is $1.5625^\circ/s$. As $\dot{\theta}'_{final}$ decreases by a factor of 2, the perturbation rate $\bar{\theta}$ decreases by a factor of 8 and the final angular acceleration $\ddot{\theta}'_{final}$ will decrease by a factor of 4. These relationships can be seen from the expressions given by Equations 6.3 and 6.7. A decreasing perturbation rate indicates that a longer time

is needed for the perturbed airfoil to reach 0.005° . This is why the time step increases. The time step could potentially remain the same, but then the total number of time steps must be increased from the current value of 20. Figure 6.3 below shows the perturbed motion θ' as a function of time for Cases 1.4 through 1.7. Indeed, as the perturbation rate $\bar{\theta}$ decreases, the severity of the unsteadiness decreases, i.e. it takes a longer time for the perturbed airfoil to reach a θ'_{final} of 0.005° . A decreasing perturbation rate also results in a lower angular velocity as can be seen from Figure 6.4 below. Note that the angular acceleration is not shown. This is because the magnitude varies by a factor of 8 from case to case (see Table 6.1) and as such the plot would be inconvenient for visualization.

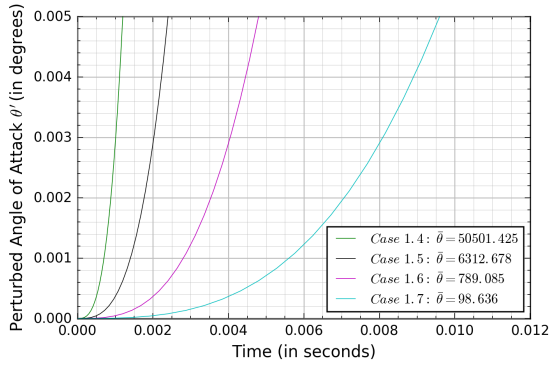


Figure 6.3: Case 1: θ' vs. *time*

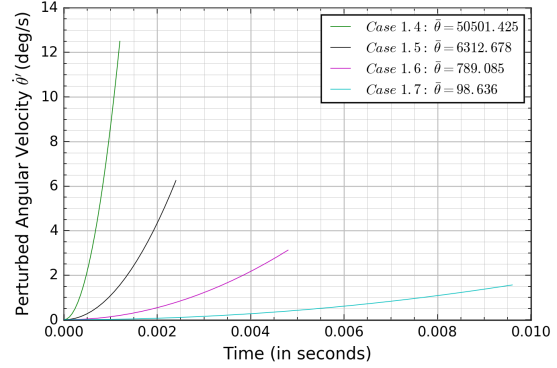


Figure 6.4: Case 1: $\dot{\theta}'$ vs. *time*

Figures 6.5 and 6.6 below show the change in lift and moment relative to the *steady* state as the airfoil is perturbed with a specific perturbation rate. The curves of different colors represent the Δc_l and Δc_m for various perturbation rates obtained by the transient CFD simulations. Note that these values represent the RHS (i.e. $\{\mathbf{f}\}$) of Equation 6.5. From Equation 6.6, the lift and moment coefficients are calculated. They are then multiplied by the $[A]$ matrix and plotted as stars to see how well they model the lift and moment response. Note that since the coefficients are obtained from an over-determined system, multiplying them by the $[A]$ matrix will not give an $\{\mathbf{f}\}$ vector identical to that obtained by the CFD simulations. However, the resemblance should be good, as is the case.

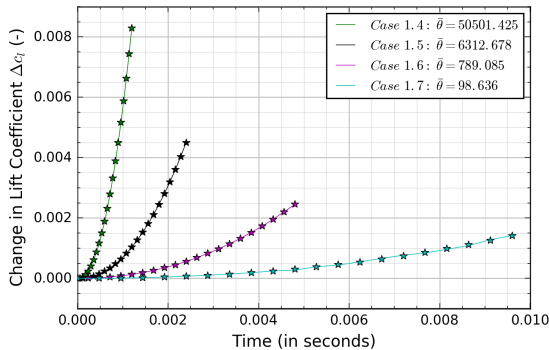


Figure 6.5: Case 1: Δc_l vs. *time*

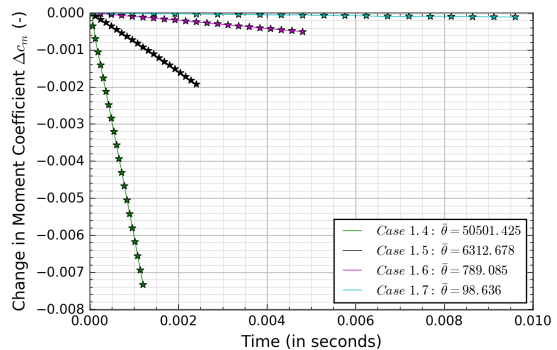


Figure 6.6: Case 1: Δc_m vs. *time*

A lower perturbation rate results in a slower perturbation motion and smaller change in the

lift and moment response. This is clear from Figure 6.5 and 6.6 above, where the highest change in lift and moment is for Case 1.4: $\theta = 50, 501.425$.

The computed linearized lift coefficients are shown in Table 6.2 below. Note that from now onwards, the linearized coefficients will be referred to without the $|_s$ for convenience. For example, $\frac{\partial c_l}{\partial \theta}|_s$ becomes $\frac{\partial c_l}{\partial \theta}$. Furthermore, the relative change between the coefficients of each subcase is also shown. For example, $\Delta(\partial c_l/\partial \theta)$ for Case 1.2 denotes the change in $\partial c_l/\partial \theta$ in relation to the value computed for Case 1.1. $\Delta(\partial c_l/\partial \theta)$ for Case 1.3 denotes the change in $\partial c_l/\partial \theta$ in relation to the value computed for Case 1.2 and so on. Clearly, the coefficients are not constant and the change is drastic for $\partial c_l/\partial \theta$ and $\partial c_l/\partial \dot{\theta}$. The change in $\partial c_l/\partial \ddot{\theta}$ is in the acceptable range.

Table 6.2: Case 1: Linearized Lift Coefficients, $\theta'_{final} = 0.005^\circ$

Case	$\partial c_l/\partial \theta$	$\Delta(\partial c_l/\partial \theta)$ (%)	$\partial c_l/\partial \dot{\theta}$	$\Delta(\partial c_l/\partial \dot{\theta})$ (%)	$\partial c_l/\partial \ddot{\theta}$	$\Delta(\partial c_l/\partial \ddot{\theta})$ (%)
1.1	38.041	-	3.117e-2	-	-5.496e-7	-
1.2	28.884	-24.071	3.168e-2	1.637	-5.852e-7	-6.467
1.3	16.320	-43.498	3.408e-2	7.597	-7.818e-7	-33.601
1.4	6.867	-57.921	3.729e-2	9.407	-1.220e-6	-56.031
1.5	4.208	-38.728	3.955e-2	6.066	-2.020e-6	-65.589
1.6	3.300	-21.583	4.097e-2	3.593	-3.208e-6	-58.810
1.7	4.093	24.043	3.969e-2	-3.135	-4.623e-6	-44.098

The computed linearized moment coefficients and their relative change are shown in Table 6.3 below. Clearly, even for the linearized moment, the coefficients are not constant and the change is drastic for $\partial c_m/\partial \theta$ and $\partial c_m/\partial \dot{\theta}$. The change in $\partial c_m/\partial \ddot{\theta}$ is minimal. Note how $\partial c_l/\partial \dot{\theta}$ was relatively constant (see Table 6.2) while for the moment coefficients $\partial c_m/\partial \ddot{\theta}$ is almost completely constant.

Table 6.3: Case 1: Linearized Moment Coefficients, $\theta'_{final} = 0.005^\circ$

Case	$\partial c_m/\partial \theta$	$\Delta(\partial c_m/\partial \theta)$ (%)	$\partial c_m/\partial \dot{\theta}$	$\Delta(\partial c_m/\partial \dot{\theta})$ (%)	$\partial c_m/\partial \ddot{\theta}$	$\Delta(\partial c_m/\partial \ddot{\theta})$ (%)
1.1	-36.207	-	1.691e-3	-	-1.922e-5	-
1.2	-12.829	64.566	5.722e-4	-66.160	-1.922e-5	0
1.3	-4.331	66.239	-5.166e-4	-190.270	-1.919e-5	0.187
1.4	-0.487	88.759	-1.530e-3	-196.174	-1.913e-5	0.315
1.5	0.267	154.914	-1.987e-3	-29.859	-1.904e-5	0.429
1.6	0.767	186.803	-2.455e-3	-23.543	-1.925e-5	-1.105
1.7	0.873	13.945	-2.885e-3	-17.536	-1.815e-5	5.721

Using the computed linearized lift and moment coefficients given in Table 6.2 and 6.3, the normalized amplitudes and phase angles are computed as a function of reduced frequency k for each case using Equation 6.12 - 6.15 and compared to the nonlinear unsteady CFD results and Theodorsen Theory. As a reminder to the reader, the results for Case 1.1 - 1.3 are not shown because the normalized amplitudes drastically vary from those of the remaining cases. Therefore, the normalized amplitudes along with the phase angles is included in Appendix E (see Figures E.5-E.8).

Figures 6.7 and 6.8 show the normalized amplitudes and phase angles of the linearized lift for Cases 1.4 - 1.7. The general trend is: as the perturbation rate decreases, the normalized amplitude decreases. Case 1.7 is an exception, where the normalized amplitude increases in relation to Case 1.6. For the phase angle, as the perturbation rate decreases, the phase angle increases. Again, Case 1.7 is an exception.

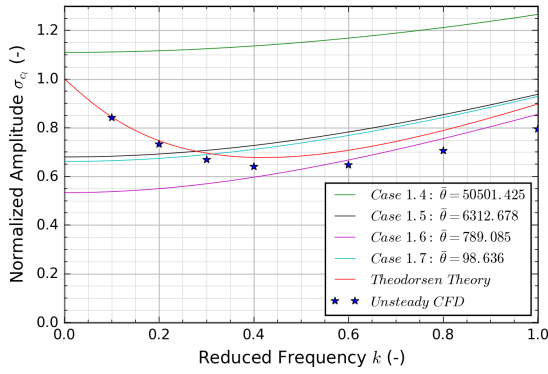


Figure 6.7: Case 1: σ_{c_l} vs. k (for linearized lift)

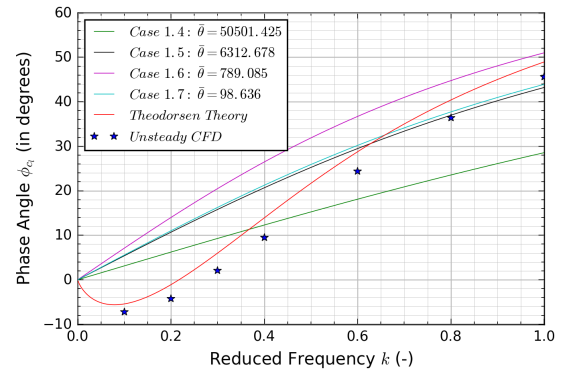


Figure 6.8: Case 1: ϕ_{c_l} vs. k (for linearized lift)

The best result for the normalized amplitude is obtained with a perturbation rate $\bar{\theta} = 789.085$ (i.e. Case 1.6). While the result is satisfactory for reduced frequencies larger than 0.4, the difference from the unsteady CFD results for lower reduced frequencies is too large. For $k \approx 0.4$, the difference is $\approx 5\%$, but grows to $\approx 45\%$ as $k \rightarrow 0$. On the other hand, a perturbation rate of $\bar{\theta} = 6,312.678$ (i.e. Case 1.5) and $\bar{\theta} = 98.636$ (i.e. Case 1.7) provide better results for lower reduced frequencies. For the phase angle, Case 1.6 does not give as good of results as Case 1.5 & 1.7. Case 1.5 & 1.7 provide good results for a higher reduced frequency. However for lower reduced frequencies, none of the cases (not even Case 1.5 & 1.7) are able to predict a negative phase lag. This is due to the $\partial c_l / \partial \theta$ coefficient being positive (see Table 6.2).

Figure 6.9 and 6.10 below show normalized amplitudes and phase angles for the linearized moment for Cases 1.4 - 1.7. However, note that the phase angle of Case 1.4 is not plotted in Figure 6.10. This is because the phase angle varies from $\approx -180^\circ$ at $k \approx 0$ and rises to $\approx -150^\circ$ as $k \rightarrow 1$ and as such varies drastically from the remaining cases. Nevertheless, the linearized moment phase angle of Case 1.4 is shown in Appendix E (see Figure E.8).

The normalized amplitude increases as the perturbation rate decreases. This is opposite from what can be seen in the normalized amplitude for the linearized lift (see Figure 6.7). The best result is obtained for a perturbation rate of $\bar{\theta} = 98.636$ (i.e. Case 1.7). However, the results

for this case are not satisfactory. For reduced frequencies of 0.8 and lower, the difference between Case 1.7 and the unsteady CFD results is 10% and grows as $k \rightarrow 0$. At $k = 0$, the difference is $\approx 44\%$. Surprisingly, Case 1.5 gives the best phase angle in comparison to the unsteady CFD and Theodorsen Results, while the normalized amplitude is completely off. Case 1.6 & 1.7 give reasonable results for the phase angle.

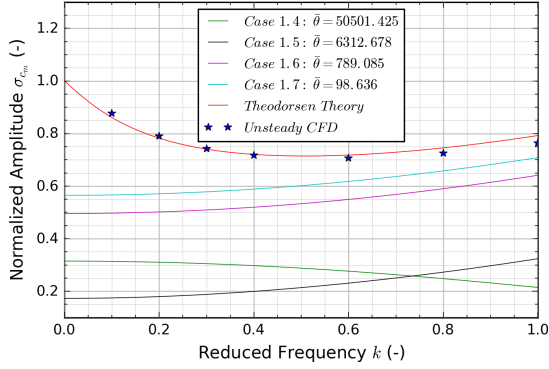


Figure 6.9: Case 1: σ_{c_m} vs. k (for linearized moment)

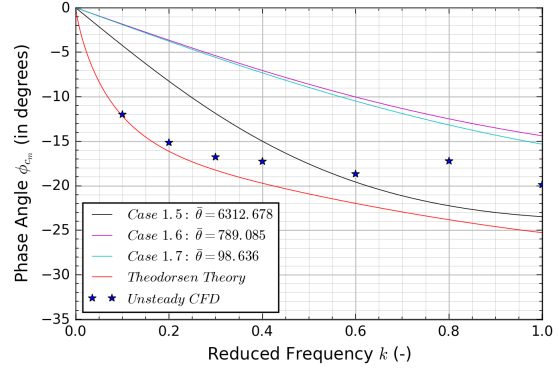


Figure 6.10: Case 1: ϕ_{c_m} vs. k (for linearized moment)

A comment on the CFL Number

Due to the fact that the number of time steps and the final perturbed angle of attack is kept constant, a lower perturbation rate results in increasing the time step Δt (i.e. CFL_{max}). If the perturbation rate is too low thus resulting in a too high CFL number, numerical wiggles can appear in the unsteady lift and moment results. This can be seen from Figures 6.11 and 6.12 below.

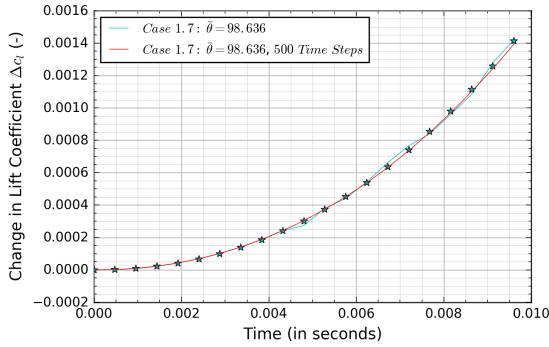


Figure 6.11: Case 1.7: Δc_l vs. *time*

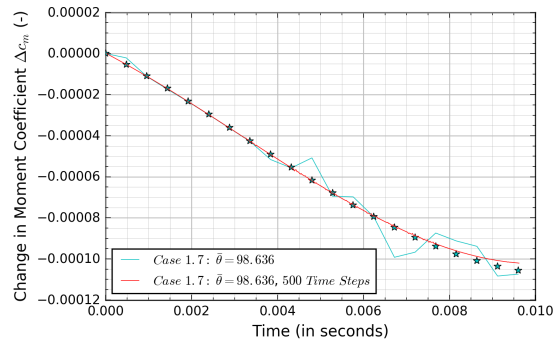


Figure 6.12: Case 1.7: Δc_m vs. *time*

Case 1.7 with 20 time steps is shown in Figure 6.11 & 6.12 as the cyan curve. The cyan stars are the computed linearized lift and moment coefficients for this case. Clearly, there are numerical wiggles. This is due to the fact that the number of time steps is limited to 20 and the perturbation rate is small which results in a time step Δt of $4.8e-4s$ and a CFL_{max} of 101.95. To ensure that these numerical wiggles are due to a large CFL_{max} , Case 1.7 is simulated with 500 time steps and shown as the red curve in Figures 6.11 & 6.12. Here Δt

is $1.92e-5s$ and CFL_{max} is 4.08. Clearly, a smaller CFL number eliminates the numerical wiggles. Furthermore, the fact that the results match well with the coefficients calculated from Case 1.7 with just 20 time steps imply that the time step (i.e. CFL number) or number of time steps will not affect the solution, as was expected. Hence the only true parameter that causes the linearized lift and moment coefficients to change is the change of the perturbation rate.

Summary of Case 1 Results

The results of Case 1 show that the coefficients are not independent of the linearization parameters (i.e. the perturbation rate), because all the coefficients except for $\partial c_l / \partial \dot{\theta}$ & $\partial c_m / \partial \ddot{\theta}$ vary drastically. This implies that all of the perturbed cubic motions cannot be predicted with a single set of coefficients. Furthermore, it was also shown that no set of linearized lift and moment coefficients could be used to accurately predict oscillatory airfoil motion, i.e. the lift/moment normalized amplitudes and phase angles. Evidence of this is given in the normalized amplitude and phase angles plots for the lift and moment (see Figures 6.7 - 6.10). However, it was noticed that lower perturbation rates $\bar{\theta}$ give the better results.

6.3.2 Case 2

In this section, an analysis of the results obtained for Case 2 is provided. For this case, θ'_{final} of Case 1 is increased by a factor of 10 and is 0.05° in order to see whether the results obtained for the linearized lift and moment coefficients might improve. Similar to Case 1, the final angular velocity $\dot{\theta}'_{final}$ is $100^\circ/s$, $50^\circ/s$, $25^\circ/s$, $12.5^\circ/s$. Values lower than $12.5^\circ/s$ are not considered because it would result in a too high CFL_{max} number for stable computations to be possible. For each combination of θ'_{final} and $\dot{\theta}'_{final}$, the perturbation rate $\bar{\theta}$ and time step Δt is computed using the expressions given by Equation 6.7. The values computed are shown in Table 6.4 below. With these parameters, the transient CFD simulations are carried out and the linearized lift and moment coefficients obtained are shown in Table 6.5 and 6.6, respectively. Furthermore, note that Table 6.4 shows the final angular acceleration $\ddot{\theta}'_{final}$, computed with the last expression of Equation 6.3, as well as the final time and CFL_{max} number. Note that for the same $\dot{\theta}'_{final}$ as in Case 1, the perturbation rate will be smaller by a factor of 100 (see Equation 6.7). Previously, it was shown that the linearized coefficients are dependent only of the perturbation rate. Therefore, in Case 2 a $\dot{\theta}'_{final}$ of $100^\circ/s$, $50^\circ/s$ and $25^\circ/s$ should give much better results for the lift & moment normalized amplitudes and phase angles than for the same $\dot{\theta}'_{final}$ in Case 1, because the perturbation rate is much smaller.

Table 6.4: Case 2: Linearization Parameters, $\theta'_{final} = 0.05^\circ$

Case	$\dot{\theta}'_{final}$ ($^\circ/s$)	t_{final} (s)	Δt (s)	CFL_{max} (-)	$\bar{\theta}$ (rad/s ³)	$\ddot{\theta}'_{final}$ ($^\circ/s^2$)
2.1	100	1.5e-3	7.5e-5	15.93	258,567.297	133,333.333
2.2	50	3e-3	1.5e-4	31.86	32,320.912	33,333.333
2.3	25	6e-3	3e-4	63.72	4,040.114	8,333.333
2.4	12.5	1.2e-2	6e-4	127.43	505.014	2,083.333

Figures 6.13 & 6.14 below show the perturbed motion and angular velocity for all cases. As the perturbation rate decreases, the perturbation motion becomes slower and it takes a larger time to reach θ'_{final} of 0.05° . This also results in a smaller angular velocity at a specific time.

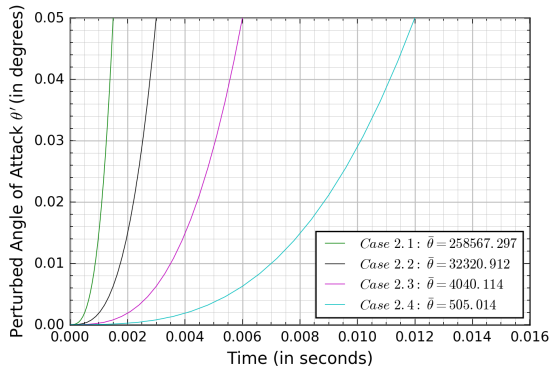


Figure 6.13: Case 2: θ' vs. time

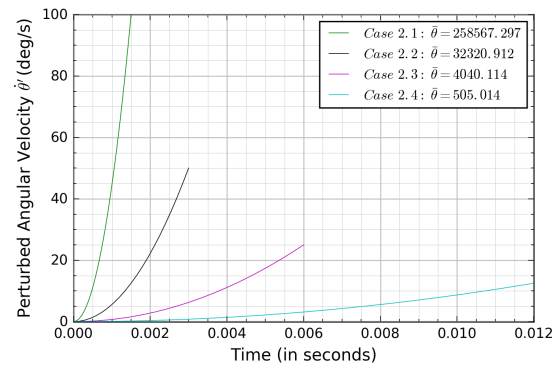


Figure 6.14: Case 2: $\dot{\theta}'$ vs. time

Figures 6.15 and 6.16 below show the change in lift and moment relative to the *steady* state as the airfoil is perturbed with a specific perturbation rate. As in Case 1, the curves of different colors represent the Δc_l and Δc_m for various amplitudes obtained by the transient CFD simulations. Note that these values represent the RHS (i.e. $\{\mathbf{f}\}$) of Equation 6.5. From Equation 6.6, the lift and moment coefficients are calculated. They are then multiplied by the $[A]$ matrix and plotted as stars to see how well they model the lift and moment response. Note that since the coefficients are obtained from an over-determined system, multiplying them by the $[A]$ matrix will not give an $\{\mathbf{f}\}$ vector identical to that obtained by the CFD simulations. However, the resemblance should be good, as is the case.

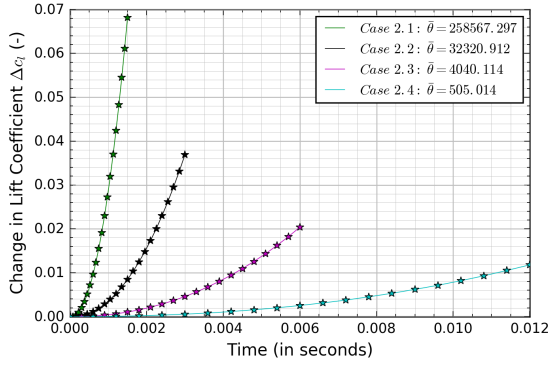


Figure 6.15: Case 2: Δc_l vs. *time*

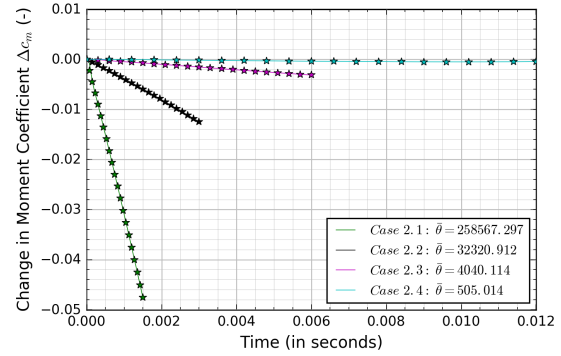


Figure 6.16: Case 2: Δc_m vs. *time*

In general, it can be seen from the figures above that the change in lift Δc_l and moment Δc_m is larger than for Case 1. This is due to the fact that the final perturbation angle is an order of magnitude larger (θ'_{final} is 0.005° for Case 1 and 0.05° for Case 2).

Table 6.5 below shows the linearized lift coefficients for the different linearization parameters (i.e. Cases 2.1-2.4). The relative change between the coefficients of each subcase is also shown. For example, $\Delta(\partial c_l/\partial \theta)$ for Case 2.2 denotes the change in $\partial c_l/\partial \theta$ in relation to the value computed for Case 2.1. $\Delta(\partial c_l/\partial \theta)$ for Case 2.3 denotes the change in $\partial c_l/\partial \theta$ in relation to the value computed for Case 2.2 and so on. Note that this is the same for the moment coefficients shown in Table 6.6. Finally, similarly to Case 1, $\partial c_l/\partial \dot{\theta}$ remains relatively constant while the other two coefficients change drastically.

Table 6.5: Case 2: Linearized Lift Coefficients, $\theta'_{final} = 0.05^\circ$

Case	$\partial c_l/\partial \theta$	$\Delta(\partial c_l/\partial \theta)$ (%)	$\partial c_l/\partial \dot{\theta}$	$\Delta(\partial c_l/\partial \dot{\theta})$ (%)	$\partial c_l/\partial \ddot{\theta}$	$\Delta(\partial c_l/\partial \ddot{\theta})$ (%)
2.1	6.111	-	3.789e-2	-	-1.414e-6	-
2.2	4.004	-34.469	3.982e-2	5.087	-2.260e-6	-59.751
2.3	3.426	-14.446	4.112e-2	3.270	-3.777e-6	-67.136
2.4	3.207	-6.402	4.259e-2	3.571	-8.008e-6	-112.028

Table 6.6 below shows the linearized moment coefficients for the different linearization parameters (i.e. Cases 2.1-2.4). Here $\partial c_m / \partial \ddot{\theta}$ remains relatively constant while the other two coefficients change drastically. The same trend was observed for the linearized moment coefficients of Case 1.

Table 6.6: Case 2: Linearized Moment Coefficients, $\theta'_{final} = 0.05^\circ$

Case	$\partial c_m / \partial \theta$	$\Delta(\partial c_m / \partial \theta)$ (%)	$\partial c_m / \partial \dot{\theta}$	$\Delta(\partial c_m / \partial \dot{\theta})$ (%)	$\partial c_m / \partial \ddot{\theta}$	$\Delta(\partial c_m / \partial \ddot{\theta})$ (%)
2.1	-0.138	-	-1.770e-3	-	-1.906e-5	-
2.2	0.553	501.989	-2.224e-3	-25.682	-1.896e-5	0.540
2.3	0.834	50.810	-2.615e-3	-17.594	-1.874e-5	1.153
2.4	1.011	21.275	-3.246e-3	-24.132	-1.784e-5	4.793

Using the computed linearized lift and moment coefficients given in Table 6.5 and 6.6, the lift & moment normalized amplitudes and phase angles as a function of reduced frequency are computed for each case using Equation 6.12 - 6.15 and compared to the nonlinear unsteady CFD results and Theodorsen Theory. In this way, the unsteady loads that each set of linearized coefficient give can be validated for different oscillation frequencies.

Figures 6.17 and 6.18 show the normalized amplitudes and phase angles of the linearized lift for Cases 2.1 - 2.4. The general trend is: as the perturbation rate decreases, the normalized amplitude decreases. For the phase angle, as the amplitude decreases, the phase angle increases.

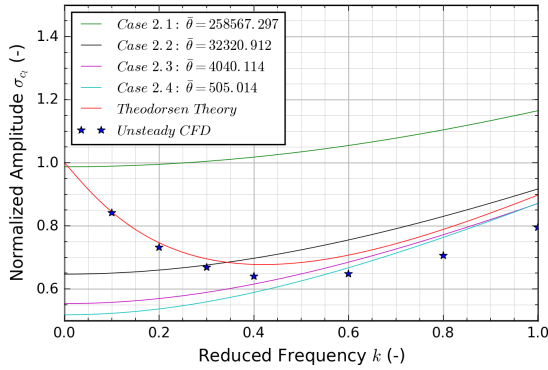


Figure 6.17: Case 2: σ_{c_l} vs. k (for linearized lift)

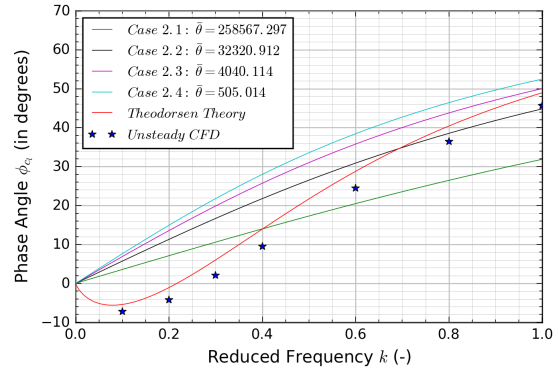


Figure 6.18: Case 2: ϕ_{c_l} vs. k (for linearized lift)

The best results for the normalized amplitude is obtained with a perturbation rate of $\bar{\theta} = 4,041.114$ (i.e. Case 2.3) and $\bar{\theta} = 505.014$ (i.e. Case 2.4). While the results are satisfactory for reduced frequencies larger than 0.4, the difference from the unsteady CFD results for lower reduced frequencies is too large. For the phase angle, the best results are obtained by $\bar{\theta} = 32,320.912$ (i.e. Case 2.2), particularly for higher reduced frequencies. However for lower

reduced frequencies, none of the cases (not even Case 2.2) are able to predict a negative phase lag. This is due to the $\partial c_l/\partial \dot{\theta}$ coefficient being positive (see Table 6.5).

Figure 6.19 and 6.20 below show normalized amplitudes and phase angles for the linearized moment for Cases 2.1 - 2.4. However, note that the phase angle of Case 2.1 is not plotted in Figure 6.20. This is because the phase angle varies from $\approx -180^\circ$ at $k \approx 0$ and rises to $\approx -70^\circ$ as $k \rightarrow 1$ and as such drastically varies from the remaining cases. However, it is shown in Figure E.9 of Appendix E.

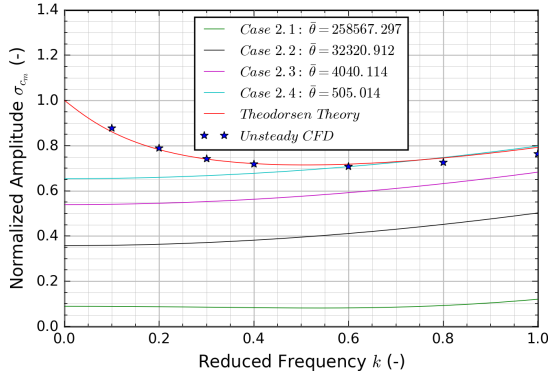


Figure 6.19: Case 2: σ_{c_m} vs. k (for linearized moment)

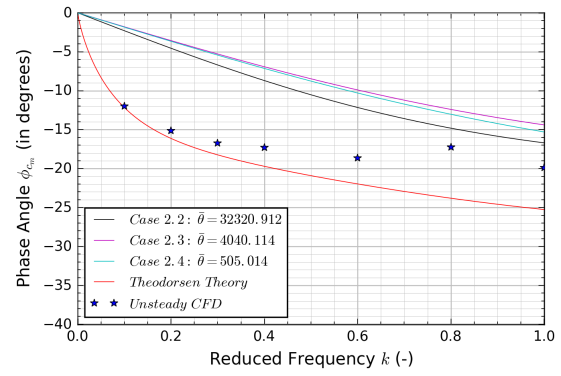


Figure 6.20: Case 2: ϕ_{c_m} vs. k (for linearized moment)

The normalized amplitude increases as the perturbation rate decreases. This is opposite from what can be seen in the normalized amplitude for the linearized lift (see Figure 6.17). The best result is obtained for a perturbation rate of $\bar{\theta} = 505.014$ (i.e. Case 2.4). For this case, the results are excellent for reduced frequencies higher than 0.4. However, as $k \rightarrow 0$ the error increases to $\approx 35\%$. Case 2.2, 2.3 & 2.4 all gives similar phase angles. Their agreement with Theodorsen Theory and the nonlinear CFD simulations is relatively good.

Summary of Case 2 Results

In general, the same conclusions can be drawn as from the Case 1 results. Clearly, the linearized lift and moment coefficients change as the linearization parameters change (apart for $\partial c_l/\partial \dot{\theta}$ & $\partial c_m/\partial \dot{\theta}$). This again implies that a cubic perturbation of different perturbation rates cannot be predicted with the same linearized coefficients. Furthermore, the lift & moment normalized amplitudes and phase angles were computed for each set of linearized lift & moment coefficients. The general trend was that the lower the perturbation rate, the better the results, but that is not to say the lowest perturbation rate provided the best result. It was noticed that there is no single subcase of Case 2 that provides the best results for both the lift & moment normalized amplitudes and phase angles. Finally, it is important to note that the overall agreement between the linearized results and the Theodorsen/nonlinear CFD results are unsatisfactory.

6.3.3 Evaluation of the Linearized Aerodynamic CFD Model

Both Case 1 and Case 2 consist of a variety of subcases. Each subcase has a different perturbation rate and time step, while the number of time steps is kept at 20. The premise was that the linearized lift and moment coefficients would be independent of the linearization parameters chosen and that once a set of lift and moment coefficients were computed, they could be used to compute the unsteady lift and moment of any type of motion $\theta'(t)$ using Equation 6.1 and 6.2. The only restrictions were that the airfoil is subject to an inflow of 50 m/s (i.e. $Re = 10^6$) and pitches about its midchord and a steady state angle of attack of 1° with relatively small angles, such that flow linearity is preserved. The reason for this restriction is because these are the parameters around which the linearized aerodynamic lift and moment models were constructed. Since the linearized aerodynamic models should provide accurate results for any type of perturbed motion, they should be able to model oscillatory airfoil motion. The linearized lift and moment that describes the unsteady forces for oscillatory motion is given by Equations 6.10 and 6.11. Their normalized amplitudes and phase angles are computed as a function of the reduced frequency with Equations 6.12 - 6.15.

First, it was shown that the coefficients of the linearized lift and moment were not constant and were not independent of the linearization parameters, i.e. the perturbation rate. Second, it was shown that no set of constant lift and moment coefficients could adequately model the unsteady lift and moment of oscillatory airfoil motion. Evidence of this is depicted in the normalized amplitude and phase angle plots (see Figures 6.7 - 6.10 and 6.17 - 6.20).

Therefore, the question arises whether the linearized lift and moment models (given by Equations 6.1 and 6.2) with constant coefficients can actually accurately model at least oscillatory motion. The results shown for Case 1 and Case 2 argue that this is not possible. However, in order to be able to come to a conclusion with confidence, an additional analysis is carried out. Instead of computing the coefficients of the linearized lift and moment models using a cubic perturbation shown in Equation 6.3, the coefficients are found by perturbing the airfoil about its midchord and the steady state angle of attack $\alpha_{ss} = 1^\circ$ with the following function

$$\theta' = \bar{\theta}\cos(\omega t); \quad \dot{\theta}' = -\omega\bar{\theta}\sin(\omega t); \quad \ddot{\theta}' = -\omega^2\bar{\theta}\cos(\omega t) \quad (6.16)$$

where ω is in radians and is related to the reduced frequency as $\omega = Uk/b$. U is the freestream velocity of 50 m/s and b is the half chord length of 0.4976m. $\bar{\theta}$ is the oscillation amplitude in radians and is taken as the equivalent of 1° . Note that the expressions in Equation 6.16 are just the real part of $\theta' = \bar{\theta}e^{i\omega t}$, $\dot{\theta}' = i\omega\bar{\theta}e^{i\omega t}$ & $\ddot{\theta}' = -\omega^2\bar{\theta}e^{i\omega t}$, respectively. For such a perturbation, a solution for the unsteady lift and moment exists, i.e. Theodorsen Theory. Therefore, a system of equations for lift, similar to that shown in Section 6.2.1 can be created for a specific ω . Then the coefficients can be computed for a range of ω (i.e. k) and this will give insight to whether the coefficients can truly be constant. Perturbing the airfoil for n time steps in order to compute the linearized lift coefficients results in n equations of the

form of Equation 6.1. This can be re-written as the following system of equations

$$\begin{Bmatrix} \Delta c_l(k_i, t_1) \\ \Delta c_l(k_i, t_2) \\ \vdots \\ \Delta c_l(k_i, t_n) \end{Bmatrix} = \begin{bmatrix} \bar{\theta} \cos(\frac{U}{b} k_i t_1) & -\frac{U}{b} k_i \bar{\theta} \sin(\frac{U}{b} k_i t_1) & -(\frac{U}{b} k_i)^2 \bar{\theta} \cos(\frac{U}{b} k_i t_1) \\ \bar{\theta} \cos(\frac{U}{b} k_i t_2) & -\frac{U}{b} k_i \bar{\theta} \sin(\frac{U}{b} k_i t_2) & -(\frac{U}{b} k_i)^2 \bar{\theta} \cos(\frac{U}{b} k_i t_2) \\ \vdots & \vdots & \vdots \\ \bar{\theta} \cos(\frac{U}{b} k_i t_n) & -\frac{U}{b} k_i \bar{\theta} \sin(\frac{U}{b} k_i t_n) & -(\frac{U}{b} k_i)^2 \bar{\theta} \cos(\frac{U}{b} k_i t_n) \end{bmatrix} \begin{Bmatrix} \left. \frac{\partial c_l}{\partial \theta} \right|_s \\ \left. \frac{\partial c_l}{\partial \dot{\theta}} \right|_s \\ \left. \frac{\partial c_l}{\partial \ddot{\theta}} \right|_s \end{Bmatrix} \quad (6.17)$$

where in matrix form this is $\{\mathbf{f}\} = [A]\{\mathbf{b}\}$. The number of time steps is defined by n and k_i is the reduced frequency of the imposed motion. Notice how the relation $\omega = Uk/b$ is used when constructing the $[A]$ matrix from the expressions given by Equation 6.16. Furthermore, $\Delta c_l(k_i, t_1) = c_l(k_i, t_1) - c_{l,ss}$ and so on. $c_l(k_i, t_j)$ is computed by calculating the real part of the Theodorsen lift (see Equation 5.4) for a specific k_i and t_j . If the linearized moment coefficients are to be computed, $c_m(k_i, t_j)$ in $\{\mathbf{f}\}$ is defined by the real part of the Theodorsen moment (see Equation 5.10) for a specific k_i and t_j . Furthermore, then vector $\{\mathbf{b}\}$ is constructed of linearized moment coefficients $\partial c_m / \partial \theta$, $\partial c_m / \partial \dot{\theta}$ and $\partial c_m / \partial \ddot{\theta}$. The $[A]$ matrix remains identical.

The vector $\{\mathbf{b}\}$ of the overdetermined system is computed with the least squares method and $\{\mathbf{b}\} = [[A]^T[A]]^{-1}[A]^T\{\mathbf{f}\}$. This is identical to what was done in Section 6.2.1. However, column 1 and column 3 of the $[A]$ matrix are linearly dependent. This implies that the inverse of $[A]^T[A]$ does not exist because $[A]^T[A]$ is singular. In order to overcome this problem, the following is proposed: it is unsure whether the linearized lift and moment coefficients are constant for any reduced frequency k_i ; however, it can be assumed that the coefficients will be constant for reduced frequencies close to a specific k_i . For example, for $k = [0.0999, 0.1, 0.1001]$ it assumed that the computed linearized coefficients are constant. Therefore, the system $[A]\{\mathbf{b}\} = \{\mathbf{f}\}$ can be constructed of multiple reduced frequencies such that it results in the system of equation given on the next page.

In the system of equations given by Equation 6.18, the first n equations are for the imposed frequency $k_{i-1} = k_i - 0.0001$. The second n equations are for the imposed frequency k_i and the third n equations are for the imposed frequency $k_{i+1} = k_i + 0.0001$. A time step of $n = 1000$ is chosen. The actual time step corresponding to each reduced frequency k_{i-1} , k_i and k_{i+1} are calculated in the following manner: For example, from the relation $k = \omega b / U$, ω_i can be calculated. From ω_i , the period T_i is computed. Dividing the period by 1000 will result is the time step Δt_{k_i} . In the same manner $\Delta t_{k_{i-1}}$ and $\Delta t_{k_{i+1}}$ can be computed. Having said this, the system of equation given by Equation 6.18 is built for each k_i in the range of $[0.01:0.01:1]$. For each k_i , the linearized lift coefficients given by $\{\mathbf{b}\}$ can be found. The same procedure is carried out for computing the linearized moment coefficients.

$$\left\{ \begin{array}{l} \Delta c_l(k_{i-1}, t_1) \\ \Delta c_l(k_{i-1}, t_2) \\ \vdots \\ \Delta c_l(k_{i-1}, t_n) \\ \Delta c_l(k_i, t_1) \\ \Delta c_l(k_i, t_2) \\ \vdots \\ \Delta c_l(k_i, t_n) \\ \Delta c_l(k_{i+1}, t_1) \\ \Delta c_l(k_{i+1}, t_2) \\ \vdots \\ \Delta c_l(k_{i+1}, t_n) \end{array} \right\} = \begin{bmatrix} \bar{\theta} \cos(\frac{U}{b} k_{i-1} t_1) & -\frac{U}{b} k_{i-1} \bar{\theta} \sin(\frac{U}{b} k_{i-1} t_1) & -(\frac{U}{b} k_{i-1})^2 \bar{\theta} \cos(\frac{U}{b} k_{i-1} t_1) \\ \bar{\theta} \cos(\frac{U}{b} k_{i-1} t_2) & -\frac{U}{b} k_{i-1} \bar{\theta} \sin(\frac{U}{b} k_{i-1} t_2) & -(\frac{U}{b} k_{i-1})^2 \bar{\theta} \cos(\frac{U}{b} k_{i-1} t_2) \\ \vdots & \vdots & \vdots \\ \bar{\theta} \cos(\frac{U}{b} k_{i-1} t_n) & -\frac{U}{b} k_{i-1} \bar{\theta} \sin(\frac{U}{b} k_{i-1} t_n) & -(\frac{U}{b} k_{i-1})^2 \bar{\theta} \cos(\frac{U}{b} k_{i-1} t_n) \\ \bar{\theta} \cos(\frac{U}{b} k_i t_1) & -\frac{U}{b} k_i \bar{\theta} \sin(\frac{U}{b} k_i t_1) & -(\frac{U}{b} k_i)^2 \bar{\theta} \cos(\frac{U}{b} k_i t_1) \\ \bar{\theta} \cos(\frac{U}{b} k_i t_2) & -\frac{U}{b} k_i \bar{\theta} \sin(\frac{U}{b} k_i t_2) & -(\frac{U}{b} k_i)^2 \bar{\theta} \cos(\frac{U}{b} k_i t_2) \\ \vdots & \vdots & \vdots \\ \bar{\theta} \cos(\frac{U}{b} k_i t_n) & -\frac{U}{b} k_i \bar{\theta} \sin(\frac{U}{b} k_i t_n) & -(\frac{U}{b} k_i)^2 \bar{\theta} \cos(\frac{U}{b} k_i t_n) \\ \bar{\theta} \cos(\frac{U}{b} k_{i+1} t_1) & -\frac{U}{b} k_{i+1} \bar{\theta} \sin(\frac{U}{b} k_{i+1} t_1) & -(\frac{U}{b} k_{i+1})^2 \bar{\theta} \cos(\frac{U}{b} k_{i+1} t_1) \\ \bar{\theta} \cos(\frac{U}{b} k_{i+1} t_2) & -\frac{U}{b} k_{i+1} \bar{\theta} \sin(\frac{U}{b} k_{i+1} t_2) & -(\frac{U}{b} k_{i+1})^2 \bar{\theta} \cos(\frac{U}{b} k_{i+1} t_2) \\ \vdots & \vdots & \vdots \\ \bar{\theta} \cos(\frac{U}{b} k_{i+1} t_n) & -\frac{U}{b} k_{i+1} \bar{\theta} \sin(\frac{U}{b} k_{i+1} t_n) & -(\frac{U}{b} k_{i+1})^2 \bar{\theta} \cos(\frac{U}{b} k_{i+1} t_n) \end{bmatrix} \left\{ \begin{array}{l} \frac{\partial c_l}{\partial \theta} \Big|_s \\ \frac{\partial c_l}{\partial \theta} \Big|_s \\ \frac{\partial c_l}{\partial \theta} \Big|_s \end{array} \right\} \quad (6.18)$$

The computed linearized lift and moment coefficients are depicted in Figures 6.21 - 6.26. It is clear that these coefficients are not constant. Both $\partial c_l / \partial \theta$ and $\partial c_m / \partial \theta$ vary $\approx 40\%$ from $k \approx 0$ to $k = 1$. $\partial c_l / \partial \dot{\theta}$ varies more than 100% even changes its sign. $\partial c_m / \partial \dot{\theta}$ also varies almost 100%. Furthermore, $\partial c_l / \partial \ddot{\theta}$ varies $\approx 100\%$ between $k \approx 0$ and $k \approx 0.4$. After $k \approx 0.4$, $\partial c_l / \partial \ddot{\theta}$ is a small non-zero value and is relatively constant compared to the values of $\partial c_l / \partial \dot{\theta}$ for $k < 0.4$. A similar trend is observed for $\partial c_m / \partial \ddot{\theta}$. However, here the value of $\partial c_m / \partial \ddot{\theta}$ for $k > 0.6$ becomes negative.

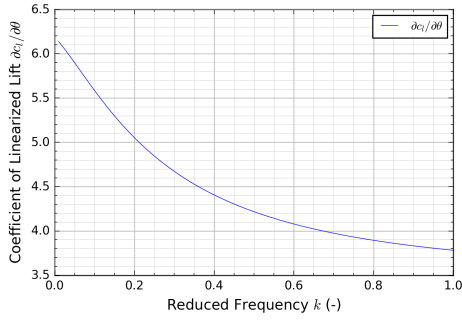


Figure 6.21: $\partial c_l / \partial \theta$ vs. k

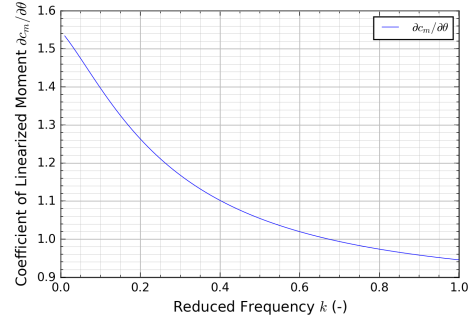


Figure 6.22: $\partial c_m / \partial \theta$ vs. k

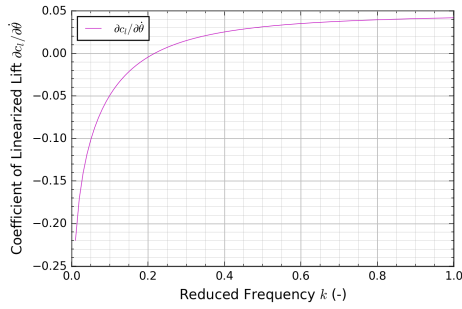


Figure 6.23: $\partial c_l / \partial \dot{\theta}$ vs. k

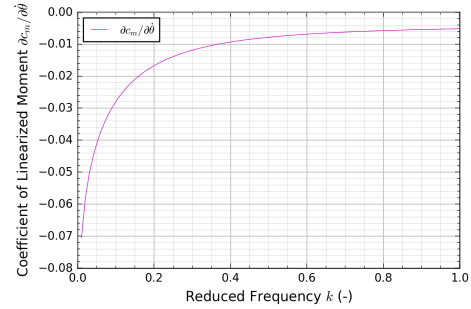


Figure 6.24: $\partial c_m / \partial \dot{\theta}$ vs. k

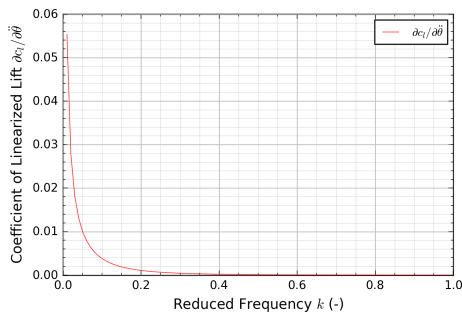


Figure 6.25: $\partial c_l / \partial \ddot{\theta}$ vs. k

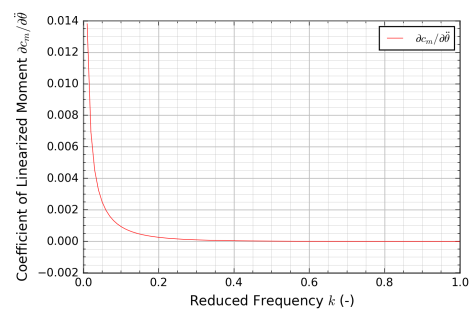


Figure 6.26: $\partial c_m / \partial \ddot{\theta}$ vs. k

6.4 Concluding Remarks and Discussion

The aim of this chapter was to validate the ability for the linearized lift and moment equations to predict harmonic oscillatory motion. Predicting harmonic oscillatory motion accurately is essential for an accurate prediction of the flutter boundary. This was done for an airfoil free to pitch about its midchord and a steady state angle of attack $\alpha_{ss}=1^\circ$, with an inflow velocity of 50 m/s ($Re = 10^6$). The linearized lift and moment coefficients were computed by perturbing the airfoil with a cubic perturbation function about the steady state. The lift/moment from the unsteady CFD results were used to compute the linearized coefficients. This was carried out in the foam-extend 3.2 framework. As a reminder for the reader, the assumption is that these coefficients are independent of the linearization parameters and that the linearized model with a set of constant coefficients is valid for any type of motion, as long as the perturbations are small such that flow linearity is ensured. In order to verify the results obtained by the linearized aerodynamic CFD model for harmonic oscillatory motion, the lift/moment normalized amplitude and phase angles as a function of reduced frequency k were computed with the linearized lift/moment coefficients and compared with Theodorsen Theory and the nonlinear unsteady CFD results presented in Chapter 5.

Preliminary analysis showed that the linearized coefficients were in fact not independent of the linearization parameters. Therefore, various linearization parameters were chosen with which the linearized coefficients were computed, in order to see whether the coefficients are truly independent of the linearization parameters. For Case 1, the final perturbation angle is $\theta'_{final} = 0.005^\circ$. The airfoil is perturbed for 20 time steps. For each final angular velocity $\dot{\theta}'_{final}$ of the range [100, 50, 25, 12.5, 6.25, 3.125, 1.5625], the corresponding perturbation rate $\bar{\theta}$ and time step Δt is calculated. These values are documented in Table 6.1. Tables 6.2 & 6.3 document the linearized lift and moment coefficients for different linearization parameters (i.e. cases), respectively. For Case 2, the difference lays in the final perturbation angle which is taken to be an order of magnitude larger than for Case 1, i.e. $\theta'_{final} = 0.05^\circ$. In addition, only a final angular velocity $\dot{\theta}'_{final}$ of the range [100, 50, 25, 12.5] was considered. The linearization parameters are documented in Table 6.4. Tables 6.5 & 6.6 document the linearized lift and moment coefficients for different linearization parameters (i.e. cases), respectively.

It was shown that for both cases, the linearized lift/moment coefficients are largely dependent on the linearization parameters, specifically the perturbation rate. Only the coefficient $\partial c_l / \partial \dot{\theta}$ and $\partial c_m / \partial \ddot{\theta}$ remained relatively constant for both cases. The fact that the linearized coefficients vary drastically implies that the lift/moment of perturbed cubic motion with different perturbation rates cannot be accurately predicted with a single set of linearized lift/moment coefficients. Furthermore, it was expected that the steady state lift/moment coefficients $\partial c_l / \partial \theta$ and $\partial c_m / \partial \theta$ would be close to the value obtained by Thin Airfoil Theory: $c_{l,\alpha}$ (i.e. 2π or 6.283) and $0.25c_{l,\alpha}$ (i.e. 0.5π or 1.571), respectively. This would imply that once the perturbations are stopped, the lift and moment at the current angle of attack are those of a steady state case. However, both the coefficients for almost all subcases of Case 1 & 2 were not close to the Thin Airfoil Theory values. Case 1.4 and 2.1 gave values of $\partial c_l / \partial \theta$ within 10% of Thin Airfoil Theory but the $\partial c_m / \partial \theta$ for both cases was negative.

It was shown that no set of linearized lift/moment coefficients could accurately predict the lift/moment normalized amplitudes and phase angles as a function of reduced frequency k . Essentially, this means that they cannot predict harmonic oscillatory motion. Case 1.1 - 1.3 provided results so inaccurate, that they were not included in this Chapter, but rather in Appendix E. It was seen that as the perturbation rate decreased, the results became better, but were still unsatisfactory; however, this does not imply that the lowest perturbation rate provides the best result. The better results seemed to approximate higher reduced frequencies better than the lower ones, which was unexpected. Furthermore, no single subcase gave the best result for both the lift and moment normalized amplitudes and phase angles.

Taking the aforementioned information into account, it seems that a set of *constant* linearized lift and moment coefficients cannot predict harmonically oscillating airfoil motion. In order to confirm this, an additional study was carried out. The airfoil was perturbed with a sinusoidal motion at different frequencies ω (i.e. k). The lift and moment for these perturbations were obtained from Theodorsen Theory and for each ω (i.e. k) the linearized lift/moment coefficients were computed. It was shown that the coefficients were not constant for any value of k which supports the conclusion that a set of linearized lift and moment coefficients cannot be constant and at the same time accurately predict the unsteady loads of a harmonically oscillating airfoil.

From the results presented in this chapter, some preliminary conclusions can be made on the topic of whether a linearized aerodynamic CFD model can be used to conduct a gust response analysis. The response of the airfoil to a gust will depend on the gust profile. Therefore, the linearized aerodynamic CFD model should be able to predict arbitrary airfoil motion accurately in order to adequately predict a gust response. Unfortunately, it was seen that cubic motions with different perturbation rates yielded different sets of lift/moment linearized coefficients. This indicates that unsteady lift/moment of different types of cubic motions cannot be predicted with the same set of linearized coefficients. Furthermore, it was shown that harmonic oscillatory motion of different reduced frequencies cannot be predicted with the same set of linearized lift/moment coefficients. These facts indicate that the linearized aerodynamic CFD model will not be able to predict arbitrary motion accurately. However, in order to be able to say this with certainty, additional research should be done in this area.

The remaining parts of the conclusion are dedicated to explaining, from a theoretical standpoint, why the proposed linearized aerodynamic CFD model should not be able to accurately predict unsteady air loads for a perturbed airfoil, regardless of whether the perturbation is harmonic or arbitrary. For this discussion, Theodorsen's expressions for the lift and moment of a harmonically pitching airfoil about the steady state are reintroduced

$$c_l = c_{l,ss} + \frac{\pi b}{U^2} \left[U\dot{\theta} - ba\ddot{\theta} \right] + \frac{c_{l,\alpha} C(k)}{U} \left[U\theta + b \left(\frac{1}{2} - a \right) \dot{\theta} \right], \quad (6.19)$$

$$\begin{aligned}
c_m = c_{m,ss} + \frac{\pi}{2U^2} \left[-Ub \left(\frac{1}{2} - a \right) \dot{\theta} - b^2 \left(\frac{1}{8} + a^2 \right) \ddot{\theta} \right] + \\
+ \frac{c_{l,\alpha} C(k)}{2U} \left(a + \frac{1}{2} \right) \left[U\theta + b \left(\frac{1}{2} - a \right) \dot{\theta} \right].
\end{aligned} \tag{6.20}$$

The elastic axis about which the lift and moment are computed is defined as a semi chords from the airfoil midchord, where a is positive aft of the midchord. The terms in the first square bracket of the lift/moment expressions are the non-circulatory terms that develop immediately, while the terms in the second bracket are the circulatory terms. Its reduction in amplitude and change of phase is due to the effect of the shed vortices, accounted for by Theodorsen's function $C(k)$, where k is the reduced frequency. The reduced frequency k is related to the oscillation frequency ω_{rad} by the following expression: $k = \omega_{rad}b/U$. So for a given airfoil subject to an inflow velocity of U , k is defined by ω_{rad} . For different oscillation frequencies, a different k and hence $C(k)$ can be computed emphasizing how Theodorsen's function accounts for the wake effect that are dependent on the frequency of the motion. If the effects of the shed wake are to be neglected, $C(k)$ is equal to 1 and the circulatory forces also develop immediately. As such the quasi-steady model is obtained.

The implication that aerodynamic forces develop immediately means that they depend only on the current motion θ , $\dot{\theta}$ and $\ddot{\theta}$ of the airfoil and not the history of the motion (i.e. the shed wake) since the beginning of airfoil motion. For example, consider an airfoil free to only pitch. At time t_0 it is at rest. The airfoil then starts to move in pitch and has a pitching displacement, velocity and acceleration. The motion can be harmonic or arbitrary. After a certain amount of time at time t_1 , the airfoil pitch displacement, velocity and acceleration is θ_1 , $\dot{\theta}_1$ and $\ddot{\theta}_1$. Regardless of how the airfoil reached the specific values of the pitch displacement, velocity and acceleration, the lift and moment computed will always be the same. For harmonic motion, the history of the motion is taken care of by Theodorsen's function. Note that here, the wake is assumed to be fully developed and periodic since the beginning of the airfoil motion. However, for arbitrary changes in the angle of attack, a closed form solution like that of Theodorsen does not exist. The lift and moment forces can be found numerically with a superposition of small step changes in angle of attack, where a single step change in angle of attack is defined by the Wagner function (Wagner, 1925), which takes into account the wake effects. Now reconsider the proposed linearized aerodynamic CFD model for the lift and moment about the steady state, as is shown below

$$c_l \approx c_{l,ss} + \frac{\partial c_l}{\partial \theta} \Big|_s \theta + \frac{\partial c_l}{\partial \dot{\theta}} \Big|_s \dot{\theta} + \frac{\partial c_l}{\partial \ddot{\theta}} \Big|_s \ddot{\theta}, \tag{6.21}$$

$$c_m \approx c_{m,ss} + \frac{\partial c_m}{\partial \theta} \Big|_s \theta + \frac{\partial c_m}{\partial \dot{\theta}} \Big|_s \dot{\theta} + \frac{\partial c_m}{\partial \ddot{\theta}} \Big|_s \ddot{\theta}. \tag{6.22}$$

Note that the coefficients are found from unsteady CFD simulations and are considered constant. Again, the underlying assumption is that this model can compute the unsteady air loads for any type of motion as long as the perturbations are small, such that flow linearity is ensured. Clearly, due to the fact that the coefficients are constant, these expressions resemble a quasi-steady model, where the lift and moment depend only on the current pitch displacement θ , velocity $\dot{\theta}$ and acceleration $\ddot{\theta}$ and hence develop immediately. This implies that the effect of the shed wake is neglected. As such, it is understandable that this linearized model cannot accurately compute the unsteady lift and moment coefficients of a harmonically oscillating airfoil. Due to the fact that the wake history is neglected, it is also expected that arbitrary motion cannot be accurately computed.

Chapter 7

Conclusion

The main objective of this Master Thesis was to validate the *efficacy of a linearized aerodynamic CFD model* for accurately predicting flutter. The analysis was carried out on a 2D airfoil free to pitch, subject to incompressible flow and a Reynolds number of 1 million. The linearized model is constructed by perturbing the airfoil with a cubic perturbation function $\theta' = \bar{\theta}t^3$ from the steady state for a number of time steps and using the results of the unsteady CFD simulation to solve for the linearized lift and moment coefficients. Note that $\bar{\theta}$ represents the perturbation rate. A larger value implies higher velocity and accelerations of the perturbed airfoil. The coefficients are assumed to be constant and independent of the perturbation rate. The constructed linearized lift and moment models are assumed to be valid for any type of perturbations, as long as the perturbations are small such that flow linearity is preserved. A more in depth explanation of the model was given in Section 2.4 & 6.2. It was shown that the coefficients are largely dependent on the perturbation rate $\bar{\theta}$ of the cubic perturbation function, as is documented in Tables 6.2, 6.3, 6.5 & 6.6.

For accurately predicting flutter, the linearized model must be able to accurately predict unsteady aerodynamic loads due to a harmonically oscillating airfoil. This is due to the fact that flutter is a neutral stability point and at the flutter boundary the airfoil oscillates harmonically. Note that below the flutter boundary, the oscillations are damped, while above the flutter boundary the oscillations are amplified. Therefore, the unsteady lift and moment computed by the linearized model was compared with that of Theodorsen and OpenFOAM simulations for an harmonically oscillating airfoil. Specifically, the lift/moment normalized amplitudes and phase angles were compared as a function of reduced frequency. This comparison was carried out for various sets of linearized lift/moment coefficients (i.e. subcases of Case 1 & 2). No set of linearized coefficients could accurately predict the unsteady air loads of a harmonically oscillating airfoil. This implies that carrying out flutter computations with such a method would result in an inaccurate flutter boundary prediction. An additional analysis was carried out in order to see whether it is actually possible for a set of constant linearized lift/moment coefficients to predict harmonic motion of different reduced frequencies. The airfoil was perturbed with a sinusoidal perturbation function that was dependant

on the reduced frequency. The lift and moment due to the perturbation were calculated from Theodorsen Theory. The coefficients were extracted for each reduced frequency and it was shown that the linearized lift/moment coefficients were largely dependent on the reduced frequency, implying that a set of constant coefficients cannot accurately predict the unsteady air loads of harmonically oscillating airfoils of different frequencies. Taking the aforementioned points into account the research question of this author's Master Thesis, given below, can be answered.

Can linearized aerodynamic CFD models, used to model the aerodynamics of an aeroelastic system, be utilized to accurately predict flutter?

The answer is, no they cannot, because in order to accurately predict flutter, the aerodynamic model must accurately predict the unsteady air loads of a harmonically oscillating airfoil. From the analysis carried out in this Master Thesis, it was shown that the linearized aerodynamic CFD model is incapable of that.

Some preliminary conclusions can be made on whether the linearized aerodynamic CFD model can be used for gust response analysis. The response of an airfoil to an arbitrary gust will also be arbitrary. In other words, different gusts will result in different responses. Therefore, the linearized aerodynamic CFD model should be able to predict arbitrary responses. The fact that the linearized lift/moment coefficients significantly depend on the perturbation rate of the cubic perturbation function implies that different types of cubic motion also cannot be predicted with the same set of linearized lift/moment coefficients. Taking this into account, as well as the fact that a set of constant linearized lift/moment coefficients cannot predict the unsteady air loads of a harmonically oscillating airfoil, means that it is unlikely that a linearized aerodynamic CFD model with constant coefficients can be used to predict air loads of arbitrary airfoil motions. However, more research should be done in this area to come to a stronger conclusion.

Finally, from the theoretical discussion of Section 6.4, it was explained that the proposed linearized aerodynamic CFD model should not be able to accurately predict the unsteady air loads due to oscillatory or arbitrary motion because it does not take into account the effects of the shed wake. As such it cannot be used to accurately carry out gust response analyses or flutter computations. From this conclusion arises the recommendation for future work which is to incorporate the wake effects into the linearized aerodynamic CFD model.

Bibliography

- Ira Herbert Abbott and Albert Edward Von Doenhoff. *Theory of wing sections, including a summary of airfoil data*. Courier Corporation, 1959.
- airfoiltools.com. Airfoil Tools. <http://airfoiltools.com/airfoil/details?airfoil=n0009sm-il>, 10 May 2018.
- Edward Albano and William P Rodden. A doublet-lattice method for calculating lift distributions on oscillating surfaces in subsonic flows. *AIAA journal*, 7(2):279–285, 1969.
- John David Anderson Jr. *Fundamentals of aerodynamics*. Tata McGraw-Hill Education, 2010.
- David Baker. *Flight and Flying: a chronology*. Facts on File, 1994.
- Armin Beckert and Holger Wendland. Multivariate interpolation for fluid-structure-interaction problems using radial basis functions. *Aerospace Science and Technology*, 5(2):125–134, 2001.
- Leonardo Bergami. Aeroelastic stability of a 2d airfoil section equipped with a trailing edge flap. 2008.
- Gunjit Bir and Jason Jonkman. Aeroelastic instabilities of large offshore and onshore wind turbines. In *Journal of Physics: Conference Series*, volume 75, page 012069. IOP Publishing, 2007.
- Raymond L Bisplinghoff, Holt Ashley, and Robert L Halfman. *Aeroelasticity*. Courier Corporation, 2013.
- Frederic J Blom. Considerations on the spring analogy. *International journal for numerical methods in fluids*, 32(6):647–668, 2000.
- J Boussinesque. theorie de lecoulement tourbillant, mem. *Presentes par Divers Savants Acad. Sci. Inst. Fr.*, 23:45–50, 1877.
- M Burt. The impact of computational unsteady aerodynamics in aerospace engineering past. In *Present and Future*, *European Forum: Recent Developments and Applications in Aeronautical CFD*, pages 1–3, 1993.
- cfD online.com. CFD Online. https://www.cfd-online.com/Wiki/Turbulence_intensity, 30 July 2018.

- A Roderick Collar and Alan Simpson. *Matrices and engineering dynamics*. Halsted Press, 1987.
- AR Collar. The expanding domain of aeroelasticity. *The Aeronautical Journal*, 50(428): 613–636, 1946.
- Ulrike Cordes, G Kampers, T Meißner, C Tropea, J Peinke, and M Hölling. Note on the limitations of the theodorsen and sears functions. *Journal of Fluid Mechanics*, 811, 2017.
- A De Boer, MS Van der Schoot, and Hester Bijl. Mesh deformation based on radial basis function interpolation. *Computers & structures*, 85(11-14):784–795, 2007a.
- A De Boer, MS Van der Schoot, and Hester Bijl. Mesh deformation based on radial basis function interpolation. *Computers & structures*, 85(11-14):784–795, 2007b.
- R. De Breuker. Lecture Notes, *Aeroelasticity*. TU Delft. <https://blackboard.tudelft.nl>, 1 March 2018.
- Christoph Degand and Charbel Farhat. A three-dimensional torsional spring analogy method for unstructured dynamic meshes. *Computers & structures*, 80(3-4):305–316, 2002.
- G. Dimitradis. Lecture Notes, *Aeroelasticity and Experimental Aerodynamics*. University of Liege. <http://www.ltas-aea.ulg.ac.be/cms/index.php?page=aeroelasticity-course>, 20 June 2018.
- Mark Drela. Xfoil: An analysis and design system for low reynolds number airfoils. In *Low Reynolds number aerodynamics*, pages 1–12. Springer, 1989.
- Charbel Farhat, Christoph Degand, Bruno Koobus, and Michel Lesoinne. Torsional springs for two-dimensional dynamic unstructured fluid meshes. *Computer methods in applied mechanics and engineering*, 163(1-4):231–245, 1998.
- Michael Fehrs, Anna C.L.M. van Rooij, and Jens Nitzsche. Flutter prediction in the transonic flight regime with the γ -re- θ transition model. In Eugenio Oñate, Xavier Oliver, and Antonio Huerta, editors, *6th. European Conference on Computational Fluid Dynamics (ECFD VI)*, pages 6334–6346. International Center for Numerical Methods in Engineering, July 2014. URL <https://elib.dlr.de/94555/>.
- Joel H Ferziger and Milovan Peric. *Computational methods for fluid dynamics*. Springer Science & Business Media, 2012.
- H Försting. Challenges and perspectives in computational aeroelasticity. In *International Forum on Aeroelasticity and Structural Dynamics*, pages 1–1, 1995.
- Robert Alexander Frazer. The flutter of aeroplane wings. *The Aeronautical Journal*, 33(222): 407–454, 1929.
- Robert Alexander Frazer, William Jolly Duncan, Arthur Roderich Collar, et al. *Elementary matrices and some applications to dynamics and differential equations*, volume 1963. Cambridge University Press Cambridge, 1938.
- Yuan Cheng Fung. *An introduction to the theory of aeroelasticity*. Courier Dover Publications, 2008.

- IE Garrick and Wilmer H Reed III. Historical development of aircraft flutter. *Journal of Aircraft*, 18(11):897–912, 1981.
- J Giesing and T Kalman. Subsonic unsteady aerodynamics for general configurations. In *10th Aerospace Sciences Meeting*, page 26, 1971.
- Joseph P Giesing, William P Rodden, and Bernhard Stahl. Sears function and lifting surface theory for harmonic gust fields. *Journal of Aircraft*, 7(3):252–255, 1970.
- Robert L Halfman. Experimental aerodynamic derivatives of a sinusoidally oscillating airfoil in two-dimensional flow. 1952.
- Martin Otto Laver Hansen, Jens Nørkær Sørensen, S Voutsinas, Niels Sørensen, and H Aa Madsen. State of the art in wind turbine aerodynamics and aeroelasticity. *Progress in aerospace sciences*, 42(4):285–330, 2006.
- Hermann J Hassig. An approximate true damping solution of the flutter equation by determinant iteration. *Journal of Aircraft*, 8(11):885–889, 1971.
- Brian T Helenbrook. Mesh deformation using the biharmonic operator. *International journal for numerical methods in engineering*, 56(7):1007–1021, 2003.
- Charles Hirsch. *Numerical computation of internal and external flows: The fundamentals of computational fluid dynamics*. Elsevier, 2007.
- <http://www.nasa.gov>. 2DN00: 2D NACA 0012 Airfoil Validation Case. https://turbmodels.larc.nasa.gov/naca0012_val.html, 11 April 2018.
- Daniel J Inman and Ramesh Chandra Singh. *Engineering vibration*, volume 3. Prentice Hall Englewood Cliffs, NJ, 1994.
- Hrvoje Jasak. Error analysis and estimation for the finite volume method with applications to fluid flows. 1996.
- Dennis A Johnson and LS King. A mathematically simple turbulence closure model for attached and separated turbulent boundary layers. *AIAA journal*, 23(11):1684–1692, 1985.
- Joseph Katz and Allen Plotkin. *Low-speed aerodynamics*, volume 13. Cambridge university press, 2001.
- Thiemo Kier. Comparison of unsteady aerodynamic modelling methodologies with respect to flight loads analysis. In *AIAA Atmospheric Flight Mechanics Conference and Exhibit*, page 6027, 2005.
- Hans G Küssner. *Untersuchung der Bewegung einer Platte beim Eintritt in eine Strahlgrenze*. Zentrale für techn.-wiss. Berichtswesen, 1935.
- Gordon J Leishman. *Principles of helicopter aerodynamics with CD extra*. Cambridge university press, 2006.
- David J Lucia, Philip S Beran, and Walter A Silva. Reduced-order modeling: new approaches for computational physics. *Progress in aerospace sciences*, 40(1-2):51–117, 2004.

- Daniel R Lynch and Kevin O'Neill. Elastic grid deformation for moving boundary problems in two space dimensions. *Finite elements in water resources*, 2, 1980.
- Florian R Menter. Zonal two equation kw turbulence models for aerodynamic flows. In *23rd fluid dynamics, plasmadynamics, and lasers conference*, page 2906, 1993.
- Florian R Menter. Two-equation eddy-viscosity turbulence models for engineering applications. *AIAA journal*, 32(8):1598–1605, 1994.
- Joseba Murua, Rafael Palacios, and J Michael R Graham. Applications of the unsteady vortex-lattice method in aircraft aeroelasticity and flight dynamics. *Progress in Aerospace Sciences*, 55:46–72, 2012.
- Bonifacius Bima Prananta. Physical and numerical aspects of aeroelastic simulations. 1999.
- Gerald Recktenwald. The ke turbulence model. *ME*, 448:548, 2009.
- Kenneth Roger. Airplane math modeling methods for active control design. *AGARD-CP-288*, 1977.
- Hermann Schlichting and Klaus Gersten. *Boundary-layer theory*. Springer, 2016.
- David M Schuster, Danny D Liu, and Lawrence J Huttzell. Computational aeroelasticity: success, progress, challenge. *Journal of Aircraft*, 40(5):843–856, 2003.
- Walter A Silva and Robert E Bartels. Development of reduced-order models for aeroelastic analysis and flutter prediction using the cfl3dv6. 0 code. *Journal of Fluids and Structures*, 19(6):729–745, 2004.
- Benjamin Smilg and Lee S Wasserman. Application of three-dimensional flutter theory to aircraft structures. *US Army Air Force Tech. Rept*, 4798, 1942.
- M. Stuurman. Simulating flutter for a 100-m wind turbine blade: using a CFD-CSD coupled method in OpenFOAM. Master's thesis, TU Delft, The Netherlands, 2016.
- Theodore Theodorsen. General theory of aerodynamic instability and the mechanism of flutter. *NACA Technical Report*, (496), 1935.
- A. van Zuijlen. Lecture notes, an introduction to numerical coupled simulation, May 2008.
- AG Von Baumhauer and C Koning. On the stability of oscillations of an airplane wing. 1923.
- Herbert Wagner. Über die entstehung des dynamischen auftriebes von tragflügeln. *ZAMM-Journal of Applied Mathematics and Mechanics/Zeitschrift für Angewandte Mathematik und Mechanik*, 5(1):17–35, 1925.
- Terry A. Weisshaar, 2017. Aeroelasticity, an introduction to fundamental problems - with a historical perspective, examples and homework problems, *AAE556 Aeroelasticity*. Purdue University, unpublished.
- Frank M White and Isla Corfield. *Viscous fluid flow*, volume 3. McGraw-Hill New York, 2006.
- A Wick. Grid deformation techniques for two-dimensional hybrid grids. In *In 10th International Meshing Roundtable, pages 261–267, Sandia National Laboratories*. Citeseer, 2001.

-
- Jan Robert Wright and Jonathan Edward Cooper. *Introduction to aircraft aeroelasticity and loads*, volume 20. John Wiley & Sons, 2008.
- Rudy Yurkovich, D Liu, and P Chen. State-of-the-art of unsteady aerodynamics for high performance aircraft. In *39th Aerospace Sciences Meeting and Exhibit*, page 428, 2001.
- Dehong Zeng and C Ross Ethier. A semi-torsional spring analogy model for updating unstructured meshes in 3d moving domains. *Finite Elements in Analysis and Design*, 41(11-12): 1118–1139, 2005.

Appendix A

Derivation of Modal Aerodynamic Matrices

In this appendix, the derivation of the modal matrices $[\tilde{M}_a]$, $[\tilde{C}_a]$ and $[\tilde{K}_a]$ is explained. The modal matrices appear on the RHS of Equation 2.27, where the RHS is reintroduced below

$$RHS = [\Phi]^T [M_a] [\Phi] \{\ddot{\mathbf{a}}\} + [\Phi]^T [C_a] [\Phi] \{\dot{\mathbf{a}}\} + [\Phi]^T [K_a] [\Phi] \{\mathbf{a}\}. \quad (\text{A.1})$$

Note that $[\tilde{M}_a] = [\Phi]^T [M_a] [\Phi]$, $[\tilde{C}_a] = [\Phi]^T [C_a] [\Phi]$ and $[\tilde{K}_a] = [\Phi]^T [K_a] [\Phi]$. The derivation of the modal matrices is done for $[\tilde{K}_a]$, but the same approach is used for deriving $[\tilde{M}_a]$ and $[\tilde{C}_a]$. As a reminder, $[K_a]$ is a $n \times n$ matrix and is given by Equation 2.21, where n is the degrees of freedom of the system. $[\Phi]$ is a matrix with a set of k orthonormal eigenvectors (with respect to the structural mass matrix) of a $n \times 1$ dimension. The final $[\tilde{K}_a]$ matrix is a $k \times k$ matrix, as is shown by the derivation below. For easier understanding, the derivation is carried out with an arbitrarily chosen finite value of n and k , rather than using the symbols n and k themselves. So, for this purpose, the number of degrees of freedom chosen is $n = 5$. The number of eigenmodes, and hence eigenvectors chosen, is $k = 3$. Therefore, the aerodynamic stiffness matrix $[K_a]$ is written as

$$[K_a] = \begin{bmatrix} \frac{\partial F_1}{\partial x_1} & \frac{\partial F_1}{\partial x_2} & \frac{\partial F_1}{\partial x_3} & \frac{\partial F_1}{\partial x_4} & \frac{\partial F_1}{\partial x_5} \\ \frac{\partial F_2}{\partial x_1} & \frac{\partial F_2}{\partial x_2} & \frac{\partial F_2}{\partial x_3} & \frac{\partial F_2}{\partial x_4} & \frac{\partial F_2}{\partial x_5} \\ \frac{\partial F_3}{\partial x_1} & \frac{\partial F_3}{\partial x_2} & \frac{\partial F_3}{\partial x_3} & \frac{\partial F_3}{\partial x_4} & \frac{\partial F_3}{\partial x_5} \\ \frac{\partial F_4}{\partial x_1} & \frac{\partial F_4}{\partial x_2} & \frac{\partial F_4}{\partial x_3} & \frac{\partial F_4}{\partial x_4} & \frac{\partial F_4}{\partial x_5} \\ \frac{\partial F_5}{\partial x_1} & \frac{\partial F_5}{\partial x_2} & \frac{\partial F_5}{\partial x_3} & \frac{\partial F_5}{\partial x_4} & \frac{\partial F_5}{\partial x_5} \end{bmatrix}, \quad (\text{A.2})$$

where $\frac{\partial F_1}{\partial x_1}$ represents the change in force on the first degree of freedom as a result of the change in displacement of the first degree of freedom, while $\frac{\partial F_1}{\partial x_2}$ represents the change in force

on the first degree of freedom as a result of the change in displacement of the second degree of freedom and so on. $\frac{\partial F_2}{\partial x_1}$ represents the change in force on the second degree of freedom as a result of the change in displacement of the first degree of freedom, while $\frac{\partial F_2}{\partial x_2}$ represents the change in force on the second degree of freedom as a result of the change in displacement of the second degree of freedom and so on. The physical interpretation of the terms in rows 3-5 can be analogously explained. Note that these partial derivatives are evaluated at the steady state $|_s$; however, this was omitted from the terms for convenience. Moving on, the displacement can be written as $\{\mathbf{x}\} = [\Phi]\{\mathbf{a}\}$ from Equation 2.24, where $[\Phi]$ is a matrix with a set of k orthonormal eigenvectors (with respect to the structural mass matrix) of a $n \times 1$ dimension. For $n = 5$ and $k = 3$, the displacement equation becomes the following

$$\begin{Bmatrix} x_1 \\ x_2 \\ x_3 \\ x_4 \\ x_5 \end{Bmatrix} = \begin{bmatrix} \Phi_{1,1} & \Phi_{1,2} & \Phi_{1,3} \\ \Phi_{2,1} & \Phi_{2,2} & \Phi_{2,3} \\ \Phi_{3,1} & \Phi_{3,2} & \Phi_{3,3} \\ \Phi_{4,1} & \Phi_{4,2} & \Phi_{4,3} \\ \Phi_{5,1} & \Phi_{5,2} & \Phi_{5,3} \end{bmatrix} \begin{Bmatrix} a_1 \\ a_2 \\ a_3 \end{Bmatrix}, \quad (\text{A.3})$$

where each column in Equation A.3 is an eigenvector. Derivating the LHS of Equation A.3 with respect to a_1 , a_2 and a_3 results in the following

$$\begin{Bmatrix} \frac{\partial x_1}{\partial a_1} \\ \frac{\partial x_2}{\partial a_1} \\ \frac{\partial x_3}{\partial a_1} \\ \frac{\partial x_4}{\partial a_1} \\ \frac{\partial x_5}{\partial a_1} \end{Bmatrix} = \begin{Bmatrix} \Phi_{1,1} \\ \Phi_{2,1} \\ \Phi_{3,1} \\ \Phi_{4,1} \\ \Phi_{5,1} \end{Bmatrix}; \quad \begin{Bmatrix} \frac{\partial x_1}{\partial a_2} \\ \frac{\partial x_2}{\partial a_2} \\ \frac{\partial x_3}{\partial a_2} \\ \frac{\partial x_4}{\partial a_2} \\ \frac{\partial x_5}{\partial a_2} \end{Bmatrix} = \begin{Bmatrix} \Phi_{1,2} \\ \Phi_{2,2} \\ \Phi_{3,2} \\ \Phi_{4,2} \\ \Phi_{5,2} \end{Bmatrix}; \quad \begin{Bmatrix} \frac{\partial x_1}{\partial a_3} \\ \frac{\partial x_2}{\partial a_3} \\ \frac{\partial x_3}{\partial a_3} \\ \frac{\partial x_4}{\partial a_3} \\ \frac{\partial x_5}{\partial a_3} \end{Bmatrix} = \begin{Bmatrix} \Phi_{1,3} \\ \Phi_{2,3} \\ \Phi_{3,3} \\ \Phi_{4,3} \\ \Phi_{5,3} \end{Bmatrix}. \quad (\text{A.4})$$

Taking into account the expression given in Equation A.4, the matrix of eigenvectors $[\Phi]$ can be alternatively expressed as

$$[\Phi] = \begin{bmatrix} \frac{\partial x_1}{\partial a_1} & \frac{\partial x_1}{\partial a_2} & \frac{\partial x_1}{\partial a_3} \\ \frac{\partial x_2}{\partial a_1} & \frac{\partial x_2}{\partial a_2} & \frac{\partial x_2}{\partial a_3} \\ \frac{\partial x_3}{\partial a_1} & \frac{\partial x_3}{\partial a_2} & \frac{\partial x_3}{\partial a_3} \\ \frac{\partial x_4}{\partial a_1} & \frac{\partial x_4}{\partial a_2} & \frac{\partial x_4}{\partial a_3} \\ \frac{\partial x_5}{\partial a_1} & \frac{\partial x_5}{\partial a_2} & \frac{\partial x_5}{\partial a_3} \end{bmatrix}. \quad (\text{A.5})$$

In order to obtain $[\tilde{K}_a]$, the matrix $[K_a]$ is first multiplied by $[\Phi]$

$$[K_a][\Phi] = \begin{bmatrix} \frac{\partial F_1}{\partial x_1} & \frac{\partial F_1}{\partial x_2} & \frac{\partial F_1}{\partial x_3} & \frac{\partial F_1}{\partial x_4} & \frac{\partial F_1}{\partial x_5} \\ \frac{\partial F_2}{\partial x_1} & \frac{\partial F_2}{\partial x_2} & \frac{\partial F_2}{\partial x_3} & \frac{\partial F_2}{\partial x_4} & \frac{\partial F_2}{\partial x_5} \\ \frac{\partial F_3}{\partial x_1} & \frac{\partial F_3}{\partial x_2} & \frac{\partial F_3}{\partial x_3} & \frac{\partial F_3}{\partial x_4} & \frac{\partial F_3}{\partial x_5} \\ \frac{\partial F_4}{\partial x_1} & \frac{\partial F_4}{\partial x_2} & \frac{\partial F_4}{\partial x_3} & \frac{\partial F_4}{\partial x_4} & \frac{\partial F_4}{\partial x_5} \\ \frac{\partial F_5}{\partial x_1} & \frac{\partial F_5}{\partial x_2} & \frac{\partial F_5}{\partial x_3} & \frac{\partial F_5}{\partial x_4} & \frac{\partial F_5}{\partial x_5} \end{bmatrix} \begin{bmatrix} \frac{\partial x_1}{\partial a_1} & \frac{\partial x_1}{\partial a_2} & \frac{\partial x_1}{\partial a_3} \\ \frac{\partial x_2}{\partial a_1} & \frac{\partial x_2}{\partial a_2} & \frac{\partial x_2}{\partial a_3} \\ \frac{\partial x_3}{\partial a_1} & \frac{\partial x_3}{\partial a_2} & \frac{\partial x_3}{\partial a_3} \\ \frac{\partial x_4}{\partial a_1} & \frac{\partial x_4}{\partial a_2} & \frac{\partial x_4}{\partial a_3} \\ \frac{\partial x_5}{\partial a_1} & \frac{\partial x_5}{\partial a_2} & \frac{\partial x_5}{\partial a_3} \end{bmatrix}. \quad (\text{A.6})$$

Note that when carrying out the matrix multiplication, the first row of matrix $[K_a]$ times the first column of matrix $[\Phi]$ is equal to $\partial F_1/\partial a_1$ as is shown below

$$\frac{\partial F_1}{\partial a_1} = \frac{\partial F_1}{\partial x_1} \frac{\partial x_1}{\partial a_1} + \frac{\partial F_1}{\partial x_2} \frac{\partial x_2}{\partial a_1} + \frac{\partial F_1}{\partial x_3} \frac{\partial x_3}{\partial a_1} + \frac{\partial F_1}{\partial x_4} \frac{\partial x_4}{\partial a_1} + \frac{\partial F_1}{\partial x_5} \frac{\partial x_5}{\partial a_1}. \quad (\text{A.7})$$

In order to equate the RHS with $\partial F_1/\partial a_1$ the chain rule is employed, because F is a function of \mathbf{x} , $\dot{\mathbf{x}}$ and $\ddot{\mathbf{x}}$ which in turn are a function of \mathbf{a} , $\dot{\mathbf{a}}$ and $\ddot{\mathbf{a}}$. For the variable \mathbf{x} , this is clearly visible from Equation A.3. Therefore, to derivate F with respect to \mathbf{a} , i.e. a_1 , the chain rule must be employed. The product of all the rows and columns of Equation A.6 can be expressed analogously as is shown in Equation A.8 below

$$[K_a][\Phi] = \begin{bmatrix} \frac{\partial F_1}{\partial a_1} & \frac{\partial F_1}{\partial a_2} & \frac{\partial F_1}{\partial a_3} \\ \frac{\partial F_2}{\partial a_1} & \frac{\partial F_2}{\partial a_2} & \frac{\partial F_2}{\partial a_3} \\ \frac{\partial F_3}{\partial a_1} & \frac{\partial F_3}{\partial a_2} & \frac{\partial F_3}{\partial a_3} \\ \frac{\partial F_4}{\partial a_1} & \frac{\partial F_4}{\partial a_2} & \frac{\partial F_4}{\partial a_3} \\ \frac{\partial F_5}{\partial a_1} & \frac{\partial F_5}{\partial a_2} & \frac{\partial F_5}{\partial a_3} \end{bmatrix} \quad \text{or} \quad [K_a][\Phi] = \begin{bmatrix} \frac{\partial \{\mathbf{F}\}}{\partial a_1} & \frac{\partial \{\mathbf{F}\}}{\partial a_2} & \frac{\partial \{\mathbf{F}\}}{\partial a_3} \end{bmatrix}. \quad (\text{A.8})$$

In the first expression of the Equation above, $\frac{\partial F_1}{\partial a_1}$ represents the change in force on the first degree of freedom as a result of the change in displacement of the first *mode*, while $\frac{\partial F_1}{\partial a_2}$ represents the change in force on the first degree of freedom as a result of the change in displacement of the second *mode* and so on. $\frac{\partial F_2}{\partial a_1}$ represents the change in force on the second degree of freedom as a result of the change in displacement of the first *mode*, while $\frac{\partial F_2}{\partial a_2}$ represents the change in force on the second degree of freedom as a result of the change in displacement of the second *mode* and so on. The physical interpretation of the terms in rows 3-5 can be analogously explained. Of course, these derivatives are evaluated at the steady state $|_s$. Note that the second expression in Equation A.8 above is a more convenient way of

writing the product $[K_a][\Phi]$ and will be used in the next step. Multiplying the left-hand side of $[K_a][\Phi]$ by $[\Phi]^T$ results in the following system

$$[\Phi]^T [K_a][\Phi] = \begin{bmatrix} \{\Phi_1\}^T \\ \{\Phi_2\}^T \\ \{\Phi_3\}^T \end{bmatrix} \begin{bmatrix} \frac{\partial\{\mathbf{F}\}}{\partial a_1} & \frac{\partial\{\mathbf{F}\}}{\partial a_2} & \frac{\partial\{\mathbf{F}\}}{\partial a_3} \end{bmatrix}. \quad (\text{A.9})$$

Taking into account that the eigenvectors $\{\Phi_1\}$, $\{\Phi_2\}$ and $\{\Phi_3\}$ are constant, multiplying matrices of Equation A.9 gives the following system

$$[\Phi]^T [K_a][\Phi] = \begin{bmatrix} \frac{\partial\{\Phi_1\}^T\{\mathbf{F}\}}{\partial a_1} & \frac{\partial\{\Phi_1\}^T\{\mathbf{F}\}}{\partial a_2} & \frac{\partial\{\Phi_1\}^T\{\mathbf{F}\}}{\partial a_3} \\ \frac{\partial\{\Phi_2\}^T\{\mathbf{F}\}}{\partial a_1} & \frac{\partial\{\Phi_2\}^T\{\mathbf{F}\}}{\partial a_2} & \frac{\partial\{\Phi_2\}^T\{\mathbf{F}\}}{\partial a_3} \\ \frac{\partial\{\Phi_3\}^T\{\mathbf{F}\}}{\partial a_1} & \frac{\partial\{\Phi_3\}^T\{\mathbf{F}\}}{\partial a_2} & \frac{\partial\{\Phi_3\}^T\{\mathbf{F}\}}{\partial a_3} \end{bmatrix}. \quad (\text{A.10})$$

In Equation A.10 above, the product $\{\Phi_1\}^T\{\mathbf{F}\}$ maps the vector of forces $\{\mathbf{F}\}$ of each degree of freedom onto mode 1 and will be denoted by F_1 . The product $\{\Phi_2\}^T\{\mathbf{F}\}$ maps the vector of forces $\{\mathbf{F}\}$ of each degree of freedom onto mode 2 (i.e. F_2) and so on. Therefore, for a $n = 5$ degree of freedom system, where only $k = 3$ eigenvectors are considered, the modal stiffness matrix $[\tilde{K}_a]$ becomes

$$[\tilde{K}_a] = [\Phi]^T [K_a][\Phi] = \begin{bmatrix} \frac{\partial F_1}{\partial a_1} & \frac{\partial F_1}{\partial a_2} & \frac{\partial F_1}{\partial a_3} \\ \frac{\partial F_2}{\partial a_1} & \frac{\partial F_2}{\partial a_2} & \frac{\partial F_2}{\partial a_3} \\ \frac{\partial F_3}{\partial a_1} & \frac{\partial F_3}{\partial a_2} & \frac{\partial F_3}{\partial a_3} \end{bmatrix}. \quad (\text{A.11})$$

Now, $\frac{\partial F_1}{\partial a_1}$ represents the change in force on the first *mode* as a result of the change in displacement of the first mode, while $\frac{\partial F_1}{\partial a_2}$ represents the change in force on the first *mode* as a result of the change in displacement of the second *mode* and so on. $\frac{\partial F_2}{\partial a_1}$ represents the change in force on the second *mode* as a result of the change in displacement of the first *mode*, while $\frac{\partial F_2}{\partial a_2}$ represents the change in force on the second *mode* as a result of the change in displacement of the second *mode* and so on. The physical interpretation of the terms in row 3 can be analogously explained. Clearly the size of the matrices reduce from a $n \times n$ $[K_a]$ matrix to a $k \times k$ $[\tilde{K}_a]$ matrix and as such a smaller number of coefficients, i.e. partial derivatives must be computed. Knowing, from Equation 2.24, that $\{\dot{\mathbf{x}}\} = [\Phi]\{\dot{\mathbf{a}}\}$ and $\{\ddot{\mathbf{x}}\} = [\Phi]\{\ddot{\mathbf{a}}\}$, the modal aerodynamic damping $[\tilde{C}_a]$ and mass $[\tilde{M}_a]$ matrices can be easily derived.

Appendix B

Unsteady Lift for $k = 0.1, 0.3, 0.4$ & 0.8

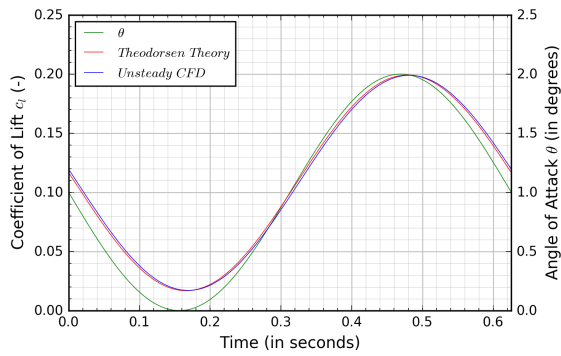


Figure B.1: c_l vs. *time*, $k = 0.1$

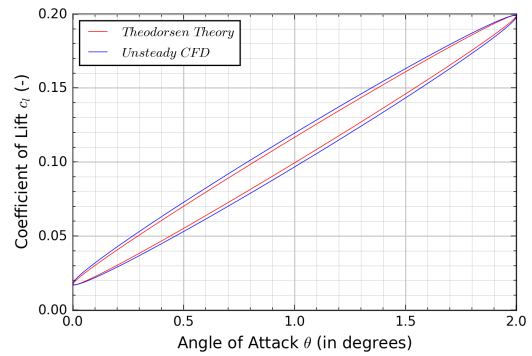


Figure B.2: c_l vs. θ , $k = 0.1$

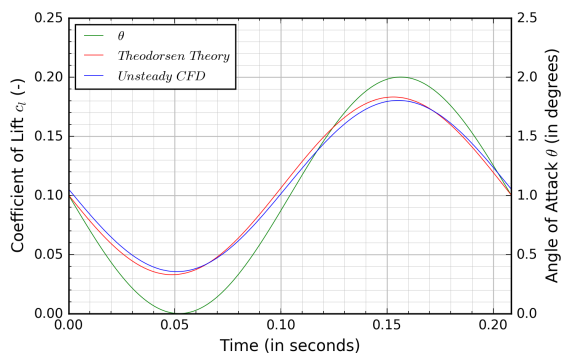


Figure B.3: c_l vs. *time*, $k = 0.3$

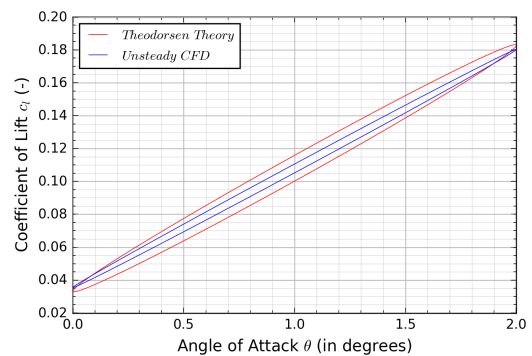


Figure B.4: c_l vs. θ , $k = 0.3$

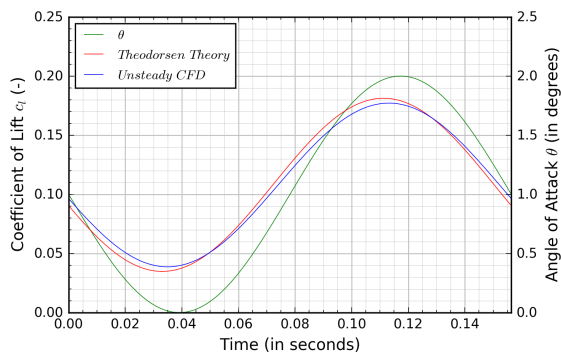


Figure B.5: c_l vs. *time*, $k = 0.4$

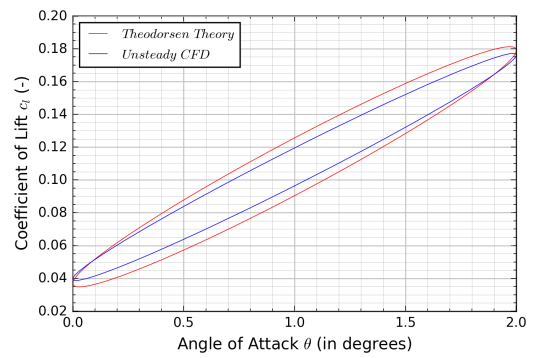


Figure B.6: c_l vs. θ , $k = 0.4$

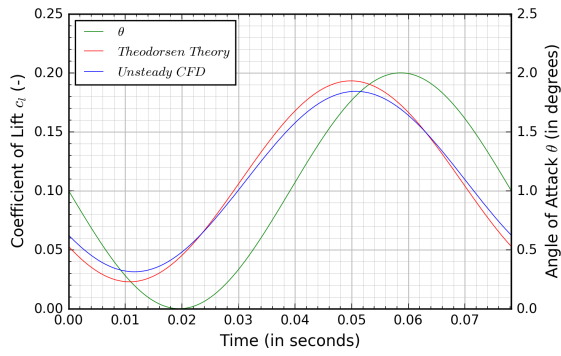


Figure B.7: c_l vs. *time*, $k = 0.8$

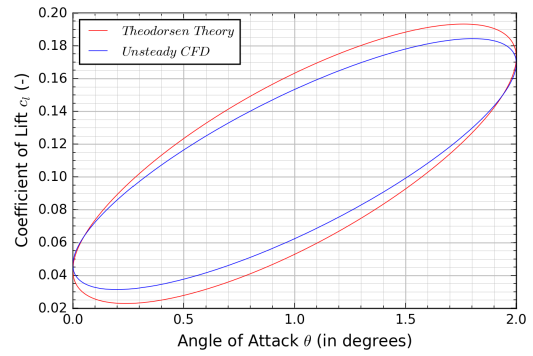


Figure B.8: c_l vs. θ , $k = 0.8$

Appendix C

Unsteady Moment for $k = 0.1, 0.3, 0.4$ & 0.8

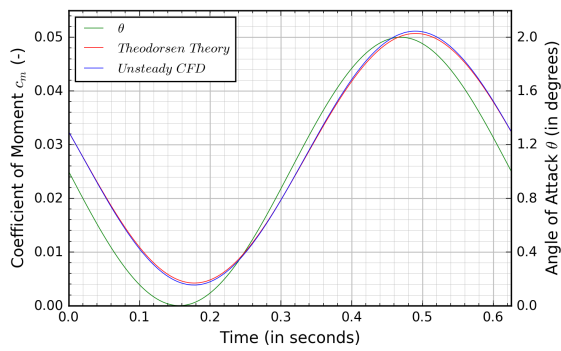


Figure C.1: c_m vs. time, $k = 0.1$

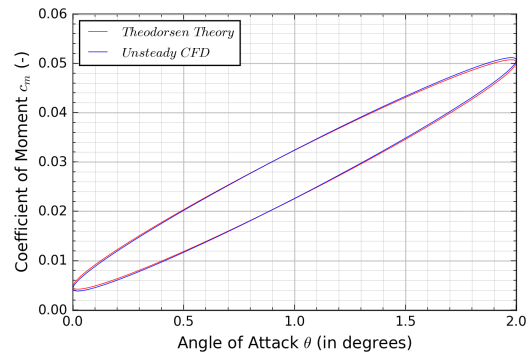


Figure C.2: c_m vs. θ , $k = 0.1$

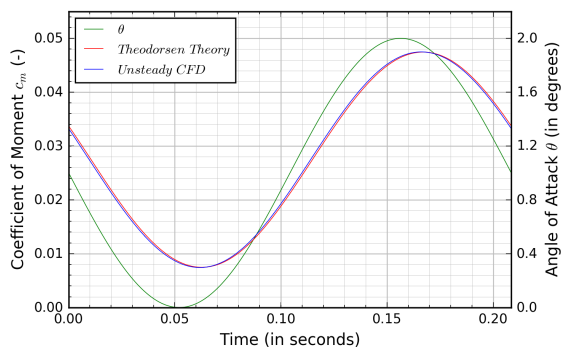


Figure C.3: c_m vs. time, $k = 0.3$

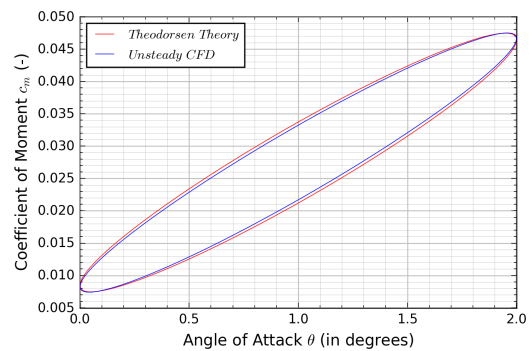


Figure C.4: c_m vs. θ , $k = 0.3$

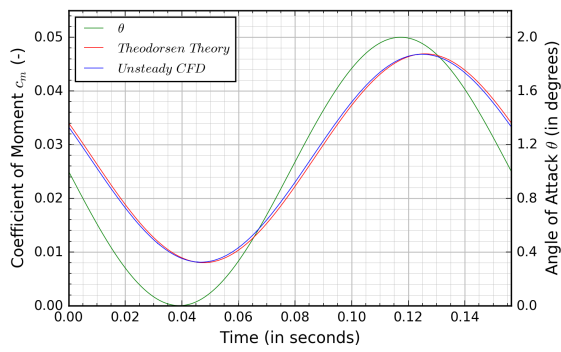


Figure C.5: c_m vs. time, $k = 0.4$

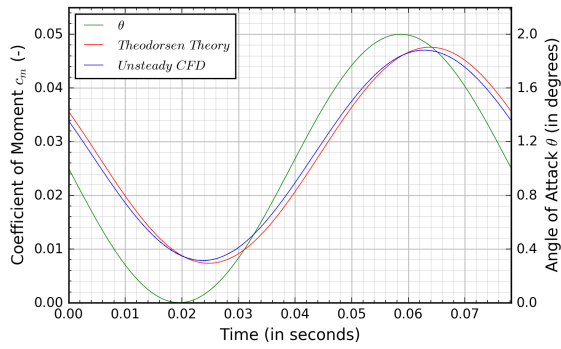


Figure C.7: c_m vs. time, $k = 0.8$

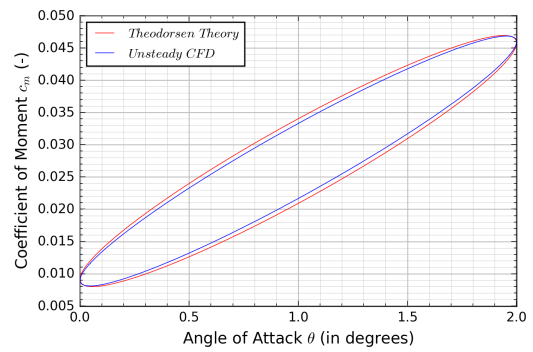


Figure C.6: c_m vs. θ , $k = 0.4$

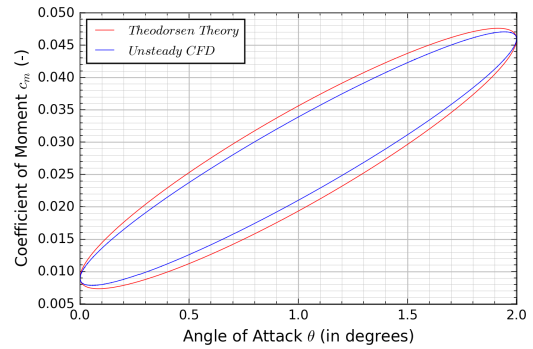


Figure C.8: c_m vs. θ , $k = 0.8$

Appendix D

A Comment on the A Matrix

Within this appendix, the reason for omitting the first 3 time steps in matrix $[A]$ of Section 6.2.1 is explained. Consider that the $[A]$ matrix is built of *all* 20 time steps as is shown below

$$[A] = \begin{bmatrix} \theta'_{1,ana} & \dot{\theta}'_{1,ana} & \ddot{\theta}'_{1,ana} \\ \theta'_{2,ana} & \dot{\theta}'_{2,ana} & \ddot{\theta}'_{2,ana} \\ \vdots & \vdots & \vdots \\ \theta'_{20,ana} & \dot{\theta}'_{20,ana} & \ddot{\theta}'_{20,ana} \end{bmatrix}, \quad (D.1)$$

where the subscript *ana* denotes that the displacement, velocity and acceleration terms are calculated from the analytical functions $\theta'_{ana} = \bar{\theta}t^3$, $\dot{\theta}'_{ana} = 3\bar{\theta}t^2$, $\ddot{\theta}'_{ana} = 6\bar{\theta}t$ at each discrete time t respectively, as was introduced by the expressions of Equation 6.3. In OpenFOAM, only the perturbation displacement $\theta'_{ana} = \theta t^3$ is imposed from the analytical function at each discrete time step t . So in order to compute the the velocity and acceleration at each discrete time, finite difference schemes are used. Assume the following finite difference expressions for the velocity $\dot{\theta}'_{n+1,num}$ and acceleration $\ddot{\theta}'_{n+1,num}$ at the new time level t_{n+1} are

$$\dot{\theta}'_{n+1,num} = \frac{\frac{3}{2}\theta'_{n+1,ana} - 2\theta'_{n,ana} + \frac{1}{2}\theta'_{n-1,ana}}{\Delta t}, \quad (D.2)$$

$$\ddot{\theta}'_{n+1,num} = \frac{\theta'_{n+1,ana} - 2\theta'_{n,ana} + \theta'_{n-1,ana}}{\Delta t^2}, \quad (D.3)$$

where $n = 0, 1, \dots, 19$ and represents the time steps taken. Note that $n = 0$ marks the first time step, $n = 1$ marks the second time step and so on. Furthermore, for the first time step (i.e.

$n=0$), $\theta'_{n-1,ana}$ from Equations D.2 & D.3 are unknown. Therefore, to compute the velocity and acceleration for the first time step t_1 , the following finite difference expressions are used

$$\dot{\theta}'_{n+1,num} = \frac{\theta'_{n+1,ana} - \theta'_{n,ana}}{\Delta t}, \quad (D.4)$$

$$\ddot{\theta}'_{n+1,num} = \frac{\theta'_{n+1,ana} - 2\theta'_{n,ana}}{\Delta t^2}. \quad (D.5)$$

Again, for the remaining time steps, the expressions given by Equations D.2 & D.3 are used. Keeping this in mind, another version of the $[A]$ matrix in which the displacement, velocity and acceleration as is computed by OpenFOAM is included, can be constructed as follows

$$[A] = \begin{bmatrix} \theta'_{1,ana} & \dot{\theta}'_{1,num} & \ddot{\theta}'_{1,num} \\ \theta'_{2,ana} & \dot{\theta}'_{2,num} & \ddot{\theta}'_{2,num} \\ \vdots & \vdots & \vdots \\ \theta'_{20,ana} & \dot{\theta}'_{20,num} & \ddot{\theta}'_{20,num} \end{bmatrix}. \quad (D.6)$$

Note that the first column consists of the imposed displacement in OpenFOAM that is identical to the analytical function $\theta'_{ana} = \bar{\theta}t^3$ at each discrete time t . The velocity and acceleration are computed numerically with Equations D.2-D.5. As is shown in the remainder of this appendix, the velocity and accelerations obtained by analytical functions for the first few time steps are not equal to those obtained by OpenFOAM. To make the $[A]$ matrix computed by analytical function similar to that computed by OpenFOAM, the first few steps are omitted when computing for the linearized coefficients. Figure D.1 & D.2 shows the ratio of the analytically computed velocity and numerically computed velocity (i.e. $\dot{\theta}'_{ana}/\dot{\theta}'_{num}$) and ratio of the analytically computed acceleration and numerically computed acceleration (i.e. $\ddot{\theta}'_{ana}/\ddot{\theta}'_{num}$) for 20 time steps, respectively.

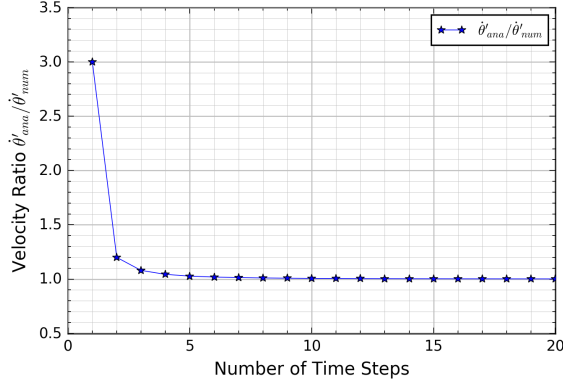


Figure D.1: $\dot{\theta}'_{ana}/\dot{\theta}'_{num}$ vs. time step

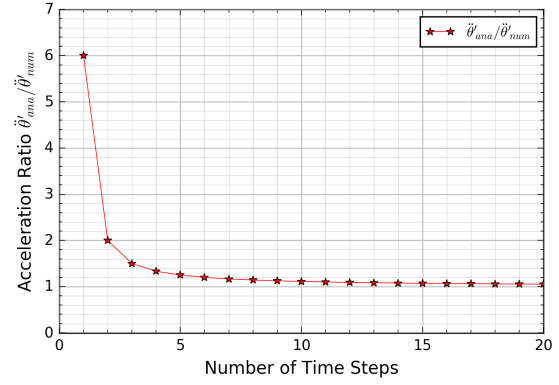


Figure D.2: $\ddot{\theta}'_{ana}/\ddot{\theta}'_{num}$ vs. time step

Note that on the x -axis, the time step number is plotted rather than the time value, because the ratios are independent of the magnitude of the time and only depends on the number of time steps taken. So for example, after one time step, the ratio of the velocity is 3, regardless of the size of the time step Δt and hence time t . Note that the ratio of the displacements are not shown because it is equal to 1. After 3 time steps, the ratios becomes close to 1, meaning that the numerically computed velocity and acceleration are similar to that computed by the analytical functions. Therefore, only the remaining time steps are used to build the $[A]$ matrix with analytical functions as is given by Equation 6.3 of Section 6.2.1. The derivations for the expressions of the velocity/acceleration ratios plotted in the figures above are given below. It is also shown that these expressions depend solely on the number of time steps, rather than the time value.

Keeping in mind that $\theta'_{n+1,ana}$, $\theta'_{n,ana}$ and $\theta'_{n-1,ana}$ can be expressed as $\bar{\theta}[(n+1)\Delta t]^3$, $\bar{\theta}[n\Delta t]^3$ and $\bar{\theta}[(n-1)\Delta t]^3$ respectively, Equations D.2-D.5 are rewritten in the form as follows

$$\dot{\theta}'_{n+1,num} = \frac{\frac{3}{2}\bar{\theta}[(n+1)\Delta t]^3 - 2\bar{\theta}[n\Delta t]^3 + \frac{1}{2}\bar{\theta}[(n-1)\Delta t]^3}{\Delta t}, \quad (\text{D.7})$$

$$\ddot{\theta}'_{n+1,num} = \frac{\bar{\theta}[(n+1)\Delta t]^3 - 2\bar{\theta}[n\Delta t]^3 + \bar{\theta}[(n-1)\Delta t]^3}{\Delta t^2}, \quad (\text{D.8})$$

$$\dot{\theta}'_{n+1,num} = \frac{\bar{\theta}[(n+1)\Delta t]^3 - \bar{\theta}[n\Delta t]^3}{\Delta t}, \quad (\text{D.9})$$

$$\ddot{\theta}'_{n+1,num} = \frac{\bar{\theta}[(n+1)\Delta t]^3 - 2\bar{\theta}[n\Delta t]^3}{\Delta t^2}. \quad (\text{D.10})$$

The velocity ratio is obtained by computing the fraction $\dot{\theta}'_{n+1,ana}/\dot{\theta}'_{n+1,num}$, where $\dot{\theta}'_{n+1,num}$ stems for Equation D.7. Similarly to what was shown in the previous paragraph $\dot{\theta}'_{n+1,ana}$ is equal to $3\bar{\theta}[(n+1)\Delta t]^2$. The velocity ratio is shown below

$$\frac{\dot{\theta}'_{n+1,ana}}{\dot{\theta}'_{n+1,num}} = \frac{3(n+1)^2}{\frac{3}{2}(n+1)^3 - 2n^3 + \frac{1}{2}(n-1)^3}. \quad (\text{D.11})$$

This expression is used to computed the velocity ratio for all time steps, expect for the first one, where $n=0$. For this special case, since t_{n-1} is not known, the velocity ratio is obtained by computing the fraction $\dot{\theta}'_{n+1,ana}/\dot{\theta}'_{n+1,num}$, where $\dot{\theta}'_{n+1,num}$ now stems for Equation D.9. The velocity ratio is shown below

$$\frac{\dot{\theta}'_{n+1,ana}}{\dot{\theta}'_{n+1,num}} = \frac{3(n+1)^2}{(n+1)^3 - n^3}. \quad (\text{D.12})$$

The acceleration ratio is obtained by computing the fraction $\ddot{\theta}'_{n+1,ana}/\ddot{\theta}'_{n+1,num}$, where $\ddot{\theta}'_{n+1,num}$ stems for Equation D.8. Similarly, $\ddot{\theta}'_{n+1,ana}$ is equal to $6\bar{\theta}[(n+1)\Delta t]$. The acceleration ratio is shown below

$$\frac{\ddot{\theta}'_{n+1,ana}}{\ddot{\theta}'_{n+1,num}} = \frac{6(n+1)}{(n+1)^3 - 2n^3 + (n-1)^3}. \quad (\text{D.13})$$

This expression is used to computed the acceleration ratio for all time steps, expect for the first one, where $n=0$. For this special case, since t_{n-1} is not known, the acceleration ratio is obtained by computing the fraction $\ddot{\theta}'_{n+1,ana}/\ddot{\theta}'_{n+1,num}$, where $\ddot{\theta}'_{n+1,num}$ now stems for Equation D.10. The acceleration ratio is shown below

$$\frac{\ddot{\theta}'_{n+1,ana}}{\ddot{\theta}'_{n+1,num}} = \frac{6(n+1)}{(n+1)^3 - 2n^3}. \quad (\text{D.14})$$

From the expressions for the velocity and accelerations ratios given by Equations D.11-D.14, it is clear that the ratios depend only on the number of time steps taken n .

Appendix E

Remaining Results of Case 1 & 2

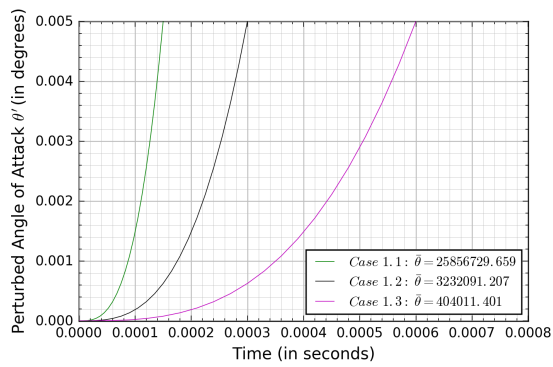


Figure E.1: Remaining Results of Case 1:
 θ' vs. time

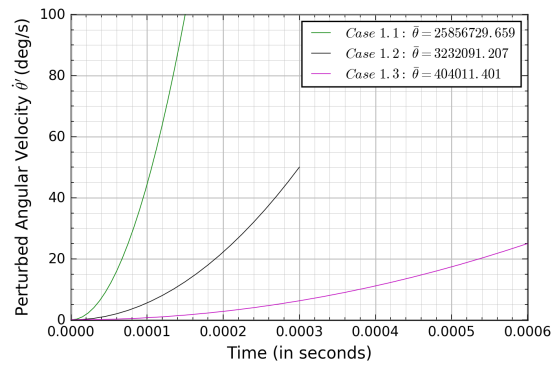


Figure E.2: Remaining Results of Case 1:
 $\dot{\theta}'$ vs. time

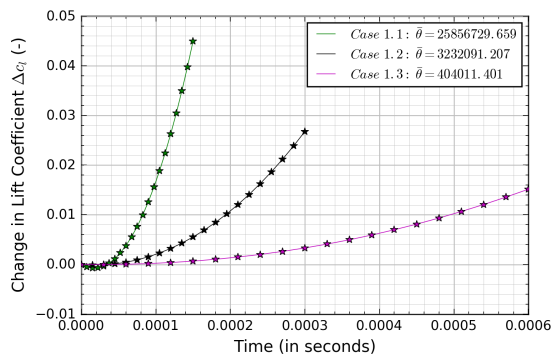


Figure E.3: Remaining Results of Case 1:
 Δc_l vs. time

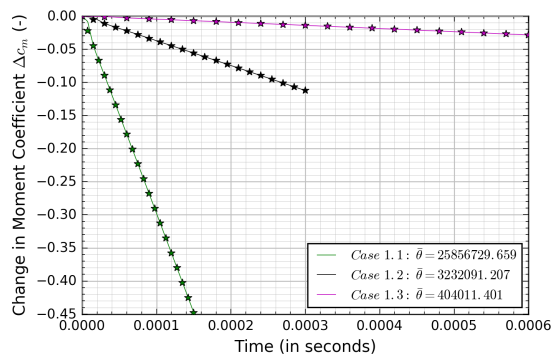


Figure E.4: Remaining Results of Case 1:
 Δc_m vs. time

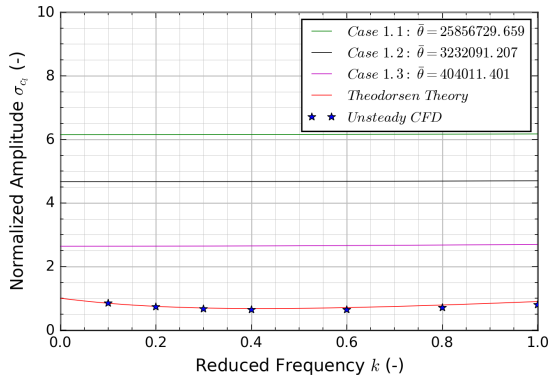


Figure E.5: Remaining Results of Case 1: σ_{c_l} vs. k (for linearized lift)

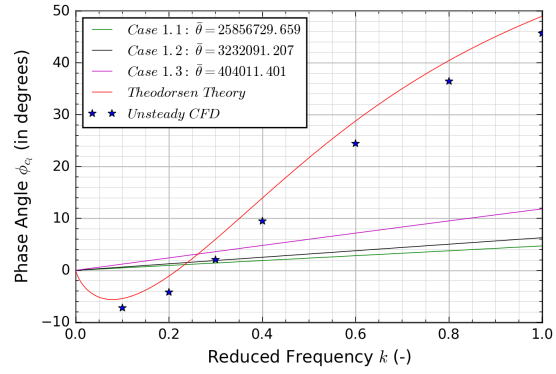


Figure E.6: Remaining Results of Case 1: ϕ_{c_l} vs. k (for linearized lift)

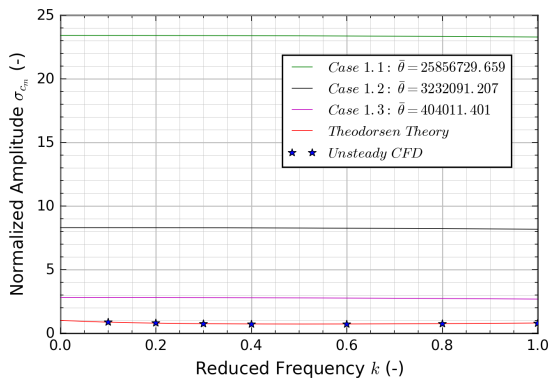


Figure E.7: Remaining Results of Case 1: σ_{c_m} vs. k (for linearized moment)

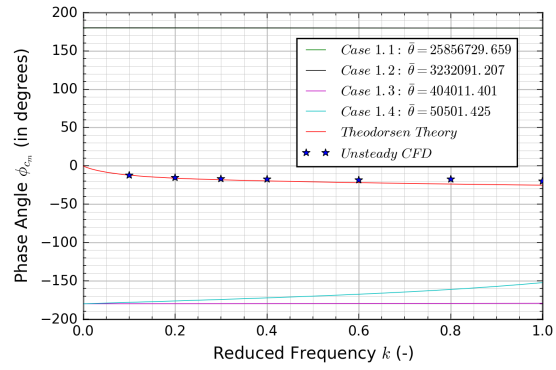


Figure E.8: Remaining Results of Case 1: ϕ_{c_m} vs. k (for linearized moment)

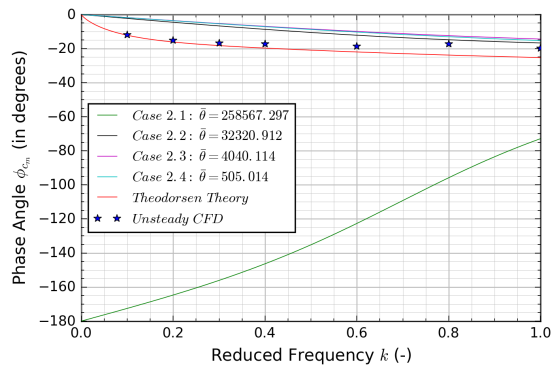


Figure E.9: Remaining Results of Case 2: ϕ_{c_m} vs. k (for linearized moment)

